

# Handbook of SiC properties for fuel performance modeling

Lance L. Snead <sup>a,\*</sup>, Takashi Nozawa <sup>a</sup>, Yutai Katoh <sup>a</sup>, Thak-Sang Byun <sup>a</sup>,  
Sosuke Kondo <sup>a</sup>, David A. Petti <sup>b</sup>

<sup>a</sup> Materials Science and Technology Division, Oak Ridge National Laboratory, P.O. Box 2008, Oak Ridge, TN 37831-6138, USA

<sup>b</sup> Idaho National Laboratory, P.O. Box 1625, Idaho Falls, ID 83415-3860, USA

---

## Abstract

The SiC layer integrity in the TRISO-coated gas-reactor fuel particle is critical to the performance, allowed burn-up, and hence intrinsic efficiency of high temperature gas cooled reactors. While there has been significant developmental work on manufacturing the fuel particles, detailed understanding of the effects of the complex in-service stress state combined with realistic materials property data under irradiation on fuel particle survival is not adequately understood. This particularly frustrates the modeling efforts that seek to improve fuel performance through basic understanding. In this work a compilation of non-irradiated and irradiated properties of SiC are provided and reviewed and analyzed in terms of application to TRISO fuels. In addition to a compilation and review of literature data, new data generated to fill holes in the existing database is included, specifically in the high-temperature irradiation regime. Another critical piece of information, the strength of the SiC/Pyrolytic carbon interface, was measured and is included, along with a formalism for its analysis. Finally, recommended empirical treatments of the data are suggested.

© 2007 Elsevier B.V. All rights reserved.

---

## 1. Introduction

The TRISO coating system has become the most common technique for fabricating fuels for the currently operating gas cooled reactors as well as the next generation high-temperature gas cooled reactors such as the pebble bed reactor being undertaken by PBMR Pty. Ltd. South Africa and the various very high temperature reactors being studied under the international Generation IV reactor program. Fig. 1 shows a schematic representation, and a SEM cross-section image of a heavily irradi-

ated TRISO fuel particle. The innermost element of this particle is the fuel kernel, which is coated with a low-density pyrolytic carbon (PyC) buffer layer containing about 50% void. This layer absorbs fission product recoils from the kernel, provides a reservoir for fission product gases, and accommodates kernel swelling without transmitting forces to the outer coatings. The next layer is a high-density, isotropic PyC layer that protects the kernel from reactions with chlorine during deposition of the SiC layer, provides structural support for the SiC layer, and protects the SiC from fission products and carbon monoxide during operation. Over this is a high-density, high strength SiC layer which provides the TRISO coating the ability to contain the high pressure generated in the kernel/buffer

---

\* Corresponding author. Tel.: +1 865 574 9942; fax: +1 865 241 3650.

E-mail address: [sneadll@ornl.gov](mailto:sneadll@ornl.gov) (L.L. Snead).

## Nomenclature

$a$	lattice parameter	$N_0$	Avogadro's number
$a_0$	lattice parameter at the reference temperature $T_0$	$p$	creep parameter
$A_p$	creep parameter	$p_{\text{Si}}$	dissociation vapor pressure of silicon carbide
$A_s$	creep parameter	$Q$	activation energy
$B$	irradiation creep compliance	$S$	void swelling
$C_{ij}$	elastic constants (tensors), $i, j = 1, 2, 3, 4$ , or 6	$t$	(1) time or (2) specimen thickness
$C_p$	specific heat	$T$	temperature
$d$	density	$T_0$	reference temperature (=298 K)
$D$	coefficient of swelling-creep coupling	$T_c$	characteristic temperature
$E$	Young's modulus	$T_{\text{irr}}$	neutron irradiation temperature
$E_0$	Young's modulus of pore free material at the reference temperature $T_0$	$T_m$	homologous temperature
$G$	shear modulus	$V_p$	porosity
$H^\circ$	enthalpy	$\alpha_d$	thermal diffusivity
$H_V$	Vickers hardness	$\alpha$	thermal expansion coefficient
$k_b$	Boltzmann constant	$\bar{\alpha}$	average thermal expansion coefficient
$k_d$	decomposition rate	$\gamma$	electronic specific heat coefficient
$K$	thermal conductivity	$\varepsilon_c$	creep strain
$K_e$	electron thermal conductivity	$\dot{\varepsilon}_c$	creep strain rate
$K_{\text{irr}}$	irradiated thermal conductivity	$\dot{\varepsilon}_{\text{ic}}$	irradiation creep strain rate
$K_{\text{non-irr}}$	non-irradiated thermal conductivity	$\theta_D$	Debye temperature
$K_p$	phonon thermal conductivity	$\mu$	coefficient of friction
$1/K_d$	thermal resistance by defect scattering	$\nu$	Poisson's ratio
$1/K_{\text{gb}}$	thermal resistance by grain boundary scattering	$\sigma$	stress
$1/K_{\text{rd}}$	thermal defect resistance	$\sigma_0$	(1) Weibull characteristic strength or (2) initially applied stress
$1/K_u$	thermal resistance by phonon–phonon (Umklapp) scattering	$\sigma_d$	debond initiation stress
$L_0$	Lorenz number	$\sigma_{\text{max}}$	complete debonding stress
$m$	(1) Weibull modulus or (2) bend stress relaxation ratio	$\tau$	creep parameter
$n$	creep exponent	$\tau_{\text{fr}}$	interfacial friction stress
		$\bar{\tau}_{\text{fr}}$	average interfacial friction stress at the interface
		$\tau_s$	interfacial debond shear strength
		$\phi$	fast neutron fluence

region by fission, and also provides structural support to withstand stresses developed due to irradiation-induced dimensional changes in the pyrolytic carbon layers. This SiC layer can therefore be thought of as a fission gas ‘pressure vessel’. The outermost layer in the TRISO system is another high-density, isotropic PyC layer that protects the SiC during the remainder of the fabrication process and provides structural stability to the particle during irradiation.

A number of TRISO performance models are currently under development. One common element

to these models is that they use the data provided in the ‘CEGA’ data report, published in July 1993 and other review publications [1–4]. The purpose of ‘CEGA’ Report on Material Models of Pyrocarbon and Pyrolytic Silicon Carbide was to update TRISO constitutive materials behavior and associated failure models for use in Modular Helium Reactor (MHR) fuel particle stress analysis. Unfortunately, the program that supported this compilation was prematurely ended. The result is that the CEGA report, while fairly comprehensive, does not provide adequate guidance for a number of key materials

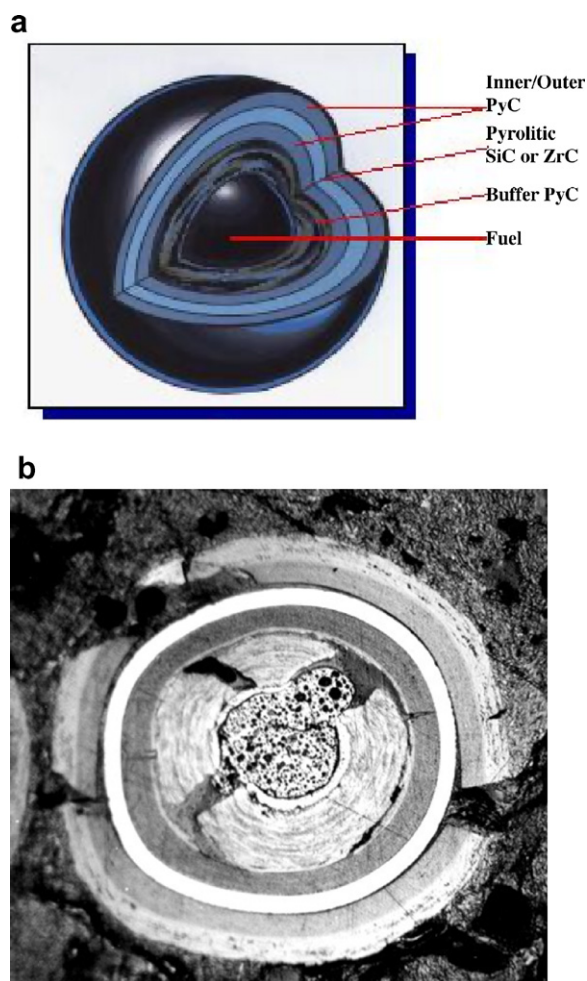


Fig. 1. (a) Schematic illustration of TRISO fuel and (b) irradiated TRISO showing cracked PyC.

properties needed for fuels modeling. This paper will begin to address some of the shortcomings of the CEGB report.

## 2. Non-irradiated SiC

### 2.1. Fabrication of silicon carbide

There are many routes for the fabrication of silicon carbide, and as both the non-irradiated and irradiated mechanical properties of SiC are a strong function of the fabrication route, a clear definition of the materials types is necessary and for this reason are briefly covered here. Silicon carbide was first synthesized in 1891 by Acheson [5]. The Acheson process is a carbothermic reduction produced by electrochemical reaction of high purity silica sand

and carbon in an electric furnace. The general reaction is



This original report suggested that  $\alpha$ -SiC formed above 2373 K and  $\beta$ -SiC at 1273–1873 K. The SiC product currently produced by the Acheson process is commercially known as Carborundum (CAR-BON-coRUNDUM).

Various fabrication techniques such as sintering, direct conversion, gas phase reaction and polymer pyrolysis are currently used for the synthesis of SiC. The sintering process is further classified into several categories based on the sintering agents used, consolidation mechanisms, and methods of pressurization. The direct conversion process is represented by reaction-bonding. A chemical vapor deposition (CVD) technique is one of the most familiar gas phase reaction methods for the synthesis of highly crystalline, stoichiometric, high-purity  $\beta$ -SiC [6,7]. The polymer pyrolysis is often utilized in production of continuous SiC fibers [8,9] and porous SiC.

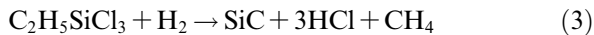
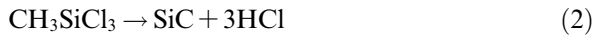
Prochazka [10] first developed the pressureless sintering process using a mixture of sub-micron  $\beta$ -SiC particles and minor amounts of sintering aids: boron and carbon. A relative density of >95% was achieved by sintering at 2293–2373 K without the application of external pressure. The pressureless sintering process has a relatively large flexibility and allows complexity in component shapes. However, the boron additive, which segregates at grain boundaries, does not behave well under neutron irradiation due to the large  $(n, \alpha)$  cross-section of the  $^{10}\text{B}$  isotope.

The hot-pressing technique can produce a robust and dense SiC form. In one variation, liquid phase sintering enables a lower temperature synthesis of SiC taking advantage of a low eutectic temperature of SiC particles and oxide additives such as  $\text{Al}_2\text{O}_3$  and  $\text{Y}_2\text{O}_3$ . These processes, however, limit the production to simple shape components due to the strict requirement of uniform pressure during sintering. Additionally, the excess additives, which tend to locate at grain boundaries, often cause degradation of mechanical properties.

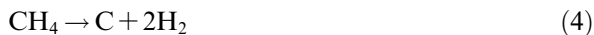
The reaction bonding process is a reaction of a mixture of SiC and carbon particles with metallic silicon in the form of vapor or liquid. The reaction-bonded SiC has a comparatively low density due to the presence of residual silicon. A major drawback of the reaction bonded SiC material is

severe degradation of the bulk performance stemming from this residual silicon.

The CVD process can produce a solid SiC form from a gas phase reactant at comparatively low temperature (1173–1373 K) without the use of sintering aids. Either methyltrichlorosilane ( $\text{CH}_3\text{SiCl}_3$ ), or an ethyltrichlorosilane ( $\text{C}_2\text{H}_5\text{SiCl}_3$ ) gas, combined with a hydrogen carrier gas, are common reactant gases. The CVD SiC material is typically synthesized by



The product methane resulting from the ethyltrichlorosilane reaction in Eq. (3) easily decomposes to free carbon with a generation of hydrogen as



The free carbon can lead to undesirable carbon layers or carbon-rich phases when using ethyltrichlorosilane as a reactant gas. A fluidized bed process, one of the CVD techniques, has been developed for fuel particles to form a pure and homogeneous SiC coating [11,12]. The representa-

tive microstructure of the fluidized bed SiC material was well summarized in Ref. [4]. Early generations of fluidized bed materials often contain micropores at grain boundaries [7]. As discussed later, such intergranular micropores potentially have a significant influence on physical-, thermal-, and mechanical-properties at elevated temperatures and under neutron irradiation. Presently, by optimizing the process conditions, high-quality SiC material can be synthesized even at low-temperatures  $\sim 1473$  K. Of the fabrication routes discussed, only CVD SiC material (including fluidized bed SiC) is inherently highly crystalline, pure and stoichiometric, providing a theoretical density of  $3.21 \text{ g/cm}^3$ . As will be seen later this is critical to irradiation stability.

## 2.2. Phase diagram

Fig. 2 shows an assessed equilibrium phase diagram of the Si–C system [13]. This phase diagram, however, does not distinguish between  $\alpha$ - and  $\beta$ -SiC. The detail of structural transformations of the SiC polytypes is described in the following section. The chemical bonding in SiC is not only

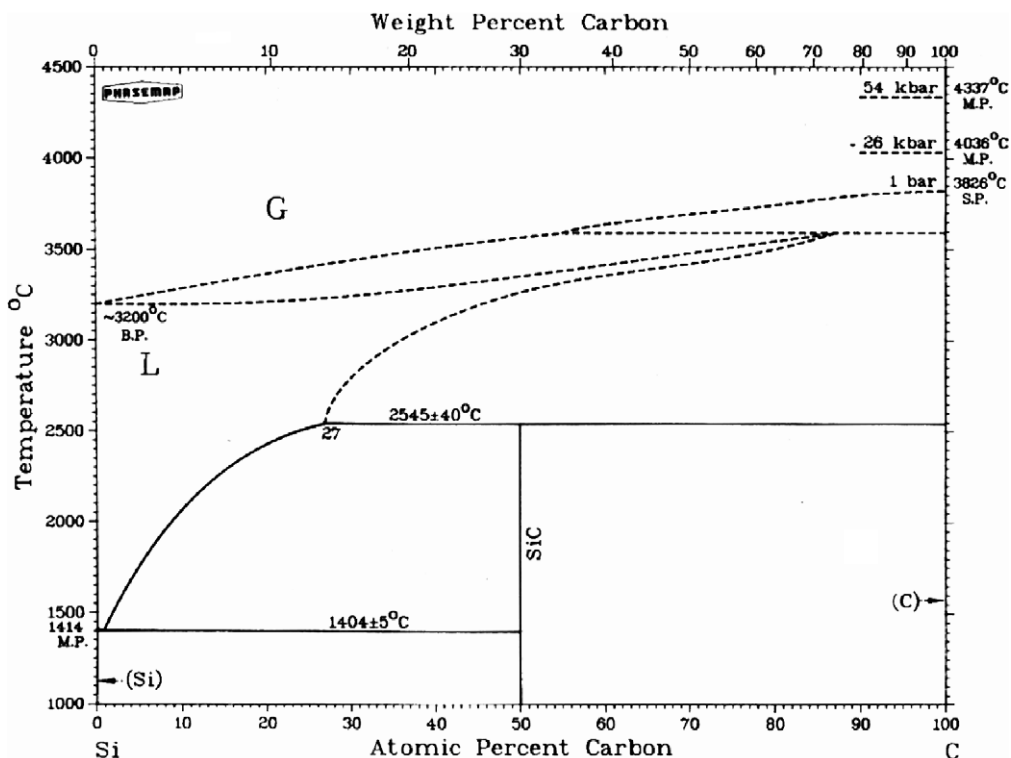


Fig. 2. Equilibrium phase diagram of the Si–C system [13].

covalent but also slightly ionic due to the differential electronegativity between silicon and carbon. The only stable compound is therefore obtained at the stoichiometric composition.

Several studies have reported conflicting decomposition temperatures and species for SiC, as reviewed by Olesinki and Abbaschian [13]. Presently, the most reliable thermal decomposition temperature of SiC is taken to be 2818 K [13]. Species generated with substantial vapor pressures are Si, SiC<sub>2</sub> and Si<sub>2</sub>C gases [14,15]. The amount of other species in vapors such as SiC, Si<sub>2</sub> and Si<sub>3</sub> are negligible. Price summarized the dissociation rate of  $\beta$ -SiC in his review paper [4]. The dissociation vapor pressure of  $\beta$ -SiC he reported was

$$p_{\text{Si}} = 7.59 \times 10^{12} \exp\left(-\frac{60926}{T}\right), \quad (5)$$

where  $p_{\text{Si}}$  is the dissociation pressure of silicon in units of Pa and  $T$  is the temperature in K. In contrast, he also reports a decomposition rate of  $\beta$ -SiC in a static argon atmosphere over the temperature range of  $2173 \leq T \leq 2373$  K as

$$k_d = 2.95 \times 10^{13} \exp\left(-\frac{56252}{T}\right), \quad (6)$$

where  $k_d$  is the decomposition rate in  $\mu\text{g}/\text{m}^2 \text{ s}$  and  $T$  is the temperature in K. In the actual TRISO coating system, the evaporation of silicon will be suppressed due to the presence of the outer protective PyC layer on the SiC, essentially serving as an environmental barrier overcoat.

### 2.3. Crystal structure

Silicon carbide has myriad polytypes dependent on the varied stacking of Si–C close-packed atomic planes [16–18]. The fundamental structural unit in all SiC polytypes is a covalently bonded primary co-ordination tetrahedron (either SiC<sub>4</sub> or CSi<sub>4</sub>). A carbon atom is at the centroid of four silicon atoms (or vice versa). One of the four Si–C bonds is parallel to, and taken to coincide with, the  $c$ -axis of the crystal. More than 200 polytypes are currently reported resulting from the wide variety of preferred stacking sequences [19]. The most common polytypes are 3C, 4H, 6H and 15R, where the leading number shows the repetition of the Si–C pair with C, H and R representing cubic, hexagonal and rhombohedral crystals, respectively (Table 1). The crystal structures of 3C-, 4H-, 6H- and 15R-SiC are schematically illustrated in Fig. 3. The 3C-SiC

Table 1  
Crystal structure of the SiC polytypes [18]

Poly-type	Space group	Element: Wyckoff ID, Position $xyz$	
2H	P63mc	Si:2b, 1/3 2/3 0	C:2b, 1/3 2/3 3/8
3C	F43m	Si:4a, 0 0 0	C:4c, 1/4 1/4 1/4
4H	P63mc	Si (1):2a, 0 0 0	C (1):2a, 0 0 3/16
		Si (2):2b, 1/3 2/3 1/4	C (2):2b, 1/3 2/3 7/16
6H	P63mc	Si (1):2a, 0 0 0	C (1):2a, 0 0 1/8
		Si (2):2b, 0 0 1/2	C (2):2b, 1/3 2/3 7/24
		Si (3):2b, 1/3 2/3 5/6	C (3):2b, 1/3 2/3 23/24
15R	R3m	Si (1):3a, 0 0 0	C (1):3a, 0 0 3/60
		Si (2):3a, 00 2/15	C (2):3a, 0 0 11/16
		Si (3):3a, 00 6/15	C (3):3a, 0 0 27/60
		Si (4):3a, 00 9/15	C (4):3a, 0 0 39/16
		Si (5):3a, 0 0 13/15	C (5):3a, 0 0 55/60

crystal, known as  $\beta$ -SiC, has the only sequence out of the infinite number of variations that shows cubic symmetry (Fig. 4). All the other polytypes, which show non-cubic symmetry, are classified as  $\alpha$ -SiC.

Fig. 5 shows a stability diagram for SiC polytypes. The stability of SiC polytypes is primarily dependent on temperature. The cubic form of SiC (3C-SiC) is believed to be more stable than the hexagonal structure (6H-SiC) below 2373 K [21], although some studies dispute this finding [22,23]. In contrast, 2H-SiC, which has the simplest stacking sequence, is rarely observed at higher temperatures. Krishna et al. [24] reported that single crystals of 2H-SiC can be easily transformed to 3C-SiC on annealing in argon at temperatures above 1673 K. In addition to temperature dependence, the effect of minute impurities and deviation from strict C:Si stoichiometry have been shown to play a role in polytype stability.

### 2.4. Lattice parameter and density

Table 2 lists lattice parameters and density for various structural types of SiC at room-temperature [25], commonly derived by X-ray diffraction. The lattice parameter and density of  $\beta$ -SiC at room-temperature are 0.4358 nm and 3.21 g/cm<sup>3</sup>, respectively.

The lattice parameter increases slightly with increasing temperature for all SiC polytypes [26–28]. Li and Bradt [28] reported the temperature dependence of the lattice parameter at high-temperatures for high-purity and polycrystalline  $\beta$ -SiC, utilizing X-ray diffraction. The lattice parameter of  $\beta$ -SiC,  $a$  (in nm), can be expressed by the third order polynomial



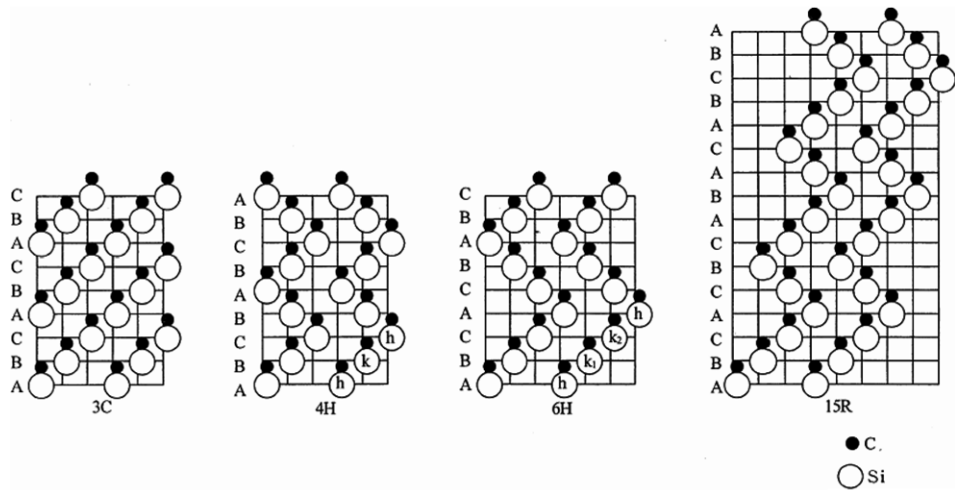


Fig. 3. Examples of the crystal structure of SiC polytypes: 3C, 4H, 6H and 15R [20].

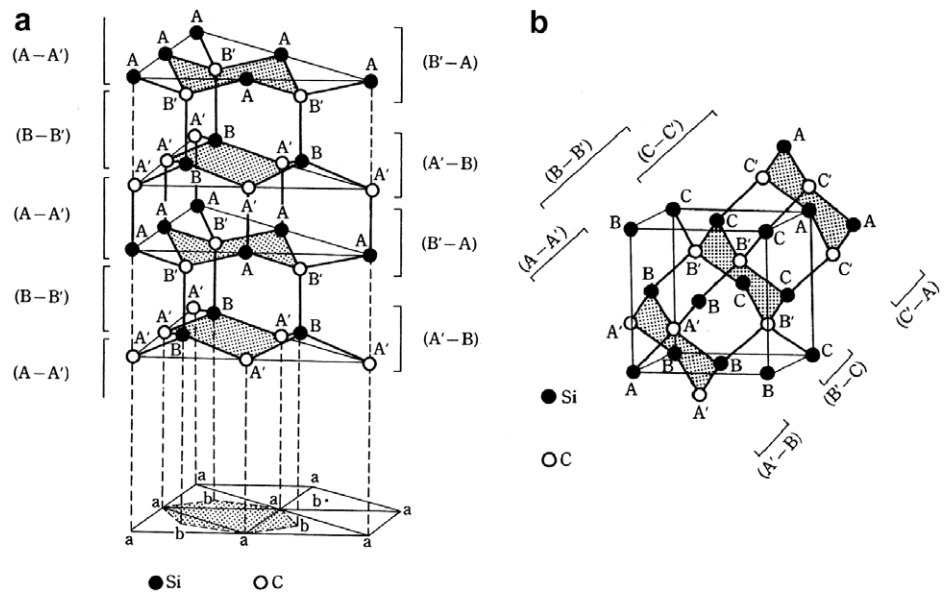


Fig. 4. Crystal structures of (a)  $\alpha$ -SiC and (b)  $\beta$ -SiC.

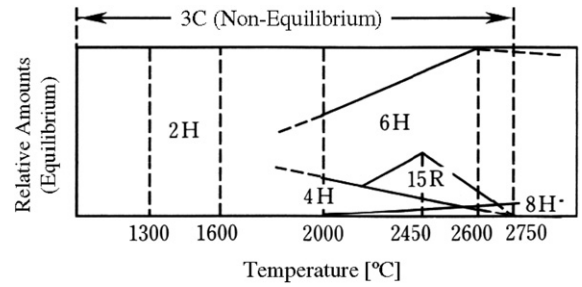


Fig. 5. Phase stability diagram of SiC polytypes [16].

Table 2  
Lattice parameters and density of SiC polytypes at room-temperature [25]

Polytype	Density (g/cm <sup>3</sup> )	Lattice parameter (nm)
2H	3.219	$a = 0.3081, c = 0.5031$
3C	3.215	$a = 0.43589$
4H	3.215	$a = 0.3081, c = 1.0061$
6H	3.215	$a = 0.3081, c = 1.5092$
15R	–	$a = 0.3073, c = 3.770$
21R	–	$a = 0.3073, c = 5.278$

$$a = 0.43577 + 1.3887 \times 10^{-6}(T - 273) \\ + 7.8494 \times 10^{-10}(T - 273)^2 \\ - 2.4434 \times 10^{-13}(T - 273)^3, \quad (7)$$

where the temperature,  $T$ , is in K. The standard deviation for the above equation is  $\pm 2.6 \times 10^{-5}$  nm. The change in lattice parameter at elevated temperatures consequently gives thermal expansion. However, as discussed in the following section, the very small change in lattice parameter of SiC ( $\sim 0.5\%$  at 1273 K) yields a very low thermal expansion coefficient.

## 2.5. Thermal properties

### 2.5.1. Heat content

It is well established that the specific heat of SiC is higher than that of the other refractory carbides and nitrides. The specific heat of SiC has been reported over a wide temperature range [29–39] and is summarized in Fig. 6. The specific heat of SiC was generally measured by calorimetry. The temperature-dependence of the specific heat can be treated in two temperature regions: a rapid increase at low temperatures (below 200 K) and a gradual

increase at higher temperatures. Of particular emphasis is that no systematic difference can be distinguished between the structural types.

At temperatures below the Debye temperature,  $\theta_D$ , the specific heat,  $C_p$ , of the material can be expressed using the electronic specific heat coefficient,  $\gamma$ , and the Debye temperature

$$C_p \cong \gamma T + CT^3, \quad (8)$$

where

$$C = \frac{234N_0k_b}{\theta_D^3}. \quad (9)$$

The constant  $C$  is determined by plotting  $C_p/T$  vs.  $T^2$ , where  $N_0$  is Avogadro's number ( $=6.02 \times 10^{23}$ ) and  $k_b$  is Boltzmann's constant ( $=1.38 \times 10^{-23}$  J/K). The Debye temperature of SiC is reported to be in the range 860–1200 K [40–45]. In general, the contribution from the electrical heat conductance is negligibly small since the covalent-bond SiC is essentially an electrical insulator. This correlation appears to be satisfactory in the temperature range 0–200 K.

In contrast, the specific heat of SiC increases only slowly with increasing temperature at elevated temperatures. The specific heat,  $C_p$  (in J/kg K), over the

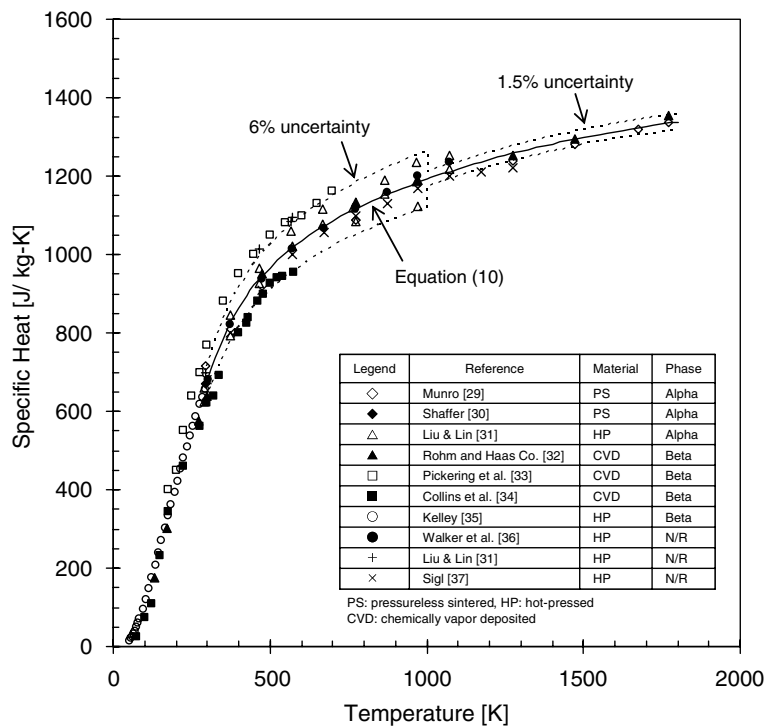


Fig. 6. Specific heat of SiC at elevated temperatures.

temperature range 200–2400 K can be approximately expressed as

$$C_p = 925.65 + 0.3772T - 7.9259 \times 10^{-5}T^2 - \frac{3.1946 \times 10^7}{T^2}, \quad (10)$$

where the temperature,  $T$ , is in K. The uncertainties in the recommended specific heat of SiC are  $\pm 7\%$  ( $200 \leq T \leq 1000$  K) and  $\pm 4\%$  ( $1000 \leq T \leq 2400$  K). The specific heat of SiC at room-temperature is therefore taken as  $671 \pm 47$  J/kg K.

### 2.5.2. Thermal conductivity

The thermal conductivity of the covalent carbides,  $K$ , can be determined by the thermal diffusivity,  $\alpha_d$ , the density,  $d$ , and the specific heat,  $C_p$ , using the following expression

$$K = \alpha_d C_p d. \quad (11)$$

The thermal diffusivity is experimentally measured by several techniques. The thermal flash method is currently the most prevalent technique for measuring the thermal diffusivity. As discussed previously, the specific heat of SiC can be expressed as a function of temperature. It may be reasonable to assume

a constant density due to the very low thermal expansion of SiC over the temperature range of interest.

The thermal conductivity of SiC has been investigated over the wide temperature range [29–34,37,43,46–58]. Fig. 7 shows a temperature dependence of the thermal conductivity of  $\beta$ -SiC over the temperature range 0–1800 K. At temperatures below 200 K, the thermal conductivity of SiC rapidly increases with increasing temperature due to the large contribution from the specific heat. Beyond the peak at  $\sim 200$  K, the thermal conductivity of SiC significantly decreases with increasing temperature due primarily to the phonon–phonon scattering (Umklapp scattering). However, the temperature dependence of phonon scattering in the presence of defects is not well understood and may be significant.

The magnitude of thermal conductivity depends on the grain size of SiC. Collins et al. [34] investigated the thermal conductivity of CVD SiC with varied grain sizes from 6.8 to 17.2  $\mu\text{m}$ . Below 300 K, the thermal conductivity of SiC monotonically increases with increasing its grain size. There should be no effect of temperature on grain boundary scattering and as temperature is increased

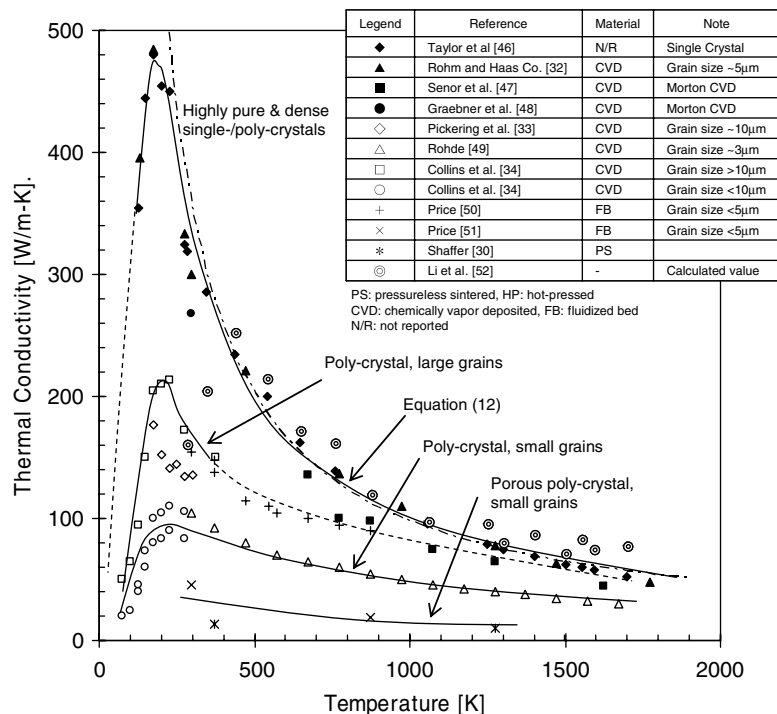


Fig. 7. Thermal conductivity of SiC at elevated temperatures.



phonon–phonon scattering dominates any scattering due to grain boundaries. Thus the difference in grain size becomes less important, with increasing temperature.

The thermal conductivity of SiC also depends on the nature of grain boundaries. It is well known that the impurities and/or micropores preferentially reside at grain boundaries. The presence of these defects at the grain boundaries as well as the grain boundaries themselves, result in a considerable reduction of thermal conductivity. In addition to the effect of grain boundaries and grain boundary defects on phonon scattering, the presence of ‘secondary phases’ at the grain boundaries for non-stoichiometric materials will also reduce thermal conductivity. For example, hot-pressed SiC exhibits considerably lower thermal conductivity when compared to other SiC forms because the thermal conductivity of this secondary phase, which originates from the sintering additives, is essentially lower than that of SiC. Moreover, Sigl et al. [37] reported that the decreased thermal conductivity for hot-pressed SiC is a function of the content of secondary YAG phase. Similarly, the thermal conductivity of sintered  $\alpha$ -SiC with residual sintering additives becomes lower. For these reasons only, thermal conductivity of CVD SiC, or perhaps single crystal, should be considered to accurately describe the thermal conductivity of a TRISO SiC layer.

It is reasonable to assume that the single crystal form of SiC, as compared to the other varieties, exhibits the highest thermal conductivity. However, high-purity and dense polycrystalline CVD SiC (such as Rohm and Haas Co.) exhibits practically the same conductivity as single crystal material, (in the orientation of its crystal growth axis). It is worth noting that the impurity content of the very high thermal conductivity CVD SiC materials are negligibly small (<5 ppm) and this material has near theoretical density ( $\sim 3.21 \text{ g/cm}^3$ ). Furthermore, it is noteworthy that the Rohm and Haas CVD SiC has a relatively small grain size ( $\sim 5 \mu\text{m}$  [32]) though still has similar thermal conductivity to single crystal even near room-temperature. It is noted that there is a very wide range in thermal conductivity even within CVD SiC grades. For example, the data reported by Price [51] on a fluidized bed SiC material (which should have been relatively pure) is about a quarter of the Rohm–Haas thermal conductivity at room-temperature. However, it is recognized that particular SiC material had many

micropores at grain boundaries and was also lower in density.

The phonon thermal conductivity of the SiC is theoretically expressed as a function of  $[A + BT]^{-1}$  with constants of  $A$  and  $B$ . The curve fitting to the single-crystal SiC data above 300 K yields an upper limit of the thermal conductivity of SiC,  $K_p$  (in W/m K)

$$K_p = [-0.0003 + 1.05 \times 10^{-5} T]^{-1}. \quad (12)$$

In parallel, a rigorous analysis using molecular dynamics simulation to evaluate directly the heat current correlation function has been developed [52]. The calculated trend agrees very well with the experimental results of the  $\beta$ -SiC single crystal at elevated temperatures  $>400 \text{ K}$ . At the low-temperature region (below 400 K), it is known that quantum effects become dominant on the heat transport behavior. Currently, no numerical model which considers this issue has been developed.

### 2.5.3. Thermal expansion

The interatomic spacing between the atoms of the SiC (as with other materials) is a function of temperature. At 0 K, these atoms have their lowest energy position, i.e., they are in the ground state. The increased stored energy resulting from increasing temperature causes the atoms to vibrate and move further apart. In short, the mean interatomic spacing increases, resulting in thermal expansion. In strongly bonded solids such as the SiC, the amplitude of the vibrations is small and the dimensional changes remain small. The comparatively lower thermal expansion coefficient of the carbides is therefore obtained due to the strong covalent bonding.

The coefficient of thermal expansion for  $\beta$ -SiC has been reported over a wide temperature range (Table 3) and is summarized in Fig. 8. A reference temperature of 298 K was used. The thermal expansivity of SiC has been measured by X-ray diffraction [28,62], dilatometry [33,51] and interferometry [65] techniques, or calculated from the induced residual stress [66]. The interferometry technique was only applied to measurement of the thermal expansivity for small ( $\sim 0.5 \text{ mm}$ ) hollow hemispherical TRISO SiC shells, which were fabricated by the fluidized bed method, over the temperature range 300–800 K [65]. The data obtained by the interferometric method are approximately in agreement with the results determined by the conventional dilatometry

Table 3  
Coefficients of thermal expansion of  $\beta$ -SiC

Authors	Method	$\Delta T$ (K)	$\bar{\alpha}$ ( $10^{-6} \text{ K}^{-1}$ )
Li and Bradt [28]	X-ray	RT–1273	4.45
Becker [59]	X-ray	RT–1473	6.2
Taylor and Jones [60]	X-ray	RT–1473	4.4
Clark and Knight [61]	X-ray	RT–1473	4.5
Suzuki et al. [62]	X-ray	RT–1173	4.3
Pickering et al. [33]	Dilatometer	RT–1373	4.4
Price [51]	Dilatometer	RT–1273	4.94
Popper and Mohyuddin [63]	Dilatometer	RT–1673	4.4
Kern et al. [64]	Dilatometer	RT–1273	4.8
Pojur et al. [65]	Interferometer	RT–780	4.38
Watkins and Green [66]	Residual stress	RT–1523	4.85
Shaffer [30]	Unspecified	RT–1523	4.78
Rohm and Haas Co. [32]	Unspecified	RT–1273	4.0

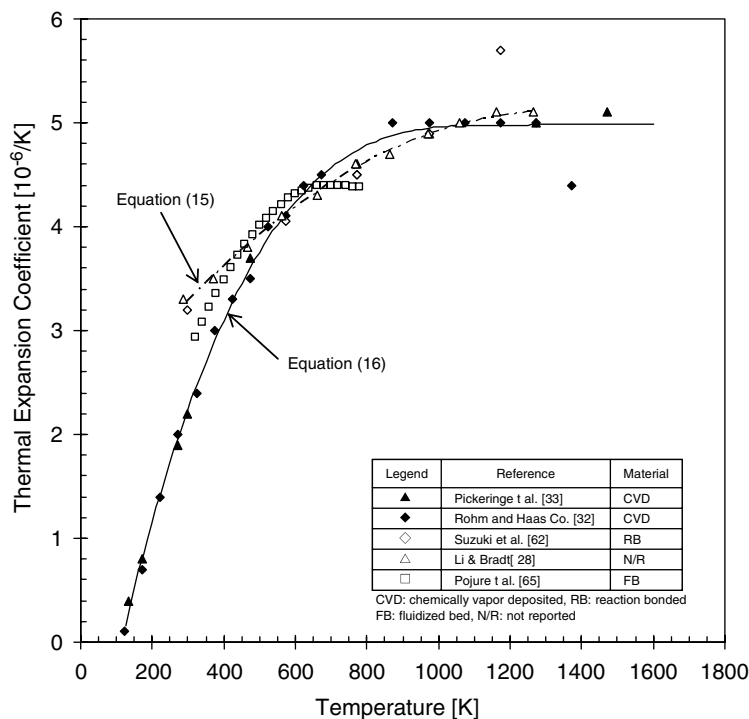


Fig. 8. Thermal expansivity of SiC at elevated temperatures.

at temperatures below 600 K, while the value at elevated temperatures 600–800 K was slightly lower. Some studies have claimed that the presence of impurities such as free carbon or silicon could reduce the thermal expansivity [4,67]. However, this mechanism must be very minor for TRISO fuel shells because the CVD SiC material currently in production is intrinsically pure. Intergranular micropores may have a minor effect on the thermal expansion behavior but this effect has not been specified.

The linear thermal expansion coefficient,  $\alpha$ , is theoretically obtained by

$$\alpha = \frac{d(\ln a)}{dT}, \quad (13)$$

where  $T$  and  $a$  are the temperature and lattice parameter, respectively. Then, a very good approximation is given by

$$\alpha = \frac{1}{a_0} \frac{da}{dT}, \quad (14)$$

where  $a_0$  is a lattice parameter at the reference temperature  $T_0$  ( $=298$  K). Substituting Eq. (7) into Eq. (14), Li and Bradt [28] estimated the coefficient of thermal expansion of 3C-SiC as

$$\alpha = 2.08 + 4.51 \times 10^{-3}T - 1.68 \times 10^{-6}T^2 (10^{-6}/\text{K}). \quad (15)$$

Eq. (15) is in good agreement with the experimental results over the temperature range 550–1273 K. However, at temperatures below 550 K, the thermal expansion coefficient of SiC is somewhat high. A more reliable correlation of the thermal expansion coefficient for 3C-SiC can be extracted from high-purity and crystalline CVD SiC (Rohm and Haas Co.) materials. Expressed as a third order polynomial as

$$\alpha = -1.8276 + 0.0178T - 1.5544 \times 10^{-5}T^2 + 4.5246 \times 10^{-9}T^3 (10^{-6}/\text{K}). \quad (16)$$

Eq. (16) is valid in the temperature range 125–1273 K. In contrast, the coefficient of thermal expansion at temperatures above 1273 K is assumed as constant  $5.0 \times 10^{-6}/\text{K}$ . The uncertainty of the recommended thermal expansion coefficient of 3C-SiC is  $\pm 10\%$  from 298 to 1273 K. The thermal expansion coefficient of 3C-SiC increases continuously from about  $2.2 \times 10^{-6}/\text{K}$  at 298 K to  $5.0 \times 10^{-6}/\text{K}$  at 1273 K, yielding an average value of  $4.4 \times 10^{-6}/\text{K}$  (298–1273 K). This is in good agreement with much of the published data (Table 3).

The thermal expansivity of SiC is significantly dependent on its crystal structure. The hexagonal SiC crystal, for example, exhibits an anisotropic behavior in thermal expansion between  $a$ - and  $c$ -axes [26,27]. In a similar manner, the thermal expansion coefficients for 4H-SiC [26] and 6H-SiC [27] can be determined as a function of temperature.

## 2.6. Electrical properties

As compared to the transition metal carbides, the covalent carbides are generally considered electrical insulators since they have no metallic bonding and their electrons are strongly bonded to the nucleus. However, the covalent carbides show semiconductor properties through conventional doping, depending primarily on the concentration and type of the doping element. For instance, aluminum and nitrogen as doping elements give p- and n-type semiconductor properties, respectively. CVD SiC is

known as a wide band-gap semiconductor with a wide range of resistivity from 1 to  $10^5 \Omega \text{ cm}$ , depending primarily on the level of doping impurities. Details on the semiconductor properties of SiC are found elsewhere [68,69].

## 2.7. Mechanical properties

### 2.7.1. Elastic constants

**2.7.1.1. Elastic modulus.** Various test methods: sonic resonance [2,32,42,57,70–82], tensile [83], flexural [29,32,51,84–88], nano-indentation [4,89–93], Vicker's indentation [94], and ring compression [7,85,95–97] techniques, have been applied to determine the elastic modulus of SiC.

Generally, a dense and high-purity SiC material, e.g., CVD SiC, exhibits the highest elastic modulus, however, the elastic modulus decreases with increasing porosity [79] or impurity concentration [89]. In contrast, neither grain size nor polytype was recognized as having a significant effect on the elastic modulus of SiC [79,98]. The effect of porosity on elastic modulus of various types of SiC at room-temperature is presented in Fig. 9. In the figure, the results obtained by various indentation techniques were excluded due to their inherently large uncertainties. The elastic modulus,  $E$ , at room-temperature can conventionally be expressed as an exponential function of porosity,  $V_p$

$$E = E_0 \exp(-CV_p), \quad (17)$$

where  $E_0$  is the elastic modulus of pore-free SiC and  $C$  is a constant. Assuming  $E_0 = 460$  GPa for Rohm and Haas CVD SiC, i.e., a polycrystalline, high-purity, and very dense SiC material, (assumed to be a pore-free SiC material), the constant  $C$  becomes 3.57. The uncertainty of the elastic modulus of SiC is  $\pm 10\%$  for  $V_p \leq 1\%$  and  $15\%$  for  $V_p > 1\%$ . No significant difference was obtained between the elastic moduli for alpha and beta polycrystalline SiC or among those of hot-pressed, sintered, and CVD materials.

The elastic modulus of SiC at elevated temperatures has been investigated by several authors [2,29,32,42,57,70–74,84–87] (Fig. 10). Most of these experiments were conducted in air, although many authors do not specify. In contrast, a few experiments were conducted in either vacuum or in an argon gas flow. In air, SiC is easily oxidized at elevated temperatures (depending on the oxygen partial pressure), forming a thin  $\text{SiO}_2$  layer (see

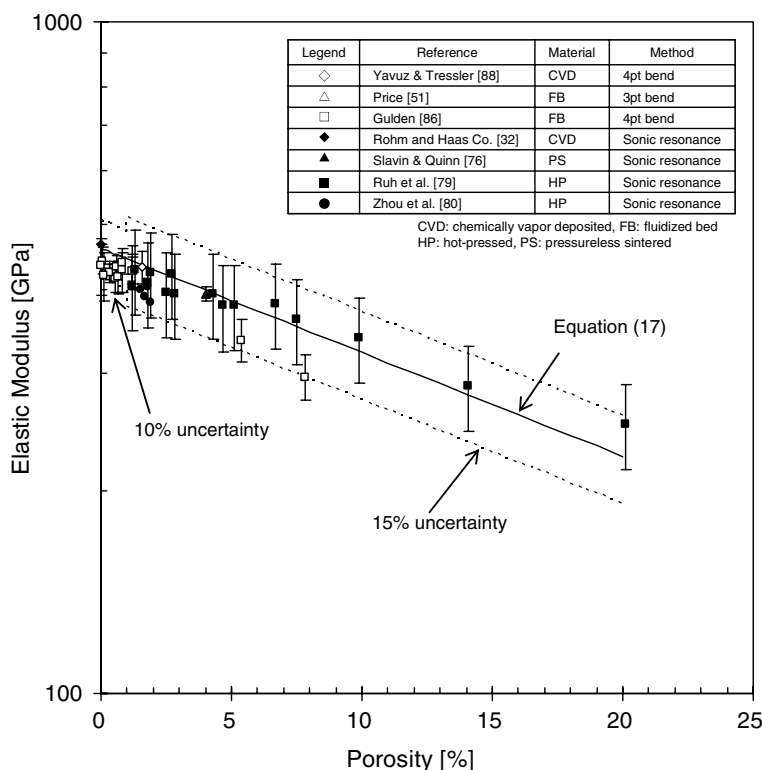


Fig. 9. The effect of porosity on elastic modulus of SiC.

detail in Section 2.8). However the overall bulk properties are essentially unchanged because the  $\text{SiO}_2$  forms only a near the surface film.

Silicon carbide exhibits a slight decrease in elastic modulus and increased internal friction at elevated temperatures. This trend is identical for most SiC polytypes with some exceptions [57,86]. In Fig. 10, the elastic modulus of reaction-bonded SiC (SCRB210, Coors Porcelain Co.) also decreases significantly at elevated temperatures [57]. The most likely mechanism is softening of residual silicon. However, the other reaction-bonded materials (Hexoloy KT, Carborundum Co. or NT-230, Norton Co.) did not show such a large reduction in elastic modulus at elevated temperatures. This implies that the distribution and fraction of residual silicon may have a significant influence on the softening behavior. In contrast, a remarkable reduction of the elastic modulus as a function of temperature for the early generation fluidized bed CVD SiC materials is believed to be due to grain boundary relaxation [86]. Specifically, this degradation was accelerated by increasing intergranular porosity. Xu et al. [7] identified the micropores preferentially

formed on the grain boundaries for the similar SiC material with fine ( $<1 \mu\text{m}$ ) crystal grains.

The elastic modulus at elevated temperatures has been empirically expressed by

$$E = E_0 - BT \exp\left(-\frac{T_0}{T}\right), \quad (18)$$

where  $B$  and  $T_0$  are constants characteristic of the material in units of GPa/K and K, respectively. An elastic modulus at 0 K is expressed as  $E_0$ . Here  $E_0$  is assumed to be identical to the room-temperature elastic modulus of 460 GPa. By fitting Eq. (18), we finally obtained the constants:  $B = 0.04 \text{ GPa/K}$  and  $T_0 = 962 \text{ K}$ . The characteristic temperature,  $T_0$ , is nearly identical to the Debye temperature of SiC. This relationship is very similar to that observed in several oxides [99]. The uncertainties of the high-temperature elastic modulus are  $\pm 2\%$  ( $0 \leq T \leq 1000 \text{ K}$ ) and  $\pm 5\%$  ( $1000 \leq T \leq 1800 \text{ K}$ ).

Elastic tensors of SiC are varied in the crystal structure. Complete sets of elastic tensors of 3C-, 4H- and 6H-SiC single crystals are given in Table 4. The elastic tensors for 3C-SiC identified by

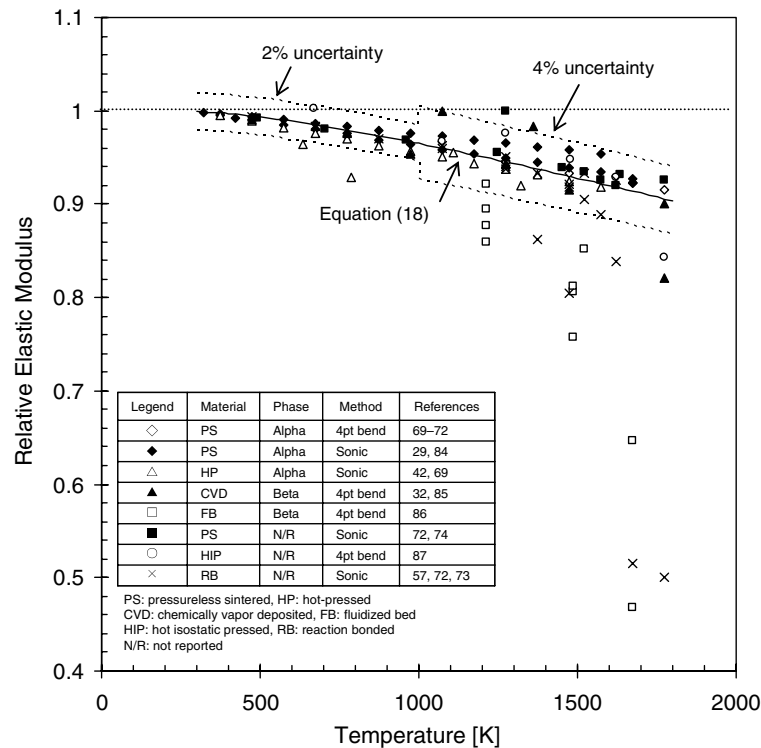


Fig. 10. Elastic modulus of SiC at elevated temperatures.

Tolpygo [100] are substantially different from reasonable estimates by the recent updates of sonic resonance data. The elastic tensor data of  $C_{11} = 511$ ,  $C_{12} = 128$  and  $C_{44} = 191$  GPa are now recommended.

**2.7.1.2. Poisson's ratio.** The Poisson's ratio of SiC is reported over a wide material range depending on the stoichiometry, crystallinity, impurity level, and porosity. The Poisson's ratio of CVD SiC with

excess residual silicon yields the lowest value ( $\sim 0.13$ ) [76,88]. A relatively low Poisson's ratio (0.14–0.20) has been identified for many of sintered forms of SiC [29,30,38,70,74–77,94,105–107] and reaction-bonded SiC [56,105,108]. In contrast, the highest value of 0.21 was typically obtained for pure CVD SiC, which best represents the TRISO fuel material [32].

The temperature dependence on the Poisson's ratio is at best very minor, although it may exist [29,70]. The Poisson's ratio of SiC is therefore assumed to be a constant ( $\sim 0.21$ ) over the temperature range of interest for fuels modeling.

Table 4  
Elastic constants of 3C-, 4H- and 6H-SiC at room-temperature

	3C [this study] <sup>a</sup>	3C [100] <sup>b</sup>	4H [101] <sup>c</sup>	6H [102] <sup>b</sup>	6H [101] <sup>c</sup>	6H [103] <sup>a</sup>	6H [104] <sup>d</sup>
$C_{11}$	511	352.3	507	464.5	501	502	479
$C_{12}$	128	140.4	108	112	111	95	97.8
$C_{13}$	–	–	–	55.3	52	–	55.3
$C_{33}$	–	–	547	521.4	553	565	521.4
$C_{44}$	191	232.9	159	137	163	169	148.4
$C_{66}$	–	–	–	–	–	203	190.6

\*Units in GPa.

<sup>a</sup> Sonic resonance.

<sup>b</sup> Theoretical.

<sup>c</sup> Brillouin scattering.

<sup>d</sup> Calculated from 3C-SiC data [100].

**2.7.1.3. Shear modulus.** The shear modulus of  $\alpha$ -SiC has been measured from room-temperature to 1773 K using the dynamic resonance method [2,29,70]. The shear modulus at room-temperature after correcting for porosity is  $\sim 195$  GPa. As with the high-temperature dependence of elastic modulus, the shear modulus of SiC decreases with increasing temperature. In contrast, only one experimental data-set is currently available for the more TRISO fuel relevant  $\beta$ -SiC. Yavuz and Tressler [88] reported the room-temperature shear modulus



of 191 GPa for CVD SiC, which was determined by the four-point bend technique. While it would be desirable to improve the  $\beta$ -SiC data-set, there currently appears no significant difference between the  $\alpha$ - and  $\beta$ -phases.

The shear modulus,  $G$ , can be alternately estimated with the following formula for an isotropic cubic crystal.

$$G = \frac{E}{2(1 + \nu)}. \quad (19)$$

Assuming an elastic modulus,  $E$ , of  $460 \pm 46$  GPa and a Poisson's ratio,  $\nu$ , of 0.21, a room-temperature shear modulus of  $191 \pm 19$  GPa is calculated.

The temperature dependence of shear modulus for SiC can be systematically obtained by applying Eq. (18) into Eq. (19).

### 2.7.2. Hardness

It is well known that SiC is among the covalent materials which possess the highest hardness. However, hardness is a complex property which involves both elastic and plastic deformation, crack initiation and propagation, and the development of new surfaces. Generally, hardness is dependent on the fabrication process, composition, and the presence of impurities. Moreover, it can be defined in terms of bonding energy, covalence level, atomic spacing, and by the parameters of fracture and deformation.

The hardness of SiC was investigated by Vicker's [29,32,71,72,76,78,80,82,84,91,94,106,109–113], Knoop [32,75,76,81] and nano-indentation techniques, [90–93] and summarized in Table 5. There appears to be no significant difference between Vicker's and Knoop hardness, while nano-hardness

gives slightly higher values. The nano-hardness is much more subject to the change in surface conditions because of the very small near-surface area of the material probed.

It is well known that the hexagonal  $\alpha$ -SiC single crystal shows anisotropy in its hardness due to the presence of its preferred slip system which is dependent on temperature [114,115]. This indicates that the hardness of SiC is essentially different for each polytype. However, any such difference should be minor for polycrystalline material such as CVD SiC.

Ryshkevitch [116] discussed the effect of porosity on the hardness of several oxide materials and found that Eq. (17) for elastic modulus can be satisfactory extended to the hardness evaluation. Fig. 11 shows the hardness of various SiC forms with varied porosity. By applying the equation, the following relationship is obtained

$$H_V = 27.7 \exp(-5.4V_p), \quad (20)$$

where  $H_V$  is the Vicker's hardness of SiC in GPa. The uncertainty of the room-temperature hardness of SiC as a function of porosity is  $\pm 7\%$ .

Fig. 12 exhibits the Vicker's hardness of SiC at elevated temperatures for various SiC materials. The general trends of hardness at elevated temperatures can be distinguished into two temperature regions: athermal temperature independent region and temperature dependent region. The hardness of SiC is nearly constant at lower temperatures, while it tends to rapidly decrease with increasing temperatures. The transition temperature has been defined as a ductile-to-brittle temperature [94]. It is interesting to note that the ductile-to-brittle transition temperature increases with increasing

Table 5  
Vickers, Knoop and nano-indentation hardness of SiC at room-temperature

Material	Sintering additives	Vickers hardness (GPa)	Knoop hardness (GPa)	Nano hardness (GPa)	References
Sintered $\alpha$ -SiC <sup>a</sup>	B, C	24.9–26.7	22.4–27.4	n/a	[71,72,75,78,82,84,112]
Hot-pressed $\alpha$ -SiC <sup>b</sup>	Al <sub>2</sub> O <sub>3</sub> , WC, Co	19.3	22.3	n/a	[75,106]
Hot isostatic pressed $\alpha$ -SiC	AlN	25.0–27.3	n/a	n/a	[109]
CVD $\beta$ -SiC <sup>c</sup>	–	20.7–24.5	24.5	32.5–40.6	[32,110,90–93]
Sintered $\beta$ -SiC	B, C	21.1–23.9	20.9	n/a	[76,106]
Hot-pressed $\beta$ -SiC	Al	26.7–29.7	n/a	n/a	[109]
Hot-pressed $\beta$ -SiC	Al <sub>2</sub> O <sub>3</sub> , RE <sub>2</sub> O <sub>3</sub> (RE = La, Nd, Y, Yb)	3.4–21.2	n/a	n/a	[80]

<sup>a</sup> Carborundum Co., Hexoloy-SA.

<sup>b</sup> Norton Co., NC-203.

<sup>c</sup> Morton Advanced Materials (presently Rohm and Haas Advanced Materials).

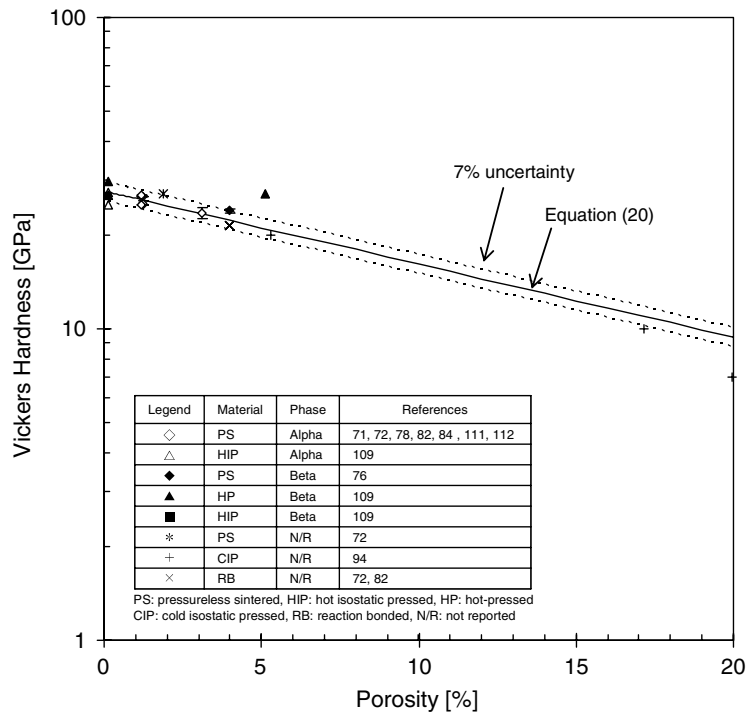


Fig. 11. The effect of porosity on Vickers hardness of SiC.

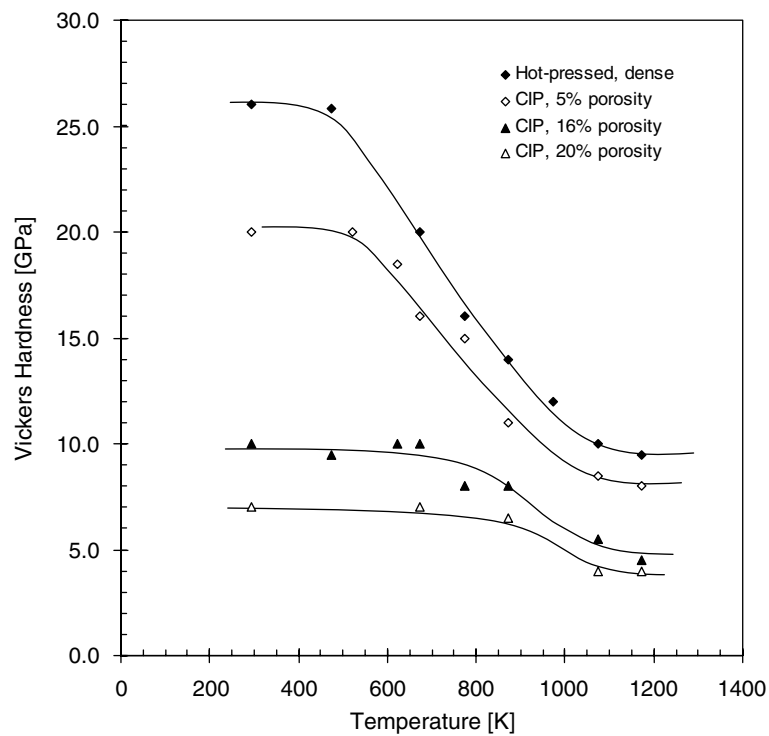


Fig. 12. Vickers hardness of SiC at elevated temperatures.

porosity. However, of particular importance is that these SiC materials are fundamentally porous, containing sintering aids as residual impurities. The significant decrease of the hardness at high-temperatures is attributed primarily to the segregation at the grain boundaries due to the presence of impurities. Therefore, Fig. 12 should be used with care, although the general trend may be consistent with high-purity and dense forms of  $\beta$ -SiC. Currently there is no high-temperature data reported for high-purity CVD-SiC.

### 2.7.3. Fracture toughness

The fracture toughness of SiC has been widely investigated by various test techniques: micro- and nano-indentation [32,71,76,78,87,90–92,94,110,112,113,117,118], surface crack in flexure (SCF) [29,71,72,77,82,105,109,112,119–123], double cantilever beam (DCB) [117], double torsion (DT) [75,106,117,124], single edge notched beam (SENB) [54,58,88,117,120,121,125–132], Chevron notched

beam (CNB) [121], and fractography [120]. The representative values determined by each test are summarized in Table 6. The Vicker's and SCF methods result in slightly lower fracture toughness, as compared to the fractography method. The large scatter of the fracture toughness data (e.g., Vicker's indentation data) is due primary to the effect of grain size as discussed later. However, when the scattering is taken into account the mean fracture toughness is similar.

The effect of grain size on the fracture toughness of SiC is shown in Fig. 13. The fracture toughness is peaked for a grain size of approximately 1–5  $\mu\text{m}$ . The same is true of the fracture energy, as determined by the SENB [133,134], DCB [134–136] and work-of-fracture (WOF) [136] methods, for sintered SiC with non-cubic structure (plotted together in Figs. 2 and 13). Rice et al. [137] demonstrated the grain-size dependence of fracture energy for non-cubic ceramics using an analytical model. They concluded that the likely mechanism is microcrack

Table 6  
Fracture toughness data of SiC at room-temperature

Material	Sintering Additives	Fracture Toughness ( $\text{MPa m}^{0.5}$ )	Method	References
Sintered $\alpha$ -SiC <sup>a</sup>	B, C	2.6–3.4	Vickers	[71,78,112]
		2.0–3.4	SCF <sup>d</sup>	[71,72,77,82,112,120,121]
		3.01	DT <sup>e</sup>	[72]
		3.9–5.4	SENB <sup>f</sup>	[54,58,120,121]
		2.91	CNB <sup>g</sup>	[121]
		4.7	Fractography	[120]
Hot-pressed $\alpha$ -SiC <sup>b</sup>	$\text{Al}_2\text{O}_3$ , WC, Co	3.8–4.7	Vickers	[118]
		3.9–4.4	SCF <sup>d</sup>	[77,105]
		3.8–5.2	DT <sup>e</sup>	[72,82,124]
		4.5–5.1	SCF <sup>d</sup>	[109]
Hot isostatic pressed $\alpha$ -SiC CVD $\beta$ -SiC	AlN –	2.4–5.1	Vickers	[32,90–92,110,117]
		2.7	SCF <sup>d</sup>	[32]
		3.8–4.1	DCB <sup>h</sup>	[117]
		3.7	DT <sup>e</sup>	[117]
		3.4–4.4	SENB <sup>f</sup>	[88,117,125]
		3.46(0.16) <sup>c</sup>	Vickers	This work
		3.20(0.12) <sup>c</sup>	CNB <sup>g</sup>	This work
		2.6–3.0	Vickers	[76,113]
		3.1	DT <sup>e</sup>	[106]
Sintered $\beta$ -SiC	B, C	2.3	SENB <sup>f</sup>	[126]
		2.5–4.5	SCF <sup>d</sup>	[109]
		3.5	SCF <sup>d</sup>	[109]
		3.7	SENB <sup>f</sup>	[109]
Hot-pressed $\beta$ -SiC	Al			
Hot isostatic pressed $\beta$ -SiC	AlN			
Reaction-bonded $\beta$ -SiC	Al			

<sup>a</sup> Carborundum Co., Hexoloy-SA.

<sup>b</sup> Norton Co., NC-203.

<sup>c</sup> Numbers in parenthesis are one standard deviation.

<sup>d</sup> SCF: Surface crack in flexure.

<sup>e</sup> DT: Double torsion.

<sup>f</sup> SENB: Single-edge notched beam flexure.

<sup>g</sup> CNB: Chevron notched beam.

<sup>h</sup> DCB: Double cantilever beam.

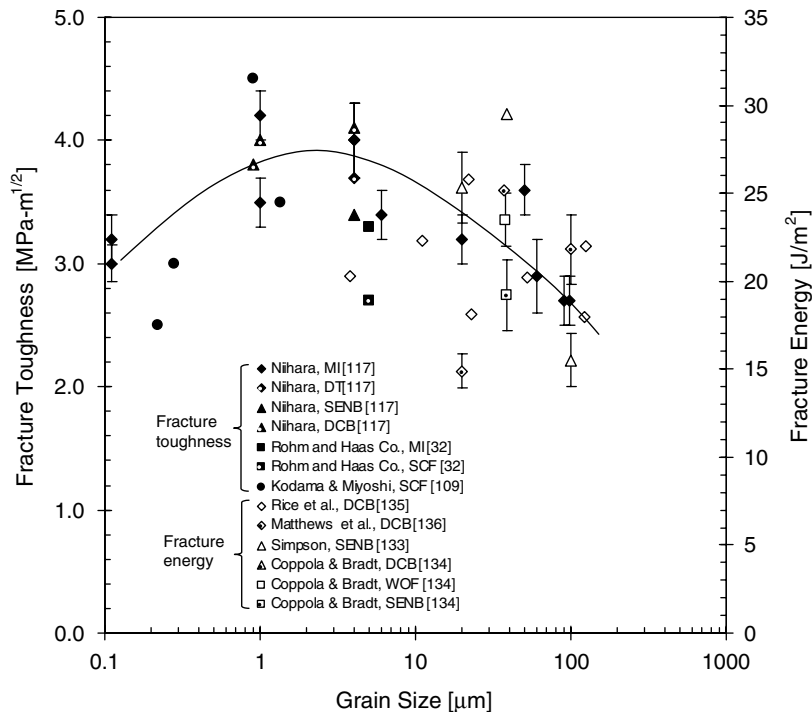


Fig. 13. Fracture toughness and fracture energy of SiC as a function of grain size.

formation due to the combined effects of the applied stress and the local micro-stresses induced by thermal expansion anisotropy, although the thermal expansion anisotropy is potentially small for isotropic 3C-SiC. However, it is known that a high internal residual stress can be induced during CVD processing [138]. Niihara [117] speculated that the grain size dependence of fracture toughness for small grain CVD SiC is due primarily to microcrack formation by the residual internal stress accumulated due to the CVD processing. Another possible explanation for such a decrease is the presence of micropores on grain boundaries. Such a degradation mechanism is similar to the decreases observed in thermal conductivity and Young's modulus. In contrast, the decrease of fracture energy for large grain SiC is attributed to the decreasing applied strain energy required to form each microcrack. Further investigation may be necessary to validate these mechanisms.

Fig. 14 shows the fracture toughness of  $\beta$ -SiC at elevated temperatures. The fracture toughness of SiC remains nearly constant with temperature for sintered and reaction-bonded SiC materials, while it increases at elevated temperatures for CVD SiC. Henshall et al. [140] also reported fracture tough-

ness increasing with temperature for single crystal  $\alpha$ -SiC near 1073 K and suggested the responsible mechanism was small plastic deformation at the crack tip. This mechanism may be satisfactorily extended to CVD SiC, as a substantial increase in plasticity has been confirmed at elevated temperatures [115]. In addition, the effect of stress relaxation at high temperatures may be responsible for the increase in fracture toughness. However, this effect seems minor as an annealing experiment (10 h at 1773 K) indicated no clear effect [115].

The only result on high-temperature fracture energy of reaction-bonded SiC was provided by Stevens [139]. Fracture energy increased with increasing temperature approaching a constant (Fig. 14). This increase may be attributed to short-term crack healing by softened excess silicon rather than the plastic deformation induced at crack tips.

#### 2.7.4. Fracture strength

The two-parameter Weibull statistical treatment is often used to evaluate statistical strength of brittle materials. Two key parameters: the Weibull modulus,  $m$ , and the Weibull characteristic strength,  $\sigma_0$ , have been determined for  $\beta$ -SiC by various test techniques (Table 7). It is noted that the extremely high

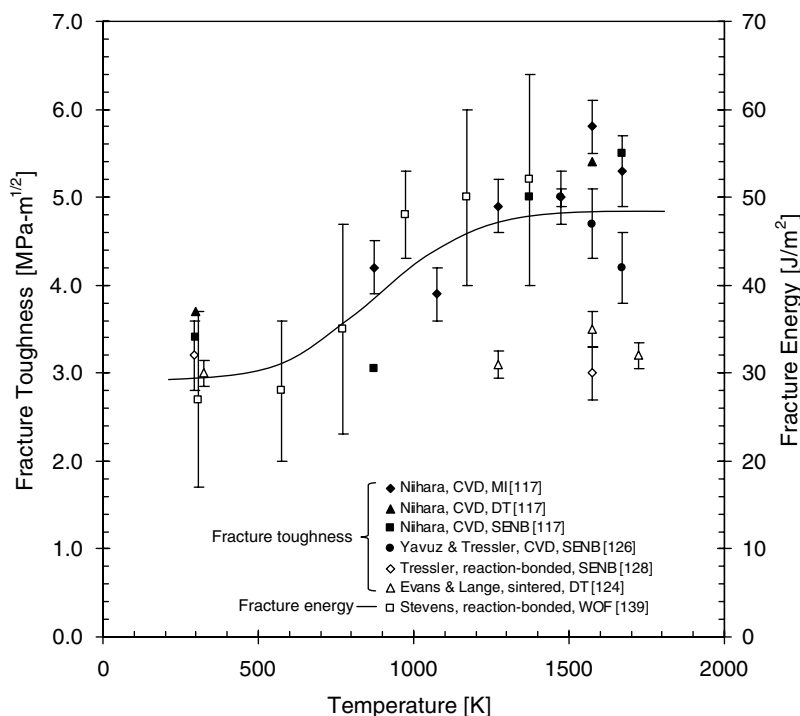


Fig. 14. Fracture toughness and fracture energy of SiC at elevated temperatures.

characteristic strength obtained by O-ring compression or hemispherical bend tests is likely due to inadequate analytical procedures and/or extremely tiny fracture volume, as pointed out by Hong et al. [148]. It is recommended that the circumferential tensile strength of spherical coatings is best determined using test methods such as internal pressurization which applies uniform loading over the entire sample surface.

**2.7.4.1. Weibull modulus.** The Weibull modulus of SiC at room-temperature spans an unfortunately large range, from 2 to 12, depending not only on the material but the condition of the SiC material, the test method, and the population of samples used. A possible explanation for the lowest value obtained (by Yavuz and Tressler [88]) is the residual stresses induced during the CVD processing. Also possible is that large amounts of unreacted silicon were present in their samples, which primarily segregates along grain boundaries and may also induce internal stresses.

Comparatively larger Weibull modulus values ( $m = 7$ –11) are often measured by flexural and tensile tests, while the lower values ( $m = 3$ –9) are

typically obtained using the ring compression test. Cockeram [85] has assumed that the flaw distributions are quite different between a flexural bar and a small tubular (ring) specimen. The lower  $m$  value obtained by the ring compression test was therefore considered primarily a consequence of the altered flaw distributions. Additionally, irregularity of ring specimens [96] and surface roughness [141] significantly impacts failure probability. Recently, Byun et al. [141] measured the Weibull modulus for the prototypical size TRISO SiC particles by both the diametral loading and the internal pressurization techniques, generating the most applicable data for the TRISO SiC layer. In summary, the Weibull modulus for the TRISO SiC particle is in the range of 4–6.

The Weibull modulus of SiC at elevated temperature is given in Refs. [72,85,125,126]. However, no systematic temperature-dependence has yet been determined. Therefore, a constant Weibull modulus is assumed over the wide temperature range of interest.

**2.7.4.2. Weibull characteristic strength.** The room-temperature failure strength of  $\beta$ -SiC has been



Table 7  
Weibull modulus and Weibull characteristic strength of  $\beta$ -SiC

Material	Weibull modulus	Characteristic strength (MPa)	Test method	References
CVD SiC (Bulk)	11	424	4pt bend	[32]
	9.9	365	4pt bend	[93]
	8	—	4pt bend	[72]
	1.9–4.5 <sup>d</sup>	205–493 <sup>d</sup>	4pt bend	[88,126]
	7.6–13.8	212–501	4pt bend	[85]
	6.7	421(69) <sup>f</sup>	4pt bend	This work
	6.7–7.3	478–532	O-ring compression	[85]
CVD SiC (Small tube) <sup>a</sup>	4.9	405	Diametral compression	This work, [141]
	5.0–9.7	312–448	Internal pressurization	This work, [141]
CVD SiC (Particle) <sup>b</sup>	4.1–6.6	659–1412	O-ring compression	[7]
	3.0–5.6	1490–1730	O-ring compression	[96]
	4.8–9.4	1050–1890	O-ring compression	[95]
	4.0–9.0	980–2200	C-ring compression	[95]
	3–8	620–720	Hemisphere bend	[142]
	6.6–8.4	1870–3170	Hemisphere bend	[143]
	5.4	—	Unspecified	[144]
	5.8–7.5	356–427	Diametral compression	This work, [141]
	4.3–6.2	222–321	Internal pressurization	This work, [141]
Sintered SiC <sup>c</sup>	11.0	362	4pt bend	[76]
	12.0	505	Tensile	[125]
Hot isostatic pressed SiC	6.6	556	4pt bend	[145]
Reaction bonded SiC	12.0 <sup>e</sup>	230 <sup>e</sup>	4pt bend	[147]

<sup>a</sup> A SiC layer was formed over the graphite rod then the graphite core was burned off before testing.

<sup>b</sup> An inner carbon layer was burned off before testing.

<sup>c</sup> Sintering additives: B, C.

<sup>d</sup> Free silicon: 1.7 ~ 6.3%.

<sup>e</sup> Free silicon: 13%.

<sup>f</sup> A number in parenthesis is one standard deviation.

reported to vary from 200 to over 3100 MPa. The failure strength of SiC particles is typically much larger than that of the SiC bulk form. Such a large variation is due primarily to the specimen size effect related to the Weibull nature of failure.

It is well known that the strength at the inner weakest flaw determines the overall strength of these brittle materials. The flaw population and distribution are strictly dependent on volume as expressed by the Weibull distribution function. Byun et al. [146] investigated the size effect on tensile hoop strength for tubular alumina specimens using the internal pressurization and diametrical loading test techniques. A major conclusion in his work is that the failure strength of the tubular brittle specimens can be determined by the effective surface area, while the volume criterion was a major conclusion of the CEGA report [1] for SiC materials. The fact that the fracture often initiated at the small flaws near the specimen surface [76] would support this result. These surface flaws have been directly associated with surface roughness. Evans et al. [142] evaluated the effect of the surface roughness on flexural

strength of hemispherical particles. Superior failure strength was achieved by reducing surface roughness by controlling the conditions of deposition of the coating. This work further supports the argument that effective surface area is primary in the failure of coatings.

Assuming an identical surface flaw distribution, the Weibull statistical theory suggests that the strength of the small ring specimen would become much higher than that of a flexural bar. Indeed, a one-order of magnitude higher Weibull characteristic strength has been obtained by ring compression testing [85]. However, the actual failure behavior would be much more complicated because the flaw distribution is substantially more complex than a single flaw. Byun et al. [141] measured statistical strength of a prototypical TRISO SiC particle fabricated in a fluidized bed being used for TRISO fuel fabrication. The specimen size effect was considered using a finite element model leading to an estimate of the strength of the SiC coating. A Weibull characteristic strength of 220–320 MPa was recommended.

It is apparent that no significant degradation of strength for CVD SiC occurs up to a temperature of 1773 K, in fact an increase above 1373 K is apparent (Fig. 15) [86,117]. This increase would be closely linked to the brittle-to-ductile transition in fracture toughness. In contrast, the short-term improvement of the failure statistics at intermediate temperatures for reaction bonded SiC is thought to be due to flaw healing and partial relief of residual stress (due to oxidation and increased ductility of the residual silicon phase at high temperatures). However, the presence of impurities would eventually cause severe deterioration at much higher temperatures because of reduced susceptibility of load at the grain boundaries. Hot-pressed SiC also degraded its strength at elevated temperatures due to the presence of excess oxide phase. In any event, the effects observed in these non-CVD materials should not be considered for TRISO coatings.

## 2.7.5. Thermal creep

**2.7.5.1. General overview.** Primary and steady-state creep deformations have been reported in the literature for CVD SiC (high-purity and polycrystalline  $\beta$ -SiC) [149,150]. Steady-state creep rates for stoichiometric polycrystalline materials have been measured only above  $\sim 1673$  K, because they are typically too small to be measured by ordinary experimental techniques below  $\sim 1673$  K, where primary creep dominates total creep deformation [150,151]. Steady-state creep in SiC is highly dependent on crystallographic orientation as found from both experimental observations and proposed physical mechanisms [150]. Therefore, the operating temperature for steady-state creep depends very strongly on crystallographic characteristics of the material and the loading direction relative to crystallographic orientations. Moreover, the primary creep deformation behavior also depends strongly

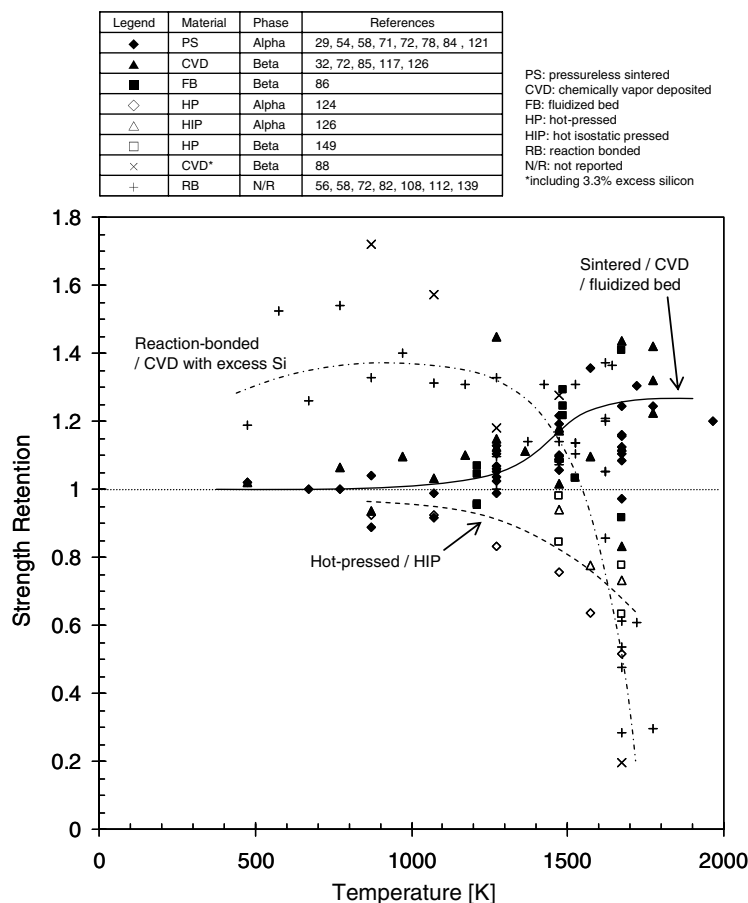


Fig. 15. Tensile, flexural and ring compression strengths of SiC at elevated temperatures. The relative strength is defined as high-temperature strength normalized by room-temperature strength.

on quality of the materials [152], often concealing the contribution from the steady-state creep in stress relaxation-type experiments [153].

There have been a large number of research reports published regarding creep behavior of materials often termed ‘SiC’ such as reaction-bonded, hot-pressed, and liquid phase-sintered SiC-based materials. Since, in most cases, the creep deformation of these materials are governed by the grain boundary-related deformation accommodated by the secondary phases or diffusion associated with sintering additives, creep data for those impure SiC materials must be differentiated from those for high-purity TRISO-relevant SiC materials. A review of creep behaviors of stoichiometric CVD SiC has been provided by Davis and Carter [154]. Additionally, the creep data compilation for SiC-based ceramics of various grades by Wang [155] may be useful.

**2.7.5.2. Primary creep.** Primary creep of CVD SiC occurs immediately upon loading and tends to saturate with time. The strain by primary creep in CVD SiC widely varies depending on quality of materials, as the proposed responsible mechanisms are related with stress-induced evolution of residual microstructural defects of various kinds, limited basal slip under polycrystalline constraints, and grain rearrangement. The primary creep strain generally obeys the following relationship [152]

$$\varepsilon_c = A_p(\sigma/G)^n(t/\tau)^p, \quad (21)$$

where  $A_p$ ,  $p$ , and  $\tau$  are creep parameters, and  $t$  is time elapsed. Analyzing the result published by Carter et al., one obtains the creep parameters  $n = 1.63$ ,  $A_p = 29$ ,  $p = 0.081$ , and  $\tau = 0.0095$  s for the temperature of 1923 K. It is shown that, in severe loading condition, primary creep strain in CVD SiC can reach as high as  $\sim 1\%$  at 1923 K. Note that these parameters are for the loading orientation of  $45^\circ$  from the CVD growth axis, the direction in which the most prominent creep strain is anticipated.

Primary creep behavior has also been studied for commercial and developmental CVD SiC fibers under a tensile loading [151]. The fiber materials were Textron SCS-6, SCS-9, and a developmental 2-mil fibers, made up of one to several CVD SiC layers deposited onto a carbon core. Morscher et al. [154] reported that (i) primary creep strain was proportional to stress ( $n = 1$ ), (ii) a time exponent,  $p$ , nearly independent of stress and temperature which fell into a range of 0.2–0.4, and (iii)

where  $A_p$  was strongly dependent on deposition quality of the material and the temperature. They determined the activation energy for the responsible mechanism to be 290–740 kJ/mol based on the temperature dependent normalized creep strain data, and also pointed out that the substantial, material dependent compositional deviation from stoichiometry had caused the large variation in activation energy. The activation energy data may be useful to estimate an extrapolated range of primary creep strain at different temperatures from Eq. (21).

**2.7.5.3. Steady-state creep.** The only data on steady-state creep deformation rates for CVD SiC known to the authors have been reported by Gulden and Driscoll [149], and Carter et al. [150].

The data by Gulden and Driscoll exhibited creep rates proportional to the applied flexural stress in a temperature range of 1655–1743 K, with an activation energy of  $640 \pm 88$  kJ/mol, implying grain boundary diffusion of carbon atoms to be the controlling mechanism [156]. Although details of the material used by Gulden and Driscoll are not known, it is very likely that the suspected non-stoichiometry in their material had governed the creep, as the measured creep rates are by more than an order of magnitude greater than those determined by Carter et al.

Carter et al. tested CVD SiC (with  $\sim 500$  ppm metallic impurity and no detectable N, Al, B) in a uni-axial compressive configuration at 1573–2023 K in a stress range of 69–220 MPa in argon. They observed no measurable steady-state creep up to 2023 K with the stress axis parallel to the deposition direction, which was confirmed to be the preferred  $\langle 111 \rangle$  orientation. With the stress axis  $45^\circ$  inclined from the deposition direction, they were able to measure the steady-state creep rates at 1673–1923 K and 110–220 MPa, and the data is replotted in Fig. 16. Fitting a general power-law creep equation,

$$\dot{\varepsilon}_c = A_s(\sigma/G)^n \exp(-Q/k_b T) \quad (22)$$

to the experimental data, steady-state creep parameters were determined as  $A_s = 2.0 \times 10^3$ ,  $n = 2.3$ , and  $Q = 174$  kJ/mol. In Eq. (22),  $A_s$  is a constant,  $\sigma$  is applied stress,  $G$  is shear modulus,  $n$  is stress exponent,  $Q$  is activation energy for the rate-determining physical process,  $k_b$  is Boltzmann constant, and  $T$  is absolute temperature. Carter et al. have attributed the creep deformation below 1923 K to

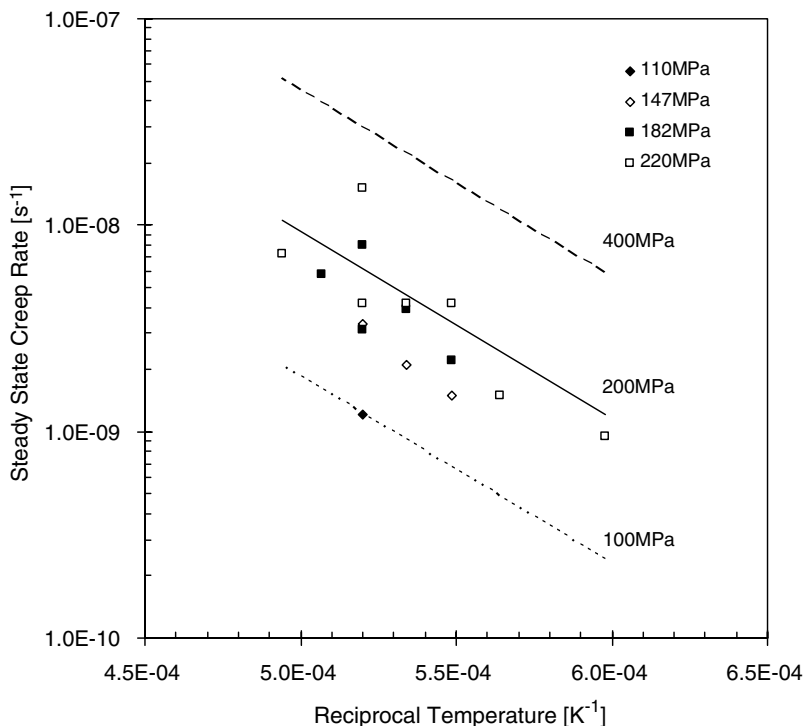


Fig. 16. Steady-state creep rate of CVD SiC at the temperatures below 1923 K.

dislocation glide, whereas that at 1923 K was provisionally attributed to climb-controlled glide.

The creep parameters above imply that the steady-state creep rates of  $\sim 10^{-10} \text{ s}^{-1}$  and  $\sim 10^{-9} \text{ s}^{-1}$  are expected at 1473 K and 1673 K, respectively, at a stress of 200 MPa. However, it should be noted that the experiment by Carter et al. was conducted in a condition that allows the highest steady-state creep rates for CVD SiC in terms of crystallographic orientation and therefore can be regarded as the greatest creep case. Indeed they did not detect steady-state creep even at 2023 K when loaded along the deposition direction. Moreover, Ohji and Yamauchi [157] also reported the lack of steady-state creep under tensile loading of 200 MPa at 1673 K over the period of  $>10^4 \text{ h}$  for SiC sintered with B and C, a material that is anticipated to exhibit inferior creep performance to high-purity CVD SiC.

A very significant crystallographic orientation effect on creep rate has also been reported by Corwan [158] for the 6H-SiC single crystal. He observed steady-state creep rates exceeding  $10^{-7} \text{ s}^{-1}$  at temperatures as low as 1073 K at a compressive stress of 200 MPa when loaded at  $45^\circ$  from [0001], whereas a similar creep rate was achieved at 2123 K when loaded along [0001]. Since the

(0001) basal plane in 6H structure corresponds to the (111) in 3C, a similar crystallographic orientation effect could be expected for the 3C-SiC single crystal.

## 2.8. Chemical properties

Silicon carbide is a non-oxide compound and the oxidation at high-temperatures therefore becomes a critical issue. Many studies on the oxidation behavior of SiC have been conducted [159–174] (see also Refs. [175,176] for recent reviews of the oxidation of SiC). The oxidation of SiC is generally divided into two regions: passive and active oxidations, with a broad transition band.

At high oxygen partial pressures and high temperatures, SiC reacts with oxygen to form a  $\text{SiO}_2$  surface scale, accompanied with significant mass gain (passive oxidation).



The structure of the resultant  $\text{SiO}_2$  scale is amorphous at the temperatures below 1673 K. In contrast, the crystallization rate from amorphous  $\text{SiO}_2$  to cristobalite has a maximum value around

1950 K, and the cristobalite is therefore more stable at higher temperatures. The Pilling–Bedworth ratio, which is defined as the ratio of the volume of the resultant oxide to the consumed substrate volume, i.e., the volume ratio between the SiO<sub>2</sub> scale and the SiC substrate, is  $\sim 1$  (forming a good bond at the interface with a very small strain gap). In contrast, the diffusion rate of oxygen in the SiO<sub>2</sub> scale is very low compared with other oxides. The SiO<sub>2</sub> scale therefore effectively acts as a protective layer to prevent further oxidation.

The oxidation kinetics of SiC is dependent on many factors: atmosphere, temperature, oxygen partial pressure, microstructure, etc. The oxidation mechanism in a dry atmosphere can be classified into linear-parabolic or parabolic behavior below the melting point of cristobalite ( $T_m = 2001$  K) [164]. Luthra [167] suggested that the passive oxidation of SiC is a mixed control mechanism, influenced both by an interface reaction and diffusion. However, the primary rate-controlling process for passive oxidation is still considered to be diffusion of oxygen through the growing oxide scale. Oxygen can diffuse through SiO<sub>2</sub> via two mechanisms: (1) interstitial (nominally molecular) oxygen diffusion through the free volume of the silicate structure and (2) network oxygen ion diffusion through the SiO<sub>4</sub> tetrahedral network [170,171]. A recent study [163] identified that the high-temperature transition from interstitial-dominant ( $<1673$  K) to network-dominant ( $>1673$  K) oxygen transport is only observed for amorphous SiO<sub>2</sub> scales, while the cristobalite scale did not show such a transition. This fact can explain a comparatively lower oxidation rate obtained below 1673 K. It was also identified that there is no significant difference between the rates of molecular oxygen diffusion in cristobalite and in amorphous SiO<sub>2</sub>, although the possible mechanism is believed to be the change of the diffusion rate of oxygen in the SiO<sub>2</sub> scale due to the crystallization from amorphous SiO<sub>2</sub> to  $\beta$ -cristobalite [159,166].

The oxidation process is accelerated by the presence of impurities and residual sintering additives which affect the microstructure of the protective SiO<sub>2</sub> scale [177]. In contrast, significant differences have been observed in the interaction of oxygen with different polytypes and different surface orientations of single crystal SiC [165,169]. The oxidation kinetics also depends on the type and size of the SiC form, e.g., sintered body or powder. The SiC powder can be oxidized in air at 973 K [174]. Moreover,

the formation of SiO<sub>2</sub> bubbles at extremely high temperatures can be closely related to the oxidation mechanism of SiC [164,172]. The transition from passive oxidation to bubble formation depends on the oxygen partial pressure and test temperature. The linear and parabolic oxidation rates were accelerated by the bubble formation. Water vapor can further accelerate the oxidation of SiC [162,173] extending the linear kinetic region and increasing the parabolic rate constant.

At low oxygen partial pressures and very high temperatures, SiC readily decomposes to SiO and CO gases without forming a protective SiO<sub>2</sub> scale (active oxidation).



According to Schneider et al. [161], there is a wide gap in oxygen pressure required for the active-to-passive oxidation transition. The active-to-passive oxidation transition is closely dependent on the impurity content in the SiC form. For instance, the partial oxygen pressure required to initiate the active oxidation of a sintered SiC, which possesses slight residual sintering aids as impurities, is  $\sim 10^4$  times higher than that of pure CVD SiC [160]. The active oxidation rates increases with increasing oxygen partial pressure [164,168].

Some basic oxides, e.g., PbO and Na<sub>2</sub>O, can dissolve the protective SiO<sub>2</sub> scale to form silicates [178]. Silicon carbide is also corrosive in Na<sub>2</sub>SO<sub>4</sub> [179,180] and a mixture of Na<sub>2</sub>CO<sub>3</sub> and KNO<sub>3</sub>. Moreover, SiC reacts readily with chlorine and sulfur above 1173 and 1273 K, respectively [181]. In contrast, SiC is chemically inert to HCl, H<sub>2</sub>SO<sub>4</sub>, HF, NaOH, and a mixture of HF and HNO<sub>3</sub>, even if the oxidizing acids are heated [181].

### 3. Effects of irradiation on SiC

#### 3.1. Irradiation-induced microstructure and swelling

The neutron-induced swelling of SiC has been well studied for low and intermediate temperatures ( $\sim 293$ – $1273$  K). Originally this material was investigated in support of nuclear fuel coating [4,182–189] and more recently for various nuclear applications such as structural SiC composites [47,62,190–201]. Before proceeding, it is important to distinguish neutron-induced effects in high purity materials, such as single crystal and most forms of chemically vapor deposited (CVD) SiC, with those of lower purity forms such as hot pressed, sintered, liquid



phase converted, or polymer-derived SiC. It is well understood that the presence of significant impurity levels in these materials leads to unstable behavior under neutron irradiation [192,195,202,203], as compared to stoichiometric materials, which exhibit remarkable radiation tolerance. This discussion and data for this section refers only to stoichiometric, near-theoretical density SiC, unless otherwise specified.

The irradiation-induced microstructural evolution of CVD SiC is roughly understood and has been reviewed recently by Katoh et al. [204] (the recent update of the microstructural evolution map is shown in Fig. 17). However, the contribution of the defects themselves to the swelling in SiC is less understood. Below several hundred Kelvin the observable microstructure of neutron irradiated SiC is described as containing ‘black spots’ which are most likely tiny clusters of self-interstitial atoms in various indeterminate configurations. For irradiation temperatures less than about 423 K, accumulation of strain due to the irradiation-produced defects can exceed a critical level above which the crystal becomes amorphous. This has been shown for both self-ion irradiation and under fast neutron irradiation [206–208]. As shown by Katoh et al. [206], the swelling at 323 K under self-ion irradiation

increases logarithmically with dose until amorphization occurs. The swelling of neutron- and ion-amorphized SiC has been reported to be 10.8% for 343 K irradiation [208]. However, there is evidence that the density of amorphous SiC will depend on the conditions of irradiation (dose, temperature, etc.) [209].

For temperatures above the critical amorphization temperature (423 K) the swelling increases logarithmically with dose until it approaches saturation, with a steady decrease in the saturation swelling level with increasing irradiation temperature. The dose exponents of swelling during the logarithmic period are in many cases close to 2/3, as predicted by a kinetic model assuming planar geometry for interstitial clusters [210,211]. This temperature regime is generally referred to as the point-defect swelling regime and can be roughly set between 423 and 1273 K. As an example of how these ‘black spot’ defects mature in the point-defect swelling regime, Fig. 18 shows neutron irradiated microstructures at 573 and 1073 K for doses consistent with a saturation in density. While these microstructural features are generically classified as ‘black spots’, those defects formed at 1073 K are clearly coarser as compared to those formed under 573 K irradiation.

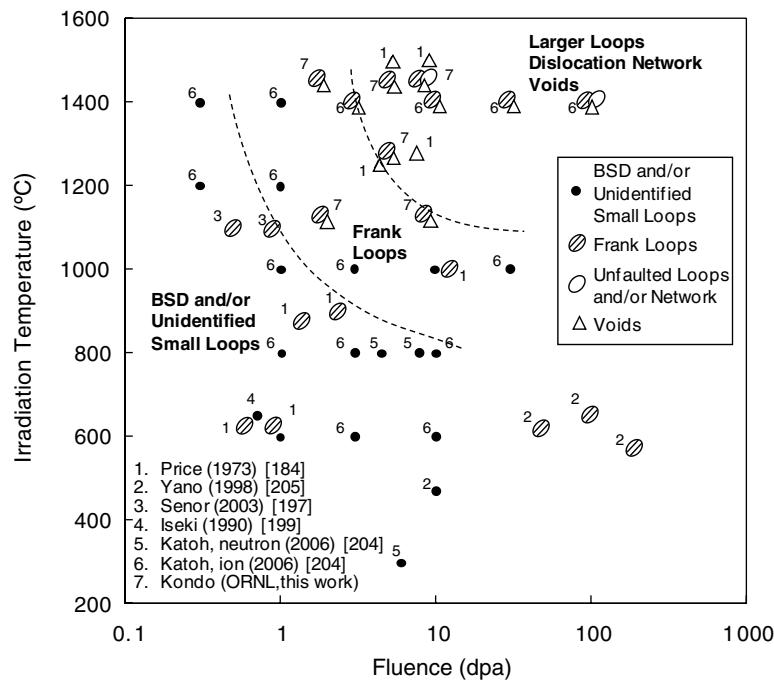


Fig. 17. Updated summary of the microstructural development in cubic SiC during neutron and self ion irradiation.

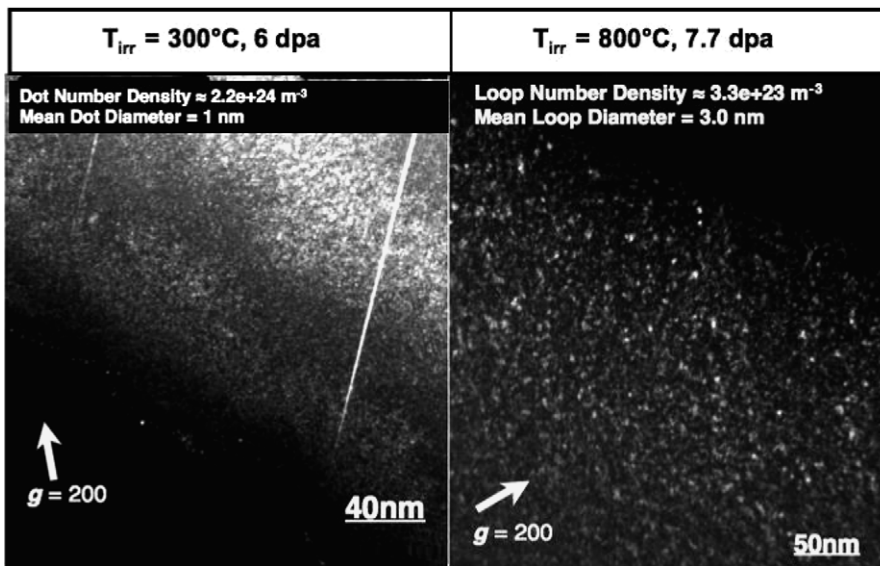


Fig. 18. Saturated microstructure for CVD Neutron Irradiated at 573 and 1073 K.

The approach to saturation swelling is shown for HFIR neutron irradiated Rohm and Haas CVD SiC in Fig. 19. In this figure the swelling is depicted in both logarithmic (Fig. 19(a)) and linear (Fig. 19(b)) plots. In addition to the approach to saturation, this figure highlights two other characteristics of neutron-induced swelling of SiC. First, the swelling of SiC is highly temperature dependent. For the data given in Fig. 19, the 1 dpa and saturation

values of swelling at 473 K are approximately five times that for 1073 K irradiation. This reduced swelling with increasing irradiation temperature is primarily attributed to enhanced recombination of cascade produced Frenkel defects due to lower interstitial clustering density for higher temperatures. The second characteristic swelling behavior to note is that the swelling saturates at a relatively low dose. For damage levels of a few dpa (typically

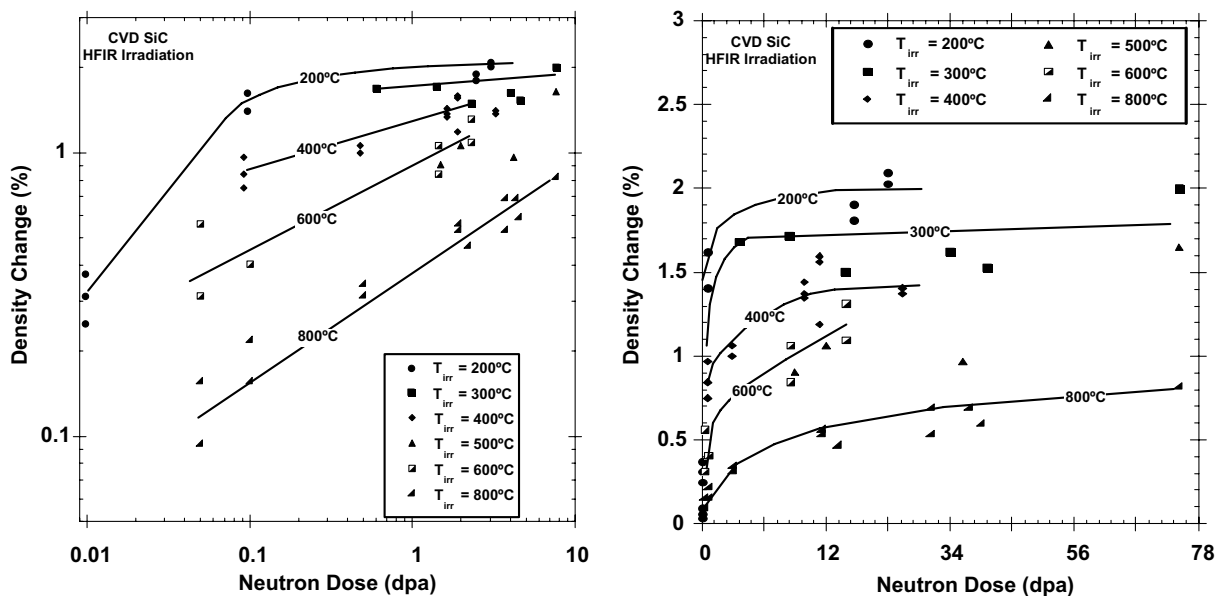


Fig. 19. Swelling and saturation of CVD SiC in the point-defect swelling regime.

months in a fission power core) the swelling in the point-defect recombination range has found its saturation value.

At higher temperatures such as 1173–1673 K [184,197,205], Frank faulted loops of interstitial type become the dominant defects observed by transmission electron microscopy. It has also been reported that Frank faulted loops appear for lower temperature neutron irradiation at extremely high doses [212]. Under silicon ion irradiation at 1673 K, the development of Frank loops into dislocation networks through unfauling reactions at high doses is reported [205]. The volume associated with dislocation loops in irradiated SiC has been estimated to be on the order of 0.1% [213,214]. At temperatures where vacancies are sufficiently mobile, vacancy clusters can be formed. Three-dimensional cavities (or voids) are the only vacancy clusters known to commonly develop in irradiated SiC. The lowest temperature at which void formation was previously reported under neutron irradiation is 1523 K [215]. Senor reported the lack of void production after neutron irradiation to 0.9 dpa at 1373 K, though voids were observed after subsequent annealing at 1773 K for 1 h [197]. Under silicon ion irradiation, voids start to form at 1273 K at very low density and become major

contributors to swelling at irradiation conditions of 1673 K at >10 dpa [213]. Positron annihilation and electron paramagnetic resonance studies have shown that the silicon vacancy in cubic SiC becomes mobile at 1073–1173 K [216,217]. Therefore, it would not be surprising for void swelling to take place at as low as ~1273 K at high doses, particularly for low damage rate irradiations.

As previously mentioned, data on swelling of SiC in the high-temperature ‘void swelling’ regime has been somewhat limited. However, recent work has been carried out in the ~1173–1773 K range for Rohm and Haas CVD SiC irradiated in HFIR. Of particular significance to that experiment is the confidence in irradiation temperature owing to the melt-wire passive thermometry [218]. Recent TEM imaging by Kondo [218] clearly shows the evolution of complex defects. As example, Fig. 20 indicates sparse void formation on stacking faults for material irradiated at 1403 K. Significant growth of voids commences at 1723 K. The well faceted voids appeared to be tetrahedrally bounded by {111} planes, which likely provides the lowest surface energy in cubic SiC. In many cases, voids appeared to be aligned on stacking faults at all temperatures. However, intragranular voids unattached to stacking faults were also commonly observed at

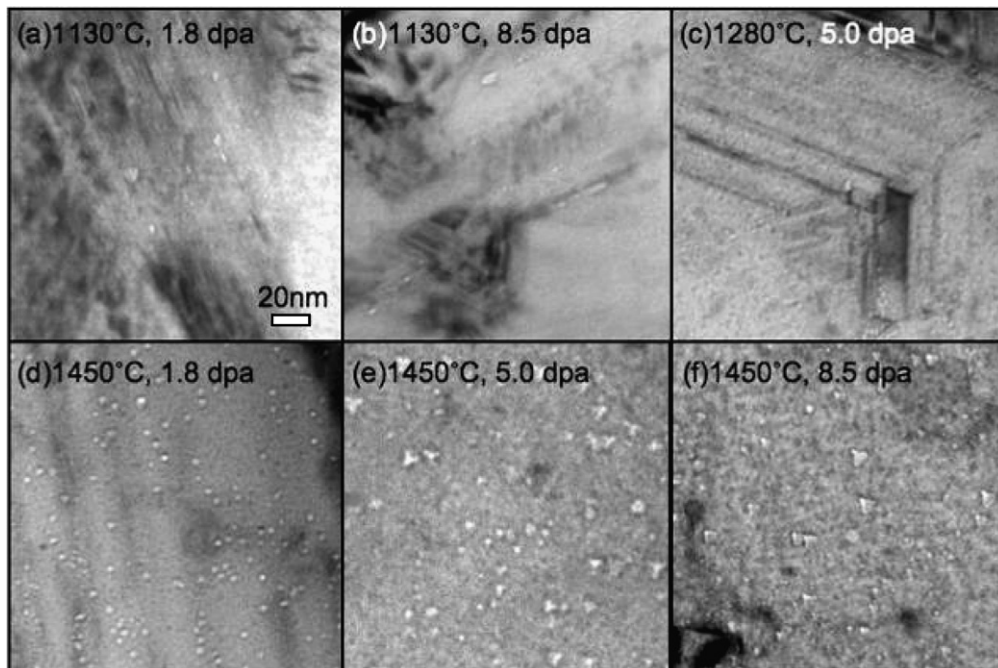


Fig. 20. Evolution of voids in high temperature irradiated CVD SiC.

1723 K. The evolution of dislocation microstructures at 1403–1723 K is shown in Fig. 21. In this temperature range, dislocation loops are identified to be of Frank faulted loops of interstitial type. Evolution of the dislocation loops into dislocation networks was confirmed for irradiation at 1723 K.

Fig. 22 plots both historical data and published and unpublished data from a recent high-temperature irradiation study [218]. This plot is limited to literature data on high-purity CVD SiC. A divergence from point-defect ‘saturated’ swelling to non-saturated swelling is observed in the 1073–1473 K range, though additional data in this temperature range as a function of fluence would be required to precisely define such behavior. Above 1273 K, there exists a clear non-saturated swelling behavior for CVD SiC. The three divergent curves drawn in Fig. 22 represent data taken at nominally  $\sim 1.75$ , 5.0, and  $8.5 \times 10^{25} \text{ n/m}^2$  ( $E > 0.1 \text{ MeV}$ ) (assumed 1.75, 5.0, and 8.5 dpa). In the 1373–1473 K temperature range, volumetric swelling is apparently at a minimum though increases from  $\sim 0.2\%$  to  $\sim 0.4\%$  to  $\sim 0.7\%$  for  $\sim 1.75$ , 5.0, and 8.5 dpa. Clearly the swelling in this temperature range has not saturated by 10 dpa. This finding is somewhat surprising given the apparent mobility of the silicon vacancy above 1273 K found experi-

mentally in cubic SiC (the CVD SiC of this study is highly faulted FCC) [216,217]. Above this minimum in swelling the data indicates a continual swelling increase to the highest irradiation temperature of  $\sim 1773$ – $1873 \text{ K}$ . At  $\sim 1773 \text{ K}$  measured swelling was  $\sim 0.4$ , 1.0, and 2.0% for  $\sim 1.75$ , 5.0, and 8.5 dpa. It was also noted in the study by Snead et al. [219] that for  $\sim 1773 \text{ K}$  surface reaction between SiC and the graphite holder had taken place. Though, a loss of silicon from the surface cannot be ruled out.

Fig. 22 includes historical data for swelling above 1273 K [182–184,197,208,215,220]. Specifically, Senor et al. [197] reports swelling for the same type of CVD SiC irradiated in this study, also irradiated in a water moderated fission reactor (the ATR). His maximum dose, irradiation temperature and swelling data were  $\sim 1 \text{ dpa}$ ,  $\sim 1373 \pm 30 \text{ K}$ , and  $0.36 \pm 0.02\%$ . The irradiation temperature quoted in Senor’s work was a best estimate though the author also provides an absolute bound for his experiment of 1073–1473 K. The maximum swelling in the Senor work ( $0.36 \pm 0.02\%$  at  $\sim 1 \text{ dpa}$ ) is somewhat higher than the  $\sim 0.25\%$  swelling at 2 dpa,  $\sim 1373 \text{ K}$  of the trend data in Fig. 22. This is seen from the rightmost figure of Fig. 22. Also seen in the figure is the high temperature swelling of Price

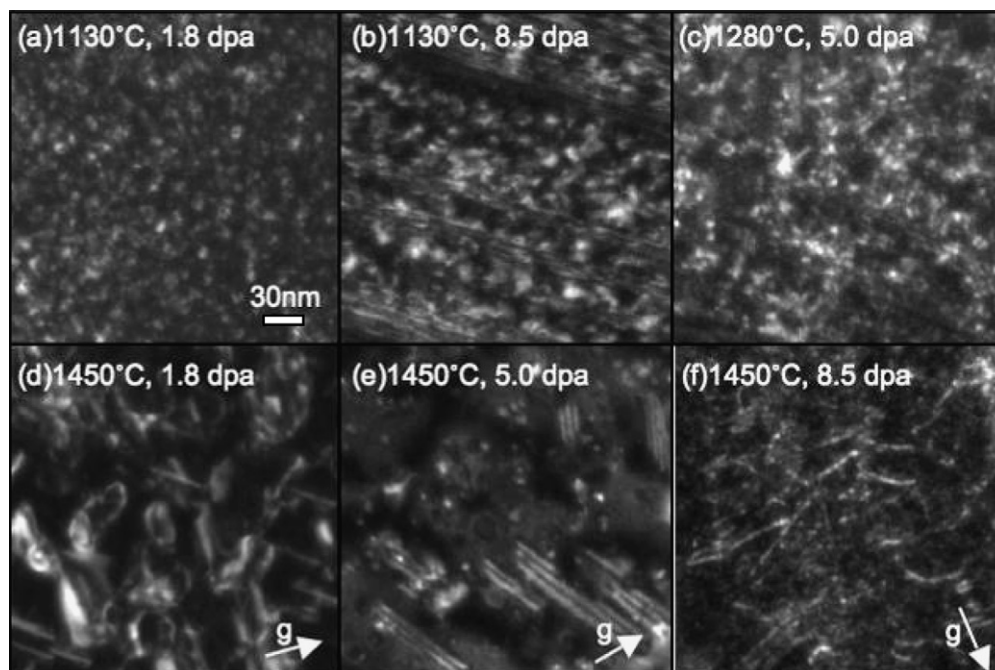


Fig. 21. Evolution in dislocation networks for high temperature irradiated CVD SiC.

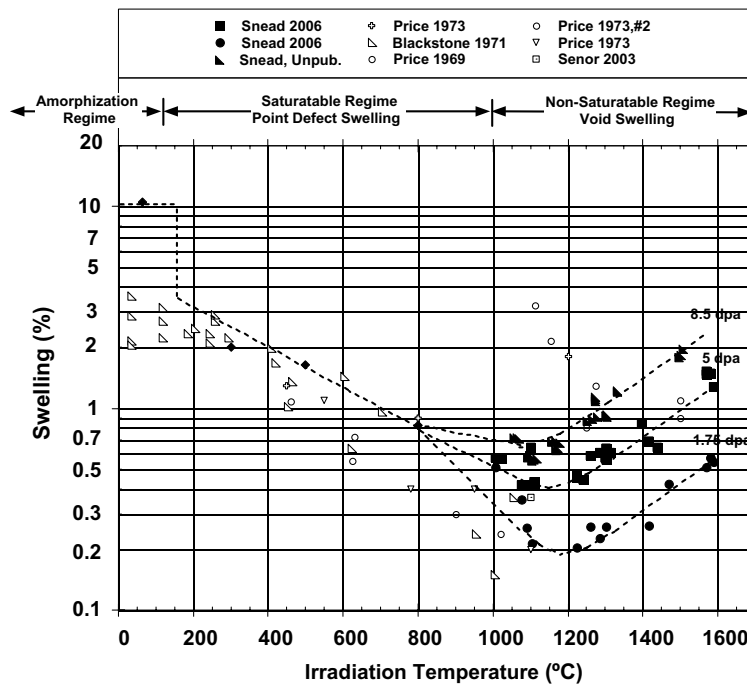


Fig. 22. Irradiation-induced swelling of SiC to high irradiation temperatures.

[183,184,215]. The Price data, which are in the dose range of about 4–8 dpa, are in fair agreement with the measured swelling of the Snead data of Fig. 22. The highest swelling material ( $\sim 1523$  K,  $\sim 6$  and 10 dpa) shows the largest discrepancy, though if the temperature error bands quoted by the various authors are taken into account the data are conceivable more in alignment. It is also noted that the Price material may have had some excess silicon leading to higher swelling as compared to stoichiometric material.

As mentioned earlier, the microstructural evolution of irradiated SiC is roughly understood, at least for temperatures up to  $\sim 1373$  K. The swelling near the critical amorphization temperature ( $\sim 423$  K) is classically described as the differential strain between the single interstitial, or tiny interstitial clusters, immobile vacancies, and antisite defects. As the temperature increases above the critical amorphization temperature the number of defects surviving the cascade are reduced and the mobility of both silicon and carbon interstitials becomes significant. For temperature exceeding  $\sim 1273$  K microstructural studies have noted the presence of both Frank loops and tiny voids indicating limited mobility of vacancies. The apparent increase in swelling with dose in the 1373–1873 K range seen

in Fig. 22, and the observed production of voids, are interesting considering the maximum irradiation temperature ( $\sim 1773$  K in Fig. 22) is  $\sim 0.65$  of the melting (dissociation) temperature ( $T_m$ ) for SiC. Here we have assumed the value of Olesinski and Abbaschian [13] of 2818 K where stoichiometric SiC transforms into C + liquid phase. This value of  $0.65 T_m$  is high when viewed in comparison to FCC metal systems where void swelling typically begins at  $\sim 0.35 T_m$ , goes through a maximum value, and decreases to nil swelling by  $\sim 0.55 T_m$ . (It is noted that the melting and dissociation temperature of SiC are somewhat variable in the literature. Even considering this variability the previous statement is still accurate). If, as the swelling data seems to indicate, the voids in SiC are continuing to grow in SiC irradiated to 1773 K the energies for diffusion of one or both the Si and C vacancy must be quite high, as are the binding energies for clustered vacancies. This has been shown through theoretical work in the literature [52,221–223]. However, it is noted that the defect energetics obtained from that body of work, and in particular those of the Si and C vacancy, SiC vary widely. Perhaps the work of Bockstedte et al. [222] following an ab initio approach, is the most accurate yielding a ground state migration energy for Si and C vacancies of



3.5 and 3.4 eV, respectively. It was also noted by Bockstedte et al. [222] that the charge state of the vacancy will affect the migration energy. Specifically the carbon vacancy in the +1 and +2 charge state increases from 3.5 to 4.1 and 5.2 eV, respectively and that of silicon in the −1 and −2 charge state decreases from 3.4 to 3.2 and 2.4 eV, respectively. Several papers discuss the vacancy and vacancy cluster mobility measured experimentally. The silicon mono-vacancy has been shown to be mobile below 1273 K. Using electron spin resonance, Itoh et al. [216] found the irradiation-produced T1 center in 3C-SiC disappearing above 1023 K. The T1 center was later confirmed to be Si vacancy [217]. Using electron spin resonance the carbon vacancy in 6H-SiC is shown to anneal above 1673 K [224]. Using isochronal annealing and positron lifetime analysis Lam et al. [223] has shown a carbon–silicon vacancy complex to dissociate above ~1773 K for the same 6H single crystal materials studied here.

From a practical nuclear application view the swelling data for CVD SiC can be broken down into the amorphization regime (<423 K), the saturatable point-defect swelling regime (423–1073 K) range and non-saturated void-swelling regime which occurs for irradiation temperature >1273 K. From the data of Fig. 22 it is still unclear where the actual transition into the non-saturated swelling begins. Furthermore, while there is an increase in swelling in the 1273–1773 K swelling as the dose is increased from ~1.75, 5.0, and  $8.5 \times 10^{25}$  n/m<sup>2</sup> ( $E > 0.1$  MeV), is close to linear with neutron dose, it is unclear how swelling will increase as a function of dose above 10 dpa. Extrapolation of swelling outside of the dose range of Fig. 22 is therefore problematic.

### 3.2. Thermal properties

#### 3.2.1. Heat content

According to Lee et al. [200], the effect of neutron irradiation on the specific heat of SiC was negligibly small. The specific heat of SiC is therefore assumed to be unchanged by neutron irradiation.

#### 3.2.2. Thermal conductivity

Due to a low density of valence band electrons, thermal conductivity of most ceramic materials, SiC in particular, is based on phonon transport. For a ceramic at the relatively high temperature associated with nuclear applications the conduction heat can be generally described by the strength of the individual contributors to phonon scattering:

grain boundary scattering ( $1/K_{gb}$ ), phonon–phonon interaction (or Umklapp scattering  $1/K_u$ ), and defect scattering ( $1/K_d$ ). Because scattering for each of these elements occurs at differing phonon frequencies and can be considered separable, the summed thermal resistance for a material can be simply described as the summation of the individual elements; i.e.,  $1/K = 1/K_{gb} + 1/K_u + 1/K_d$ . As seen in Fig. 7 the non-irradiated thermal conductivity of SiC is highly dependent on the nature of the material (grain size, impurities, etc.) and the temperature. While materials can be optimized for low intrinsic defect, impurity, and grain boundary scattering, the temperature dependent phonon scattering cannot be altered and tends to dominate at high temperature (above about 673 K for SiC).

The effect of irradiation on SiC in the temperature range of ~423–1073 K (the point defect regime discussed in Section 3.1) is to produce simple defects and defect-clusters that very effectively scatter phonons. For ceramics possessing high thermal conductivity the irradiation-induced defect scattering quickly dominates, with saturation thermal conductivity typically achieved by a few dpa. Moreover, as the irradiation-induced defect scattering exceeds the phonon–phonon scattering, the temperature dependence of thermal conductivity is much reduced or effectively eliminated.

The rapid decrease and saturation in thermal conductivity of CVD SiC upon irradiation in the point-defect regime has been reported by several authors [49,193,215,225,226]. Fig. 23 shows this rapid decrease in thermal conductivity for fully dense CVD SiC including new data, previous data from the authors [193,225], and that of Rohde [49]. It is noted that the data of Thorne is omitted as the material was of exceptionally low density for a CVD SiC material. Moreover, the data of Price [215] is published with a range of fluence so as not to be valuable in the figure.

In recent papers by Snead on the effects of neutron irradiation on the thermal conductivity of ceramics [225], and specifically on SiC [219], the degradation in thermal conductivity has been analyzed in terms of the added thermal resistance caused by the neutron irradiation. The thermal defect resistance is defined as the difference in the reciprocal of the irradiated and non-irradiated thermal conductivity ( $1/K_{rd} = 1/K_{irr} - 1/K_{non-irr}$ ). This term can be related directly to the defect type and concentration present in irradiated ceramics [225]. Moreover, this term can be used as a tool to

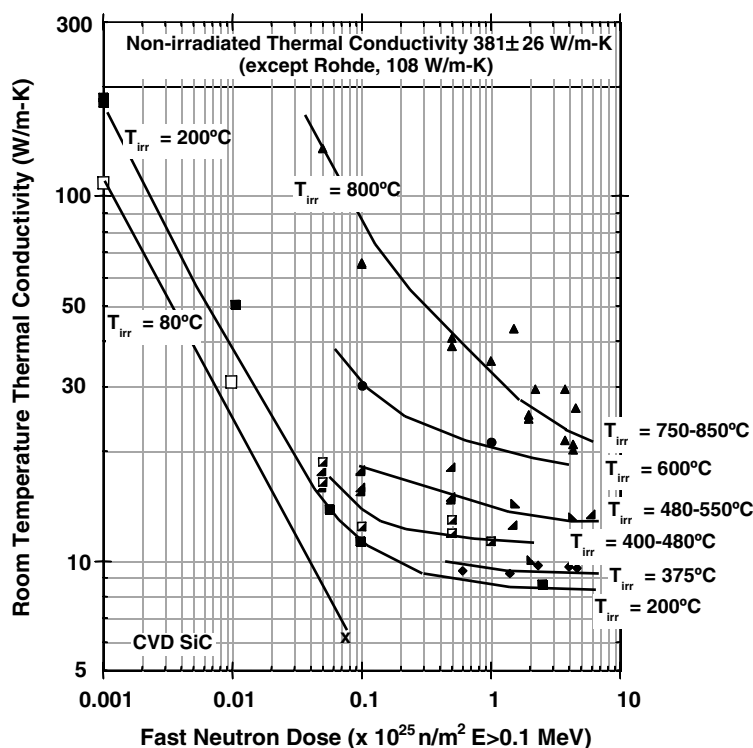


Fig. 23. Degradation in room-temperature thermal conductivity for CVD SiC (Rohde data designated as x).

compare the thermal conductivity degradation under irradiation of various ceramics, or for example various forms of SiC. It has been shown that, for certain high purity forms of alumina, the accumulation of thermal defect resistance is very similar even though the starting thermal conductivity of the materials is substantially different. Similarly, CVD SiC was shown to have a similar accumulation of thermal defect resistance as a hot-pressed form of SiC with substantially lower ( $\sim 90$  W/m K) non-irradiated thermal conductivity. The utility of this finding is that if the thermal defect resistance is mapped as a function of irradiation temperature and dose for a form of high purity CVD SiC it can be applied to determine the thermal conductivity to any high-purity CVD SiC, independent of starting thermal conductivity. The accumulation in thermal defect resistance generated from the data of Fig. 23 is shown in Fig. 24.

Another result of the previously reported analysis on irradiated CVD SiC [219] is that the thermal defect resistance appears to be directly proportional to the irradiation-induced swelling, though the data-set for making the previous assertion was somewhat limited. A compilation plot including the previous

data-set as well as the new data of Fig. 24 is shown in Fig. 25. It is clear from this plot that the linear relationship between swelling and thermal defect resistance exists. Moreover, there does not appear to be any effect of irradiation temperature on this result. The fact that the thermal defect resistance is proportional to the irradiation induced swelling allows a rough estimate of thermal conductivity. As measurement of thermal conductivity for the SiC TRISO shell is not practical, while measurement of density is routine, this finding allows an indirect determination of thermal conductivity by measurement of the density change in the TRISO SiC shell by means of a density gradient column or other technique.

The thermal conductivity degradation discussed to this point has been for the point defect regime discussed in Section 3.1. For irradiation above this temperature (the non-saturable void swelling regime), the thermal properties are not expected to saturate (at least at low dpa). The primary reason for this is that the formation of voids and other complex defects in the high temperature regime (which contribute to the non-saturated swelling as seen in Fig. 22) contribute to phonon scattering,

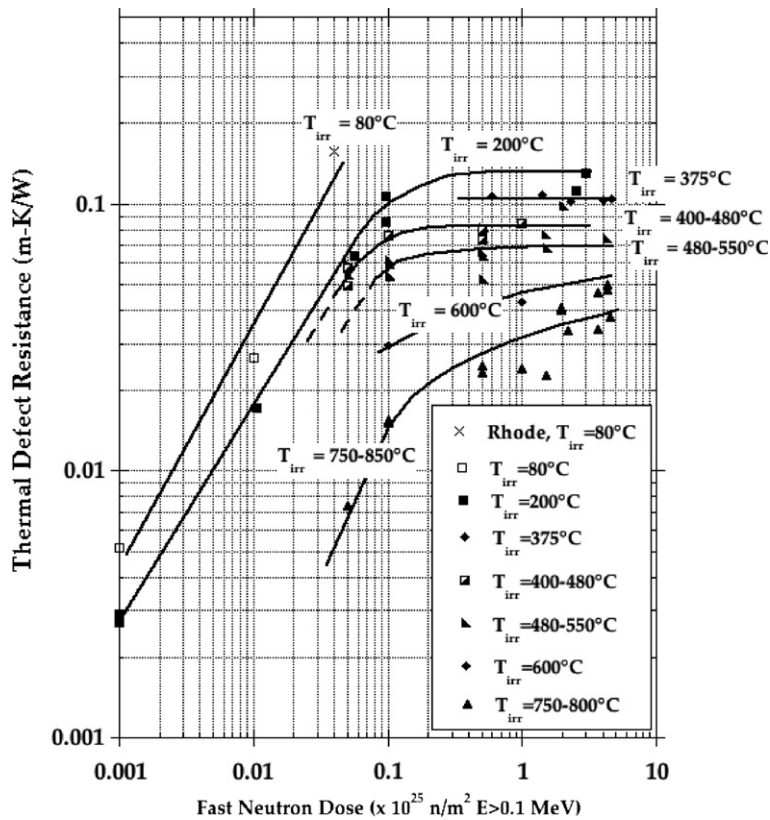


Fig. 24. Thermal defect resistance for stoichiometric CVD SiC as a function of neutron dose (Rhode data designated as  $\times$ ).

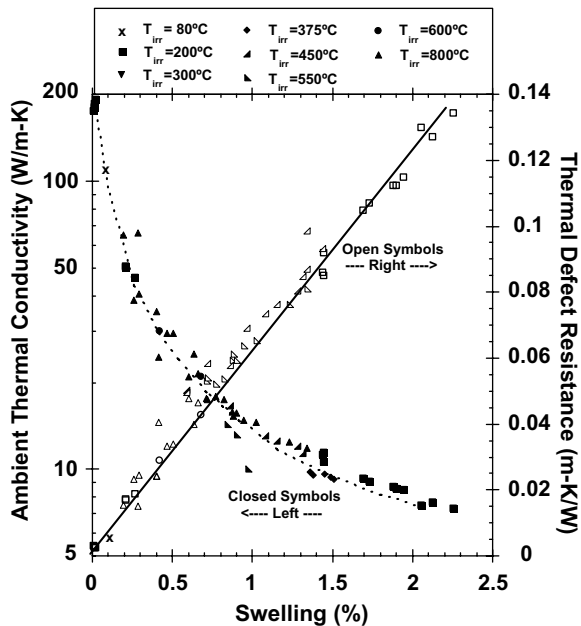


Fig. 25. The room-temperature thermal conductivity and thermal defect resistance as a function of irradiation-induced density change.

and these defects will not saturate. Moreover, it has been shown that the linear relationship that existed between swelling and thermal defect resistance (as seen in Fig. 25) does not exist in this elevated temperature regime [219]. This underlines the fact that the phonon scattering and swelling are no longer controlled by the same defects in the lower temperature saturatable and elevated, non-saturatable, temperature regimes. A compilation plot of room-temperature thermal conductivity as a function of irradiation temperature for the saturatable and non-saturatable temperature regimes is given in Fig. 26.

By comparison to the non-irradiated room-temperature conductivity value of  $\sim 280$  W/m K it is clear that the thermal conductivity degradation in the highest temperature regimes is less dramatic, even though the swelling is rapidly increasing (see Fig. 22). This is opposite to the behavior in the lower temperature, saturatable regime, where high swelling corresponds to extreme reduction in thermal conductivity. Unfortunately, the data on

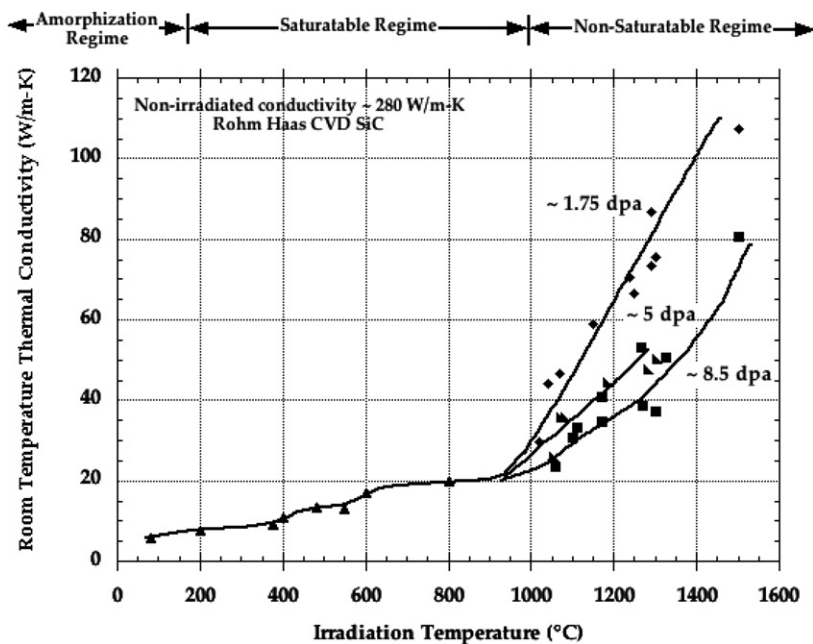


Fig. 26. Room-temperature thermal conductivity in the saturable and non-saturable regime.

thermal conductivity reduction in the non-saturable regime is limited, and given the lack of knowledge of the specific defects governing the phonon scattering, it is not possible to predict behavior outside of the data-set of Fig. 26.

Data presented thus far has been limited to measurement of thermal conductivity at room-temperature. As described in Fig. 7, there is a dramatic dependence of thermal conductivity on measurement temperature. To first order the temperature dependence of irradiated materials can be found by applying the temperature dependence of non-irradiated SiC. This approximation (dashed lines) is compared to actual data (solid lines) in Fig. 27 and shows fair correspondence. However, it is clear that such a treatment systematically underestimated the thermal conductivity degradation. This implies temperature dependence to the defect scattering that is not presently understood.

### 3.2.3. Thermal expansivity

The only one report on the effect of neutron irradiation on thermal expansivity was found in Ref. [4]. The porous reaction-bonded SiC material was irradiated at 523, 748 and 973 K up to the neutron fluence of  $1.8\text{--}5.0 \times 10^{25} \text{ n/m}^2$ . The results indicated no significant change in thermal expansivity anticipated by neutron irradiation. No data is currently available for other SiC forms.

### 3.3. Electrical properties

Reactor irradiation has a pronounced effect on the transient, and permanent, conductivity of SiC. Below irradiation temperature, the post-irradiation electrical resistivity (at ambient temperature) of neutron irradiated SiC remains unchanged by annealing, while, above the irradiation temperature, it increases exponentially with increased annealing temperature [227,228]. This transition temperature is often used as the basis for determining irradiation temperatures. The annealing behavior of the electrical resistivity of SiC is very complicated due to the combined effects of concentration, mobility, and trapping of both majority and minority charge carriers. Snead et al. [193,228] discuss the two permanent neutron irradiation effects on resistivity: the effects of (1) nuclear transmutation and (2) increasing dangling bond density by radiation-induced defects. Nuclear transmutation may affect the electrical resistivity, increasing the donor concentration through the  $^{30}\text{Si}(n, \gamma) ^{31}\text{Si}$ , and subsequent beta decay to (n-type donor)  $^{31}\text{P}$ . Additionally, 20% of the 290 wppm intrinsic (p-type acceptor) boron is removed due to the  $^{10}\text{B}(n, \alpha) ^7\text{Li}$  reaction. Similarly, other impurities such as nitrogen, aluminum, etc. would affect the electrical resistivity. It is also noted that there is a transient radiation-induced enhancement in electrical conductivity of SiC (as

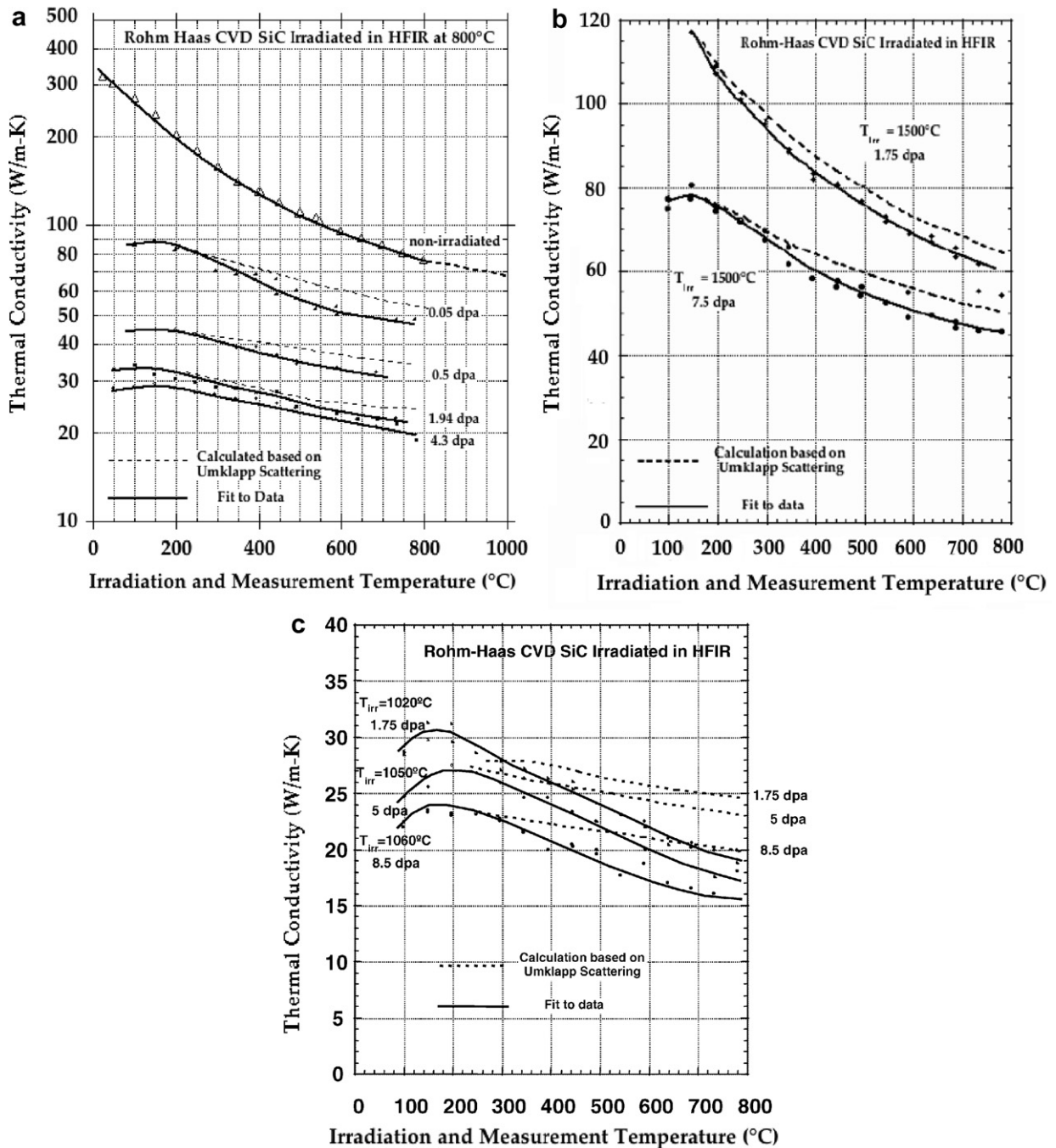


Fig. 27. Effect of temperature on the conductivity of irradiated SiC. (a)  $T_{irr} = 800^\circ\text{C}$ , (b)  $T_{irr} = 1500^\circ\text{C}$  and (c)  $T_{irr} = 1020$ – $1060^\circ\text{C}$ .

with all insulating materials) due to ionizing irradiation [193], exists. This increased conductivity is simply due to ionization of electrons into the conduction band and is therefore a function of the ionizing dose rate. This phenomenon is transient, only occurring while ionizing irradiation is present.

### 3.4. Mechanical properties

#### 3.4.1. Elastic constants

Fig. 28 summarizes the irradiation temperature dependence of the elastic modulus change. Irradiation generally reduces modulus with greater



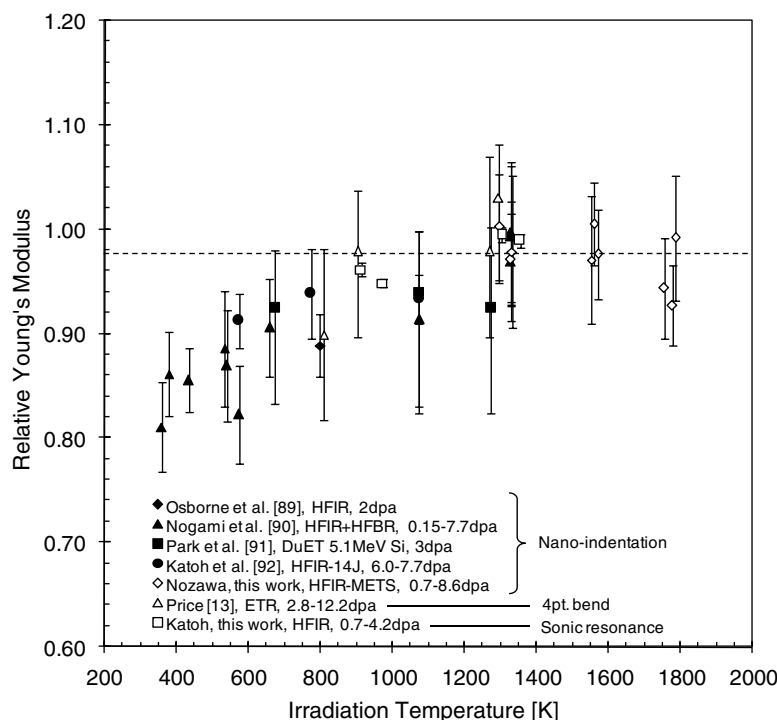


Fig. 28. Irradiation temperature dependence of irradiated elastic modulus of CVD SiC, at ambient temperature, normalized to unirradiated values. The error bars are showing standard deviations for all the neutron data points and ranges of data scatter for the ion data points.

reduction for lower temperature irradiation. The modulus reduction becomes negligible when irradiation temperature reaches or exceeds  $\sim 1273$  K. There seems to be an indistinct stage between 1073 and 1273 K. As expected, the elastic modulus trends with ‘point defect swelling’ of SiC. Point defect swelling is an isotropic volume expansion that is believed to occur by lattice relaxation due to accumulated isolated point defects and small point defect clusters during irradiation at temperatures where vacancies are not readily mobile. In SiC irradiated in the point defect swelling regime (150–1000 °C), a fairly good agreement of dimensional expansion and lattice spacing has been confirmed by X-ray diffractometry studies. In contrast, the data in the non-saturatable swelling regime is somewhat limited, though the data suggests that there is little reduction in elastic modulus even though the swelling is relatively large. However, in this regime the defects responsible for swelling are voids and other relatively large defects which would have less of an effect on elastic modulus as compared to point-defects.

An estimation of the influence of lattice relaxation on elastic modulus was attempted using the Tersoff potential [229]. The result predicted a linear

lattice swelling of 1% causing approximately 10% reduction in elastic modulus (Fig. 29). The predicted elastic modulus change could be varied by more than 10% depending on a selection of interatomic potential, with the Tersoff potential giving a relatively high sensitivity of modulus to the interatomic distance among various empirical interatomic potential functions. Therefore, the measured elastic modulus changes observed in this experiment are generally greater than the theoretical prediction. It is noted that the methods applied for generating the data of Fig. 29 are various and of differing quality. Typically, elastic modulus as measured by nano-indentation, while sometimes the only alternative for miniature specimens, which tends to give widely scattered and less reliable data than the mechanical or sonic modulus methods. Nonetheless, it is clear that the lattice expansion is a major cause of the irradiation-induced elastic modulus reduction in SiC.

### 3.4.2. Hardness

The irradiation effect on nano-indentation hardness of Roam and Haas CVD SiC in a fluence range of 0.1–18.7 dpa is summarized in Fig. 30. It is inter-



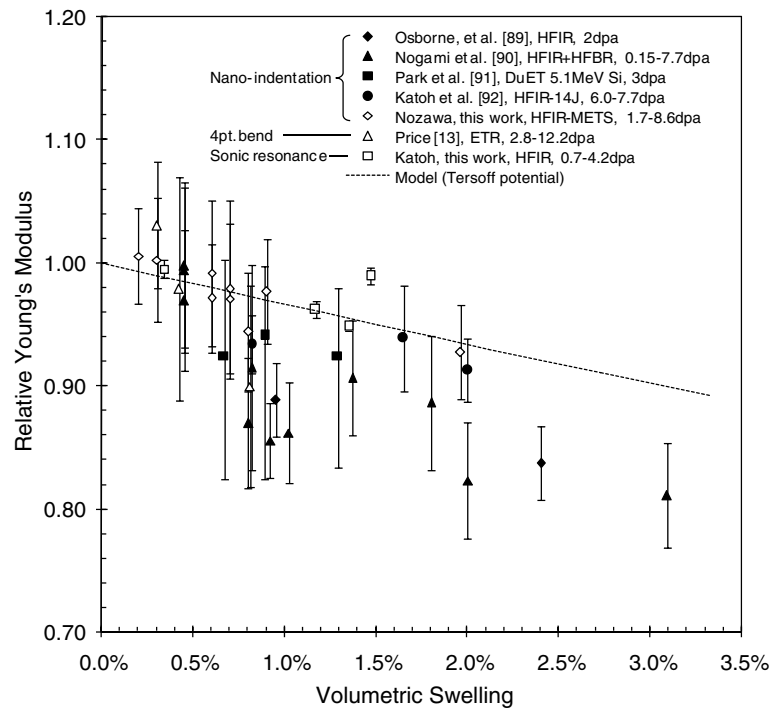


Fig. 29. Irradiation-induced change of elastic modulus vs. swelling of CVD SiC. An estimation of the influence of lattice relaxation on elastic modulus is calculated using Tersoff potential.

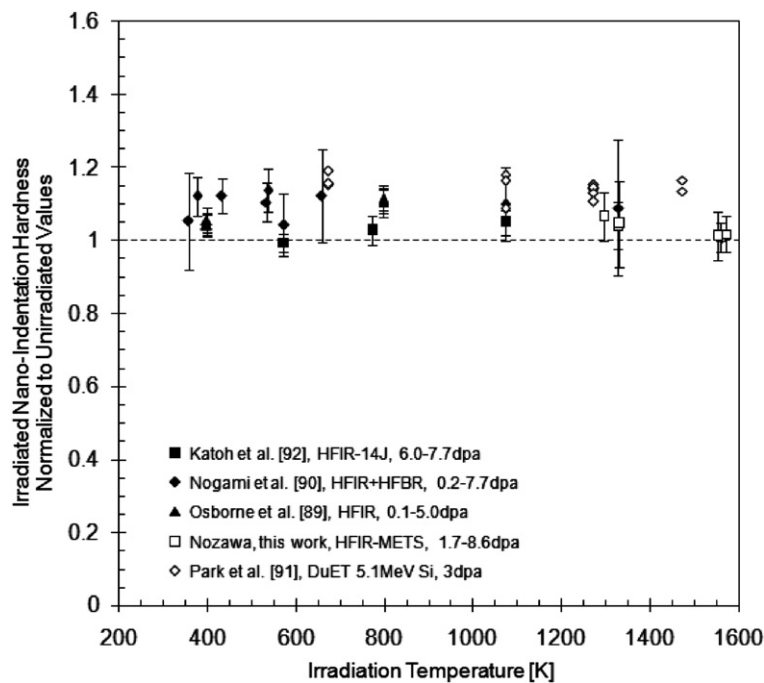


Fig. 30. Nano-indentation hardness of CVD SiC at ambient temperature as a function of irradiation temperature.

esting to note that the nano-indentation hardness exhibits relatively small scatter for the individual

experiments and the trend in data as a function of temperature is uniform. This observation is in

contrast to both the flexural strength and the indentation fracture toughness data that indicate a broad peak at an intermediate temperature. It is worth noting that nano-indentation hardness of brittle ceramics is, in general, determined primarily by the dynamic crack extension resistance in the near surface bulk material, and therefore should be more relevant to fracture toughness than to plastic deformation resistance. However, the nano-indentation hardness is less affected by surface effects of the original sample as the samples are generally polished prior to testing.

### 3.4.3. Fracture toughness

The effect of irradiation on the fracture toughness of Rohm and Haas CVD SiC is summarized in Fig. 31. This compilation plots data using the Chevron notched beam technique, though the bulk of the data-sets are reporting Vicker's or nano-indentation generated data [90–92]. The general trend is that the irradiation-induced toughening seems to be significant at 573–1273 K for the indentation fracture toughness data in spite of the decrease in elastic modulus, which confirms the increase in fracture energy by irradiation. The scatter for the indentation fracture toughness data among different experiments is likely caused both

by condition of the sample surface and the lack of standardized experimental procedures. Typically, indentation should be applied on polished surfaces, but conditions of polishing are not always provided in literature. Moreover, the crack length measurements are done using either optical microscopy, conventional scanning electron microscopy (SEM) or field emission SEM, all of which may give very different crack visibility. In addition, a few different models have been used for derivation of the fracture toughness. In conclusion, indentation fracture toughness techniques can be used only for qualitative comparison within a consistent set of experiments. It is noted that the irradiation-induced toughening is also shown by the Chevron notched beam technique, although data scatter is greater. These results confirm in the intermediate irradiation temperature range the increase of the fracture toughness of SiC.

### 3.4.4. Strength and statistical variation in strength

There have been several studies on the effect of neutron irradiation on the strength of various types of SiC forms including reaction bonded, sintered, pressureless sintered, and CVD SiC materials [4,93,190,192,199,202,203,230–233]. The strength of SiC depends significantly on stoichiometry under

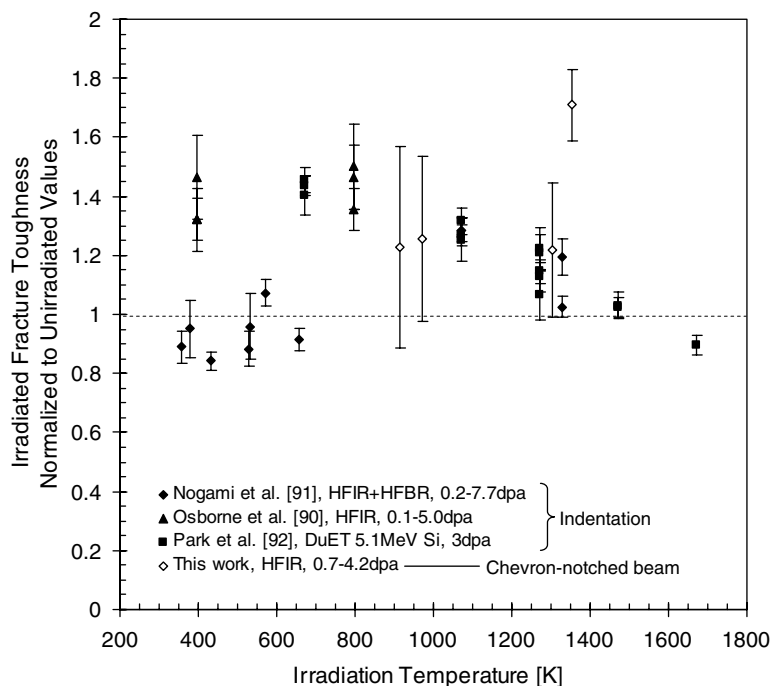


Fig. 31. Indentation fracture toughness of CVD SiC at ambient temperature as a function of irradiation temperature.

neutron irradiation. Both the sintered SiC and the reaction bonded SiC forms exhibit significant deterioration in strength by neutron irradiation (Fig. 32) [202]. The presence of impurities such as sintering additives for sintered SiC and excess Si for reaction bonded SiC, which typically segregate to grain boundaries, have a significant influence on strength under neutron irradiation. For the case of sintered SiC with boron compounds as sintering additives, the reaction of  $^{10}\text{B}(n, \alpha) ^7\text{Li}$  causes the accumulation of helium bubbles near the grain boundaries under neutron irradiation [190,230–232]. In contrast, anisotropic swelling between Si and SiC for reaction bonded SiC causes disruption at the grain boundary, severely reducing the strength [190,192,199,230–233]. Meanwhile, the highest purity materials such as CVD SiC exhibit superior irradiation resistance.

The irradiation effect on flexural strength of Roam and Haas CVD SiC in a fluence range of 0.15–18.7 dpa is summarized in Fig. 33. As with the fracture toughness data, irradiation-induced strengthening seems to be significant at 573–1273 K. The large scatter in flexural strength of brittle ceramics is inevitable since the fracture strength is determined by the effective fracture toughness, morphology and characteristics of the flaw that caused the fracture. Irradiation possibly modifies both the flaw characteristics and the fracture toughness through potential surface modification, relaxation of the machining-induced local stress,

modifications of elastic properties and fracture energy.

A change in the Weibull statistics, indicating a higher scatter in as-irradiated flexural strength has been observed by previous authors, though the point could not be made convincingly due to limitations in the number of tests observed. In the earliest work known to the authors, Sheldon [234] noted a 14% decrease in crushing strength of highly irradiated CVD SiC shells with an increase of the coefficient of variation from 8% to 14%. Price [232] used a four-point bend test on relatively thin ( $\sim 0.6$  mm) strips of CVD SiC deposited onto a graphite substrate. In his work the flexural strength following an  $\sim 9.4 \times 10^{25}$  n/m<sup>2</sup> ( $E > 0.1$  MeV) irradiation was unchanged within the statistical scatter, but the scatter itself increased from about 10% to 30% of the mean flexural strength as described assuming a normal distribution. Unfortunately, there were not sufficient samples in Price's work to infer Weibull parameters. In more recent work by Dienst [198] the Weibull modulus was reported to decrease from about 10 to less than 5 for irradiation of  $\sim 1 \times 10^{26}$  n/m<sup>2</sup> ( $E > 0.1$  MeV). However, it is worth noting that the Dienst work used a rather limited sample size (about 10 bars.)

Statistically meaningful data-sets on the effect of flexural strength of CVD SiC are reported in this proceedings by Newsome [203] and Katoh [93]. Fig. 34 shows a compilation Weibull plot of flexural strength of non-irradiated and irradiated Rohm and

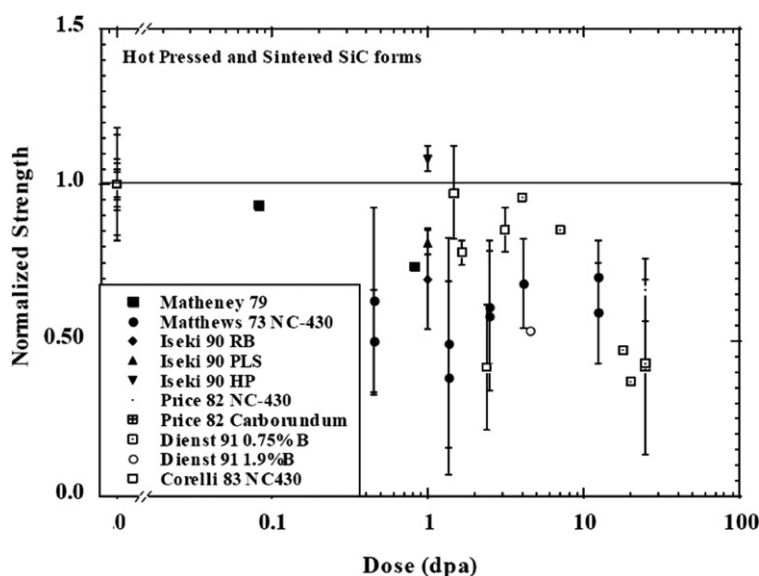


Fig. 32. Fluence dependence of irradiated flexural strength of hot-pressed and sintered SiC normalized to unirradiated strength [190].

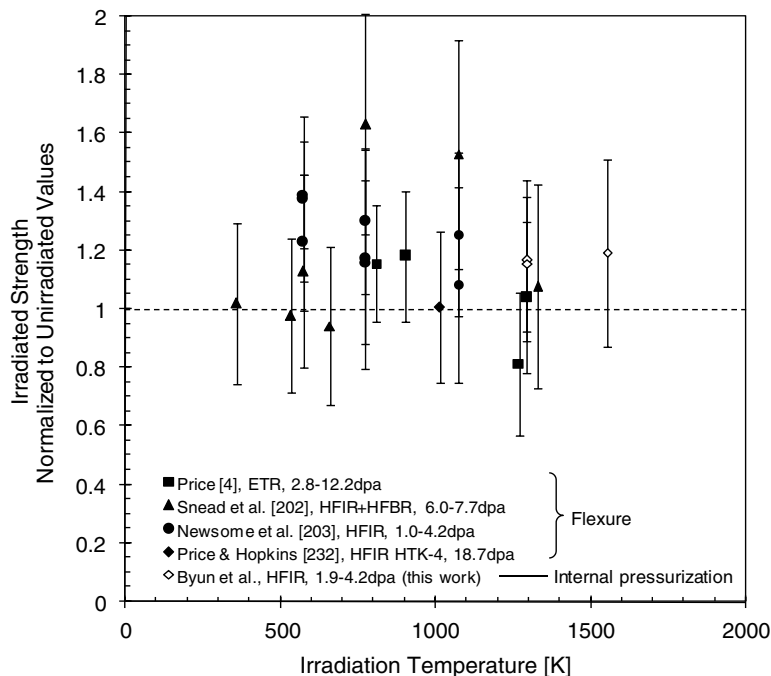


Fig. 33. Flexural strength of CVD SiC at ambient temperature as a function of irradiation temperature.

Haas CVD SiC taken from the two separate irradiation experiments carried out by Newsome [203] and Katoh [93] and they are summarized in Table 8. The sample population was in excess of 30 for each case. In Fig. 34(a) the data was arranged by irradiation temperature including data for non-irradiated and  $1.5\text{--}4.6 \times 10^{26} \text{ n/m}^2$  ( $E > 0.1 \text{ MeV}$ ) dose range. It is clear that Weibull modulus decreased by irradiation and appears dependent on irradiation temperature. This is not easily visualized through inspection of Fig. 34(a) unless one notes that there are significantly more low stress fractures populating the 573 K population. The scale parameters of flexural strength of non-irradiated materials and materials irradiated at 573, 773, and 1073 K were 450, 618, 578 and 592 MPa, respectively. The Weibull modulus of flexural strength of non-irradiated materials and materials irradiated at 573, 773 and 1073 K were 9.6, 6.2, 5.5 and 8.7, respectively.

The work of Katoh, on identical material and irradiated at the same temperature as the Newsome work, is at a slightly higher irradiation dose. As seen in Fig. 34(b) the effect on the Weibull modulus undergoes a similar trend to that of Newsome, though the modulus for the 773 K irradiation of Katoh is not in agreement, actually showing a slight increase. However, this increase is likely due to a

statistical anomaly. Given the data discussed on the effect of irradiation on the Weibull modulus and scale parameter of CVD SiC bend bars it is clear that the material is somewhat (perhaps negligibly) strengthened and that the Weibull modulus decreases by up to a factor of two, with the greatest decrease occurring for the lowest temperature irradiation.

The fracture strength and failure statistics of tubular SiC ‘TRISO surrogates’ has been determined by the internal pressurization test and the results are plotted in Fig. 35. Thin-walled tubular SiC specimens of 1.22 mm outer diameter, 0.1 mm wall thickness, and 5.8 mm length were produced by the fluidized bed technique alongside TRISO fuels [141,146]. The specimens were irradiated in the High Flux Isotope Reactor (HFIR) to  $1.9$  and  $4.2 \times 10^{25} \text{ n/m}^2$  ( $E > 0.1 \text{ MeV}$ ) at 1293 and 1553 K. In the internal pressurization test, tensile hoop stress was induced in the wall of tubular specimens by compressively loading a polyurethane insert [146,148].

In Fig. 35, Weibull plots of the flexural strength and internal pressurization fracture strength of non-irradiated and irradiated samples are presented. As with the Newsome and Katoh data, the sample population is large enough to be considered statisti-

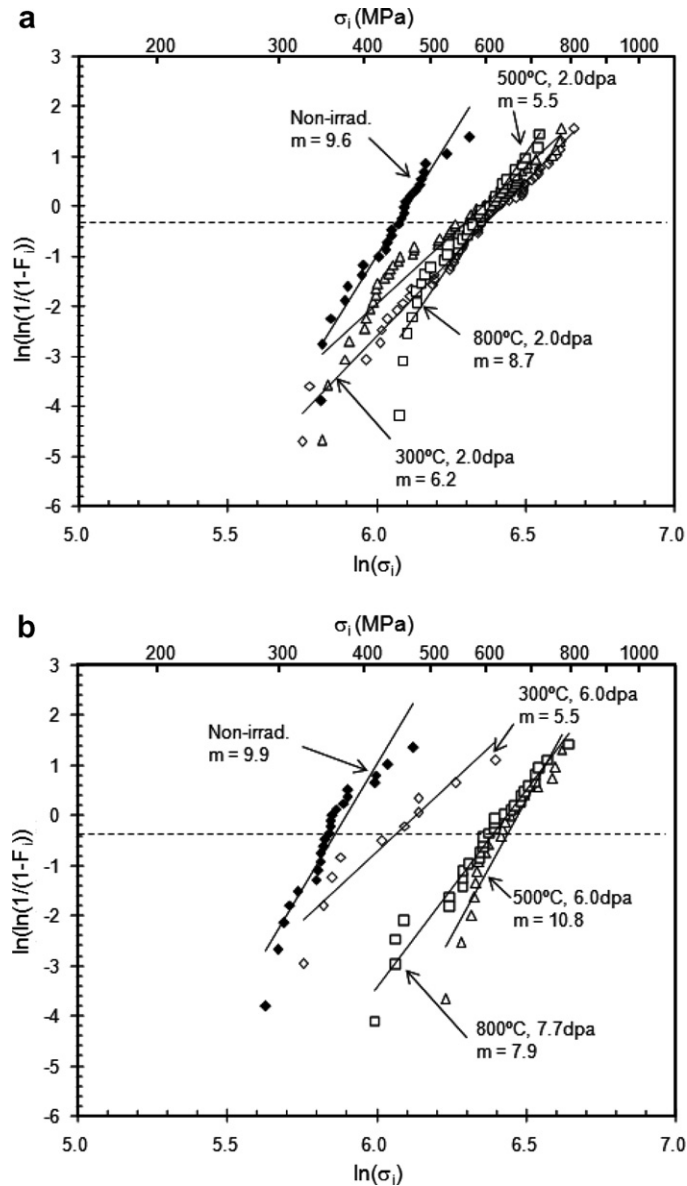


Fig. 34. Weibull plots of flexural strength of non-irradiated and irradiated CVD SiC in the dose range of (a)  $1.5\text{--}4.6 \times 10^{25} \text{ n/m}^2$  ( $E > 0.1 \text{ MeV}$ ) from Newsome [203] and (b)  $7.7 \times 10^{25} \text{ n/cm}^2$  ( $E > 0.1 \text{ MeV}$ ) from Katoh [93].

cally meaningful. From this data, the mean fracture stress of tubular specimens is seen to increase to 337 MPa (from 297 MPa) and the Weibull modulus slightly decreased to 3.9 (from 6.9) after irradiation to  $1.9 \times 10^{25} \text{ n/m}^2$  ( $E > 0.1 \text{ MeV}$ ) dpa at 1293 K. The mean fracture stresses and Weibull moduli at  $4.2 \times 10^{25} \text{ n/m}^2$  ( $E > 0.1 \text{ MeV}$ ) were similar to those at 1.9 dpa. The results for 4.2 dpa irradiation indicate that by increasing the irradiation temperature from 1293 to 1553 K no apparent discernable change in fracture stress distribution occurred. The

horizontal shift indicates a simple toughening or an increase in fracture toughness alone. While the data for these surrogate TRISO samples, irradiated through internal compression, are somewhat limited, the findings indicate that the trend in strength and statistics of failure are consistent with those found for bend bars. Therefore the general findings of the bend bar irradiation on strength and Weibull modulus appear appropriate for application to TRISO fuel modeling. Specifically, a slight increase in the mean strength is expected (though perhaps

Table 8

Summary of Weibull statistical strength of CVD-SiC

	Neutron dose (dpa)	Irradiation temperature (K)	Weibull modulus	Weibull mean strength (MPa)	Weibull characteristic strength (MPa)	Number of tests
Flexure Newsome [203]	Non-irradiated		9.6	433	450	25
	1.5–4.6	573	6.2	582	618	56
	1.5–4.6	773	5.5	541	578	55
	1.5–4.6	1073	8.7	567	592	34
Flexure Katoh [93]	Non-irradiated		9.9	353	366	23
	6.0	573	5.5	433	463	10
	6.0	773	10.8	626	648	20
	7.7	1073	7.9	598	627	31
Internal Pressurization Byun [this work]	Non-irradiated		7.6	301	316	32
	1.9	1293	4.4	340	369	17
	4.2	1293	5.4	341	365	22
	4.2	1553	3.8	342	377	24

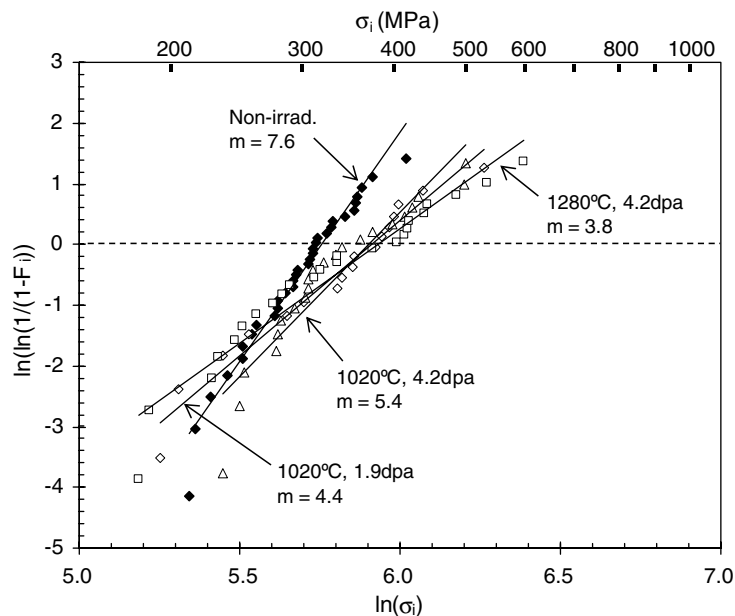


Fig. 35. Weibull statistical fracture strength of CVD SiC measured by the internal pressurization test.

negligible) and that the statistical spread of the fracture data as described by the Weibull modulus will broaden. Unfortunately a precise description of how the Weibull modulus trends with irradiation dose and temperature is not yet possible, though within the dose range and temperature covered by the data of Figs. 34 and 35 a reduction from a non-irradiated value of 10 to an irradiated value of 5 appears reasonable.

### 3.5. Irradiation creep

The definition of irradiation creep is the difference in dimensional changes between a stressed and an unstressed sample irradiated under identical conditions. Irradiation creep is important for structural materials for nuclear services since it is a major contributor to the dimensional instability of irradiated materials at temperatures where thermal creep



is negligible. However, studies on irradiation creep of SiC-based materials have so far been very limited, though it is of high importance for the behavior of the SiC TRISO shell.

Price published the result of an irradiation creep study on CVD SiC in 1977 [4]. In that work, elastically bent strip samples of CVD SiC were irradiated in a fission reactor, and the steady-state creep compliance was estimated to be in the order of  $10^{-38}$  [Pa dpa/m<sup>2</sup> ( $E > 0.18$  MeV)]<sup>-1</sup> at 1053–1403 K. Scholz and co-workers measured the transient creep deformation of SCS-6 CVD SiC-based fiber which was torsionally loaded under penetrating proton or deuteron beam irradiation [235–238]. They reported several important observations including the linear stress and flux dependency of the tangential primary creep rate at 873 K, and the negative temperature dependence of primary creep strain at the same dose. Recently, Katoh et al. determined the bend stress relaxation (BSR) creep in Rohm and Haas CVD SiC and Hoya monocrystalline 3C-SiC during irradiation in HFIR and JMTR at 673–1353 K [239]. Results reported for CVD SiC are summarized in Table 9.

In the BSR irradiation creep experiment by Katoh et al., creep strain for CVD SiC exhibited weak temperature dependence at  $<0.7$  dpa in the  $\sim 673$  to  $\sim 1303$  K temperature range, whereas a major transition at higher doses likely exists between  $\sim 1223$  and  $\sim 1353$  K. Below  $\sim 1223$  K, the creep strain appeared highly non-linear with neutron fluence due to the early domination of the transient irradiation creep. The transient creep was

speculated to have been caused by the rapid development of defect clusters and the structural relaxation of as-grown defects during early stages of irradiation damage accumulation. At  $\sim 1353$  K, irradiation creep mechanisms which are common to metals are likely operating.

In metals, steady-state irradiation creep rates are generally proportional to the applied stress and neutron (or other projectiles) flux,  $\phi$  [240,241], and therefore irradiation creep compliance,  $B$ , has been conveniently introduced [240]

$$\dot{\epsilon}_{ic} = \sigma(B\phi + D\dot{S}), \quad (25)$$

where  $S$  is void swelling and  $D$  is a coefficient of swelling-creep coupling. Ignoring the swelling-creep coupling term, preliminary estimations of the steady-state irradiation creep compliance of CVD SiC were given to be  $2.7 \pm 2.6 \times 10^{-7}$  and  $1.5 \pm 0.8 \times 10^{-6}$  (MPa-dpa)<sup>-1</sup> at  $\sim 873$  to  $\sim 1223$  K and  $\sim 1353$  K, respectively.

If linear-averaged, creep compliances of  $1-2 \times 10^{-6}$  (MPa-dpa)<sup>-1</sup> were obtained for doses of 0.6–0.7 dpa at all temperatures. Monocrystalline 3C-SiC samples exhibited significantly smaller transient creep strain by 0.7 dpa and greater subsequent deformation when loaded along  $\langle 011 \rangle$  direction.

To better define the irradiation creep behavior of SiC and the underlying physical mechanisms, it will be essential to further examine the stress dependence, dose dependence, effect of crystallographic orientation, microstructures of the crept samples, and the coupling between irradiation creep and swelling.

Table 9  
Irradiation creep data for CVD SiC from bend stress relaxation experiments

$T_{irr}$ (°C)	Fluence (dpa)	Reactor	Initial/final bend stress (MPa)	Initial/final bend strain ( $\times 10^{-4}$ )	Creep strain ( $\times 10^{-4}$ )	BSR ratio $m$	Average creep compliance $\times 10^{-6}$ (MPa-dpa) <sup>-1</sup>
CVD SiC							
400	0.6	JMTR	82/60	1.80/1.39	0.41	0.77	0.97
600	0.2	JMTR	81/57	1.80/1.31	0.49	0.73	3.5
600	0.6	JMTR	81/46	1.80/1.05	0.75	0.58	2.0
640	3.7	HFIR	87/36	1.95/0.83	1.12	0.42	0.50
700	0.7	HFIR	102/72	2.27/1.64	0.63	0.72	1.1
750	0.6	JMTR	80/55	1.80/1.27	0.53	0.71	1.3
1030	0.7	HFIR	85/61	1.94/1.42	0.52	0.73	0.97
1080	4.2	HFIR	101/8	2.29/0.19	2.10	0.08	0.91
3C-SiC							
640	3.7	HFIR	87/30	1.94/0.68	1.26	0.35	0.59
700	0.7	HFIR	102/90	2.27/2.06	0.21	0.87	0.34
1030	0.7	HFIR	86/57	1.94/1.31	0.63	0.67	1.2
1080	4.2	HFIR	101/1	2.29/0.02	2.27	0.01	1.1

#### 4. Pyrolytic carbon/silicon carbide interface of TRISO-coating

##### 4.1. Background

Under neutron irradiation, anisotropic volume changes in the fuel kernel and/or the pyrolytic carbon often cause cracking within the inner PyC layer that can penetrate through the SiC layer or partial debonding at the inner PyC/SiC interface. If the layers do not completely debond at once or if only partial debonding occurs, severe stress concentration occurs at the tip of the crack opening between layers, resulting in a finite probability of failure of the SiC layer. In contrast, if the tensile radial stress that develops between the inner PyC and the SiC layers during irradiation exceeds the bonding strength, then the layers would debond relieving stresses. If complete debonding occurs, the stress between inner PyC and SiC is effectively zero, i.e., the SiC layer would no longer experience concentrated stresses associated with shrinkage cracks. This would decrease not only the probability that a shrinkage crack would lead to failure of the particle, but also the overall failure probability. In this case, the primary cause of stress in the SiC layer would be fission product gas buildup, limiting the failure to the more traditional pressure vessel failure mode. The complete debonding may increase the probability of the pressure vessel failure due to uniform pressurization, since the SiC stress due to pressure would increase with a debonded inner PyC layer. The primary failure mechanism therefore depends significantly on the magnitude of the bonding strength between layers.

Currently no data on the shear properties at the PyC/SiC interface of the TRISO-coating is available. However, PyC/SiC interfacial properties, both non-irradiated and neutron irradiated, using a simulated TRISO-coated tube material are presented (this work). As with the surrogate tubular specimens used for strength assessment, tubular samples were fabricated in a TRISO fuel fluidized bed for the purpose of PyC–SiC interfacial characterization as shown in Fig. 36. A micro-indentation push-out technique was developed to determine interfacial parameters: (1) an interfacial debond shear strength, which is required to initiate a crack at the interface, and (2) an interfacial friction stress at the debonded interface during fiber sliding (as defined in Fig. 37). As the PyC/SiC interfacial measurement is fundamentally important to the transfer of load to the

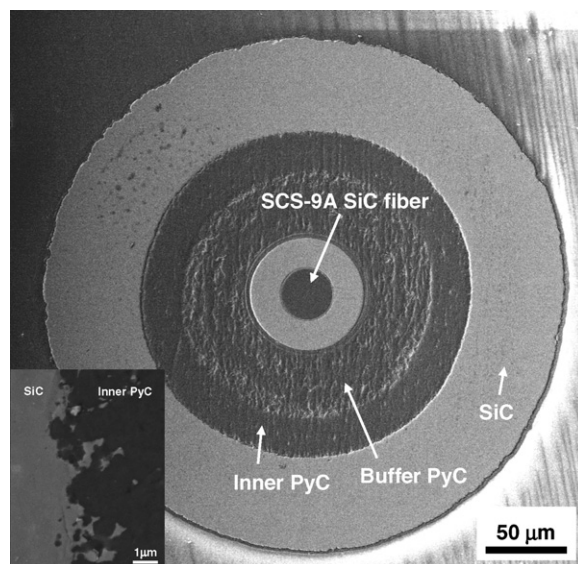


Fig. 36. Typical cross-section of a model TRISO-coated tube.

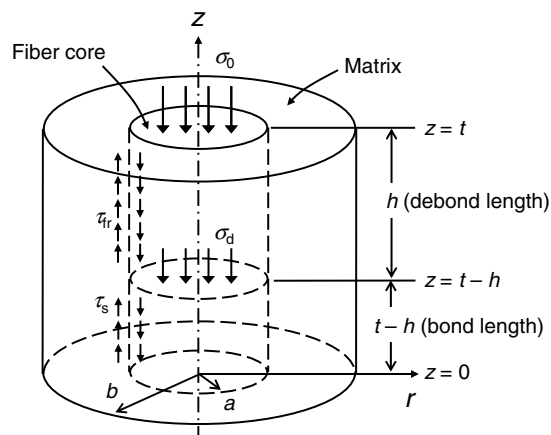


Fig. 37. A schematic illustration of cylindrical polar coordinates.

TRISO shell, and due to the fact that its definition is unique to this work, the balance of this section will present a relatively detailed explanation of the measurement and analysis of interfacial properties. Details of the testing technique development and the analytical model prediction approach for further understanding of the interfacial shear behavior of the TRISO-coating were discussed in Refs. [242,243].

##### 4.2. Interfacial debond shear strength

Fig. 38 shows a distribution of the debond initiation stress with respect to the TRISO surrogate

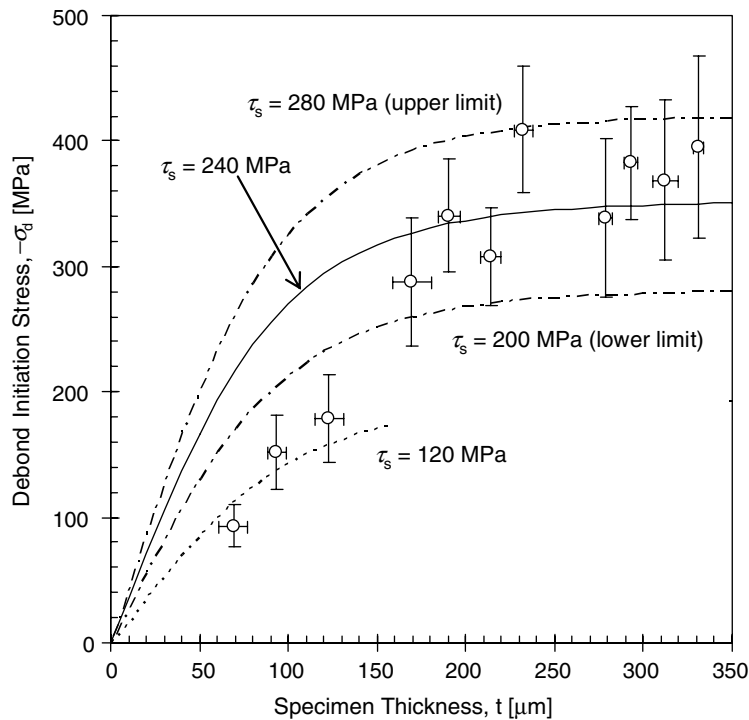


Fig. 38. Debond initiation stress vs. specimen thickness of model TRISO-coated tubes.

specimen thickness. The debond initiation stress monotonically increases with increasing specimen thickness and approaches a constant when  $t > 160 \mu\text{m}$ . By considering a relationship between debond initiation stress and interfacial shear strength (Eq. 20 in Ref. [243]), an interfacial debond shear strength of  $240 \pm 40 \text{ MPa}$  was obtained. Note that Table 10 lists material parameters used in analysis. As discussed previously [242], for thin specimens ( $<120 \mu\text{m}$ -thick), the interfacial debond shear strength becomes lower than the values expected.

This is believed to be due primarily to the effect of the stress relief from the open edges of the interface.

The interfacial debond shear strength at the inner PyC/SiC interface of the TRISO-coating is quite strong because the crack primarily propagates within the transient phase between inner PyC and SiC (Fig. 39). Such a high shear strength enables significant loads to be transferred at the inner PyC/SiC interface. The large scatter of the data is attributed to the probabilistic nature of debond initiation stress. According to the sensitivity analysis of the

Table 10  
Material parameters applied in analysis

	$d \text{ (g/cm}^3\text{)}$	$E_z \text{ (GPa)}$	$E_r \text{ (GPa)}$	$\nu_{r\theta}$	$\nu_{rz}$	$G_z \text{ (GPa)}^a$	$\alpha_z \text{ (10}^{-6}\text{/K)}^b$	$\alpha_r \text{ (10}^{-6}\text{/K)}^b$
SCS-9A SiC fiber <sup>c</sup>	2.8	307	200	0.2	0.3	128	4.3	4.3
Buffer isotropic PyC <sup>d</sup>	$\sim 1$	20	20	0.23	0.23	8	5.5	5.5
Inner isotropic PyC <sup>d</sup>	$\sim 2$	30	30	0.23	0.23	12	5.5	5.5
CVD-SiC <sup>e</sup>	3.21	460	460	0.21	0.21	190	4.4 <sup>f</sup>	4.4 <sup>f</sup>
Fiber core <sup>a</sup>	1.65	64	30	0.23	0.27	12	4.7	5.4

<sup>a</sup> Calculated by Hashin's theory [244].

<sup>b</sup> Average over the temperature range 298–1273 K.

<sup>c</sup> Product sheet from Specialty Materials, Inc. (Transverse properties are calculated by Hashin's theory [244].)

<sup>d</sup> Estimated from CEGA report [1].

<sup>e</sup> Product sheet from Rohm and Haas Co.

<sup>f</sup> Thermal expansion coefficient data from recent review in Fig. 8.

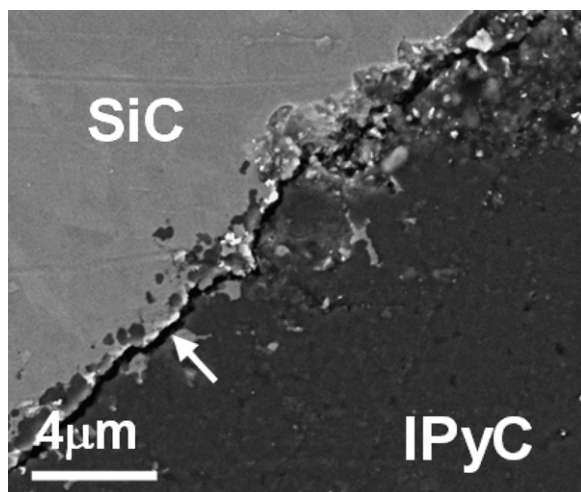


Fig. 39. A typical micrograph of crack propagation at the inner PyC/SiC interface.

parameters, the effects of measurement errors from the specimen size and the elastic constants are very small. For instance, 10% scatter of elastic modulus provides less than 5% scatter in the results. Similarly 10% scatter of thermal expansion coefficient gives at most 1% data scatter.

The effect of thermal expansion mismatch-induced residual stresses on interfacial debond shear

strength of TRISO-coated fuel particles is very minor, although may exist [243]. It can be inferred from this that the interfacial debond shear strength of the TRISO-coated fuel particles, estimated from the intrinsic value determined in Fig. 38 for the thick specimens, is  $\sim 240$  MPa. Of course, this value should be considered nominal as the interfacial properties will likely vary as the TRISO fabrication parameters are changed.

#### 4.3. Interfacial friction stress

Fig. 40 shows the frictional sliding stress as a function of TRISO surrogate specimen thickness. The fitted curves derived from modified Shetty's model (Eq. (28) in Ref. [243]) are also plotted in the figure. The modified Shetty's model for a transversely isotropic material gives the friction coefficient of 0.35 and the residual radial stress of  $-350$  MPa, yielding an intrinsic interfacial friction stress of 123 MPa. Similarly the upper and lower limits were obtained, giving data scatter of  $\sim 30$  MPa.

It is apparent that the thermal expansion mismatch between the fiber core and the SiC coating is not significant and, similar to the interfacial

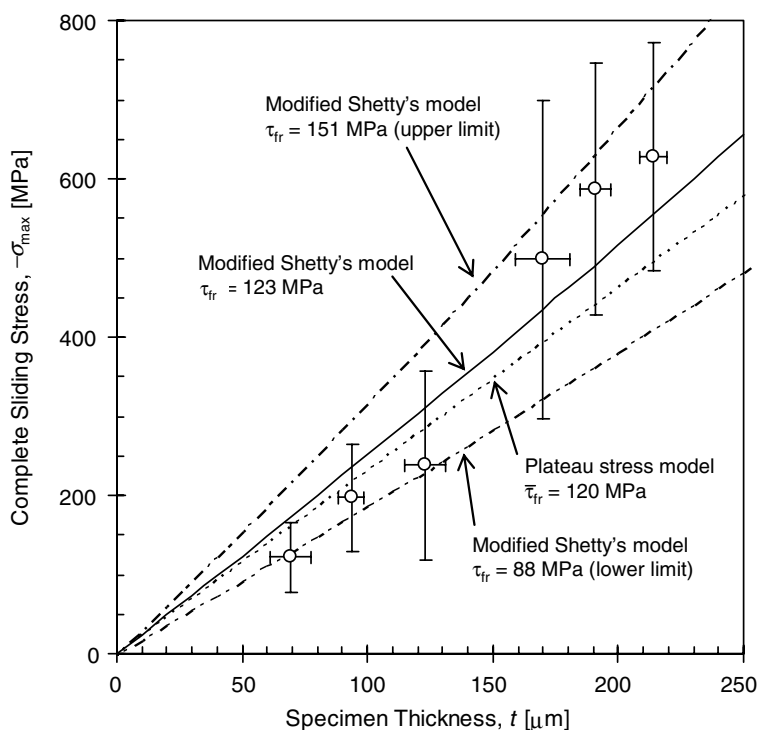


Fig. 40. Complete sliding stress vs. specimen thickness of model TRISO-coated tubes.

Table 11  
Summary of recommended properties of high purity CVD SiC

Properties	Non-irradiated	Irradiated
Density, $d$	$d$ (298 K) = $d_0 = 3.21$ g/cm <sup>3</sup>	$= d_0(1 + \Delta V/V_0)^{-1}$
Lattice parameter, $a$	Eq. (7) $a$ (298 K) = $a_0 = 0.43589$ nm	$= a_0(1 + \Delta V/3V_0)$
Swelling, $\zeta$ , $V/V_0$	–	Function of irradiation temperature and neutron fluence (Fig. 22)
Specific heat, $C_p$	Eq. (8) for $T < 200$ K Eq. (10) when $T > 200$ K (Fig. 4) $C_p$ (298 K) = 670 J/kg K	Assuming unchanged by irradiation (apparent $C_p$ may change when defect annealing is involved)
Thermal conductivity, $K$	Eq. (12) when $T > 298$ K (Fig. 5) $K$ (298 K) = $\sim < 350$ W/m K	$K = (1/K_0 + 1/K_{rd})^{-1}$ Function of irradiation temperature and neutron fluence (Figs. 25 and 26)
Coefficient of thermal expansion, $\alpha$	Eq. (16) when $T < 1273$ K (Fig. 6) $5.0 \times 10^{-6}$ /K when $T > 1273$ K $\alpha = 4.4 \times 10^{-6}$ /K (298–1273 K)	Assuming unchanged by irradiation (apparent $\alpha$ will be affected by irradiation when defect annealing is involved)
Young's modulus, $E$	Eq. (17) – Porosity dependence (Fig. 7) Eq. (18) – Temp. dependence (Fig. 8) $E$ (298 K) = $E_0 = 460$ GPa	$= E_0(1 - 6.974 \Delta V/V_0)$ when $T_{in} < 1273$ K (Fig. 29)
Poisson's ratio, $\nu$	Dependent on porosity & impurities Minor change at elevated temperatures $\nu$ (298 K) = 0.21	Not specified
Shear modulus, $G$	$= E/2(1 + \nu)$ $G$ (298 K) = 191 GPa	$= E/2(1 + \nu)$
Hardness, $H$	$H_V$ (298 K) = 22 GPa (4.9–19.6 N) Decrease with increasing porosity (Fig. 9) Decrease at elevated temperatures (Fig. 10)	Increase by irradiation Nearly independent of irradiation temperature and neutron dose (Fig. 30)
Fracture toughness, $K_{IC}$	$K_{IC}$ (298 K) = 3.2–3.5 MPa m <sup>1/2</sup> Dependent on grain size (Fig. 11) and temperature (Fig. 12)	Increase by irradiation (Fig. 31)
Characteristic strength, $\sigma_0$	Dependent on specimen size (surface area dominant) Increase at elevated temperatures (Fig. 13)	Increase by irradiation (Fig. 33)
Weibull modulus for fracture strength, $m$	4–11	Decrease or unchange (Fig. 35)
Thermal creep	Eq. (21) – Primary creep Eq. (22) – Steady-state creep (Fig. 14)	–
Irradiation creep	–	Eq. (25)

debond shear strength evaluation, the slight mismatch in the thermal expansivity therefore has a minor effect on the interfacial friction stress. In contrast, the significant residual radial stress at the interface is due primarily to the roughness at the cracked surface. Originally, the tortuous inner PyC/SiC interface formed by CVD does not allow crack propagation along the actual boundary between inner PyC and SiC, giving a very rough crack plane (Fig. 39). For a similar reason, the large

friction coefficient would be attributed to the rough surface at the interface.

#### 4.4. Effect of irradiation on interfacial strength

Unfortunately, no data exists for the effect of neutron irradiation on the interfacial debond shear or friction stress for TRISO particles or surrogates. However, based on interfacial property measurement carried out on non-irradiated and irradiated SiC fiber composites utilizing pyrolytic graphite interphase layers (which should undergo similar irradiation-induced changes to the TRISO inner PyC and outer PyC), a slight decrease in both debond shear and friction stress is expected [245,246]. It is the intent of the authors to carry out a direct measurement for irradiated TRISO fuels in the near future.

Table 12  
Summary of material properties of the PyC/SiC interface of TRISO-coating

Properties	Non-irradiated	Irradiated
Interfacial debond shear strength, $\tau_s$	$\sim 240$ MPa	Not specified
Interfacial friction stress, $\tau_{fr}$	$\sim 120$ MPa	Not specified



## 5. Conclusions

The purpose of this work was to provide a summary compilation of properties of non-irradiated and irradiated SiC for use in TRISO fuels modeling. Included in this summary was significant new work on the properties of strength of TRISO surrogate shells, materials irradiated under high-temperature neutron irradiation, and for the interfacial strength between the pyrolytic carbon layer and the SiC shell.

Tables 11 and 12 summarize material properties of SiC and PyC/SiC interface, respectively. It is noted that much of this data is still inadequate for the entire irradiation performance range expected for TRISO fuels in application, though provides a substantial improvement over the previously assumed CEGA data-set. Moreover, this handbook will be continuously updated as data comes available. The intent of the authors is to continue to update this data-base as TRISO-relevant data becomes available (including potential alternative materials such as ZrC) and to make such a handbook openly available.

## References

- [1] CEGA Report, CEGA-002820, Rev 1, NP-MHTGR Material Models of Pyrocarbon and Pyrolytic Silicon Carbide, July 1993.
- [2] H.O. Pierson, Handbook of Refractory Carbides and Nitrides, Noyes Publications, New Jersey, 1996.
- [3] NIST WebSCD Database, <<http://www.ceramics.nist.gov/srd/scd/scdquery.htm>>.
- [4] R.J. Price, Nucl. Technol. 35 (1977) 320.
- [5] E.G. Acheson, Chem. News 68 (1893) 179.
- [6] J.S. Goela, L.E. Burns, R.L. Taylor, Appl. Phys. Lett. 64 (1994) 131.
- [7] S.J. Xu, J.G. Zhou, B. Yang, B.Z. Zhang, J. Nucl. Mater. 224 (1995) 12.
- [8] S. Yajima, J. Hayashi, M. Omori, K. Okamura, Nature 261 (1976) 683.
- [9] T. Ishikawa, Y. Kohtoku, K. Kumagawa, T. Yamamura, T. Nagasawa, Nature 391 (1998) 773.
- [10] S. Prochazka, R.M. Scanlan, J. Am. Ceram. Soc. 58 (1975) 72.
- [11] T.D. Gulden, J. Am. Ceram. Soc. 51 (1968) 424.
- [12] R.L. Beatty, Report ORNL-TM-1649, 1967.
- [13] R.W. Olesinski, G.J. Abbaschian, Bull. Alloy Phase Diagrams 5 (1984) 486.
- [14] S.C. Singhal, Ceram. Int. 2 (1976) 123.
- [15] J. Drowart, G. De Maria, M.G. Inghram, J. Chem. Phys. 29 (1958) 1015.
- [16] N.W. Jepps, T.F. Page, J. Cryst. Growth Charact. 7 (1983) 259.
- [17] P. Pirouz, J.W. Yang, Ultramicroscopy 51 (1993) 189.
- [18] P.T.B. Shaffer, Acta Cryst. B 25 (1968) 477.
- [19] G.R. Fisher, P. Barnes, Philos. Mag. B 61 (1990) 217.
- [20] M. Iwami, Nucl. Instrum. and Meth. A 466 (2001) 406.
- [21] W.F. Knippenberg, Philips Res. Rept. 18 (1963) 161.
- [22] W. Weltner Jr., J. Chem. Phys. 51 (1969) 2469.
- [23] L.B. Griffiths, J. Phys. Chem. Solids 27 (1966) 257.
- [24] P. Krishna, R.C. Marshall, C.E. Ryan, J. Cryst. Growth 8 (1971) 129.
- [25] JCPDS 29-1126 ~ 29, 39-1196, 22-1319.
- [26] Z. Li, R.C. Bradt, J. Appl. Phys. 60 (1986) 612.
- [27] Z. Li, R.C. Bradt, J. Am. Ceram. Soc. 69 (1986) 863.
- [28] Z. Li, R.C. Bradt, J. Mater. Sci. 21 (1986) 4366.
- [29] R.G. Munro, J. Phys. Chem. Ref. Data 26 (1997) 1195.
- [30] P.T.B. Shaffer, Engineered Materials Handbook, vol. 4, Ceramics and Glasses, Materials Information Society, 1991, p. 804.
- [31] D.-M. Liu, B.-W. Lin, Ceram. Int. 22 (1996) 407.
- [32] Product sheet from Rohm and Haas Co., <<http://www.cvdmaterials.com/sicprop2.htm>>.
- [33] M.A. Pickering, R.L. Taylor, J.T. Keeley, G.A. Graves, Nucl. Instrum. and Meth. A 291 (1990) 95.
- [34] A.K. Collins, M.A. Pickering, R.L. Taylor, J. Appl. Phys. 68 (1990) 6510.
- [35] K.K. Kelley, J. Am. Ceram. Soc. 63 (1941) 1137.
- [36] B.E. Walker Jr., C.T. Ewing, R.R. Miller, J. Chem. Eng. Data 7 (1962) 595.
- [37] L.S. Sigl, J. Eur. Ceram. Soc. 23 (2003) 1115.
- [38] Engineering Property Data on Selected Ceramics, vol. 2, Ceramics Information Center, Battelle Columbus Laboratories. Report MCIC-HB-07, 1979.
- [39] M.E. Schlesinger, in: S.J. Schneider Jr. (Ed.), Engineered Materials Handbook, Ceramics and Glasses, vol. 4, ASM International, Metals Park, Ohio, 1991, p. 883.
- [40] L.V. Gurvich, I.V. Veyts, Thermodynamic Properties of Individual Substances, Hemisphere Publishing Corporation, New York, 1972.
- [41] A. Zywiets, K. Karch, F. Bechstedt, Phys. Rev. B 54 (1996) 1791.
- [42] A. Wolfenden, J. Mater. Sci. 32 (1997) 2275.
- [43] G.A. Slack, J. Appl. Phys. 35 (1964) 3460.
- [44] D. Singh, Y.P. Varshni, Phys. Rev. B 24 (1981) 4340.
- [45] D. Singh, Y.P. Varshni, Acta Cryst. A 38 (1982) 854.
- [46] R.E. Taylor, H. Groot, J. Ferrier, Thermophysical Properties of CVD SiC, TRPL 1336, Thermophysical Properties Research Laboratory Report, School of Mechanical Engineering, Purdue University, 1993.
- [47] D.J. Senior, G.E. Youngblood, C.E. Moore, D.J. Trimble, G.A. Newsome, J.J. Woods, Fus. Technol. 30 (1996) 943.
- [48] J.E. Graebner, H. Altmann, N.M. Balzaretti, R. Campbell, H.-B. Chae, A. Degiovanni, R. Enck, A. Feldman, D. Fournier, J. Fricke, J.S. Goela, K.J. Gray, Y.Q. Gu, I. Hatta, T.M. Hartnett, R.E. Imhof, R. Kato, P. Koidl, P.K. Kuo, T.-K. Lee, D. Maillet, B. Remy, J.P. Roger, D.-J. Seong, R.P. Tye, H. Verhoeven, E. Worner, J.E. Yehoda, R. Zachai, B. Zhang, Diam. Relat. Mater. 7 (1998) 1589.
- [49] M. Rohde, J. Nucl. Mater. 182 (1991) 87.
- [50] R.J. Price, J. Nucl. Mater. 46 (1972) 268.
- [51] R.J. Price, J. Am. Ceram. Soc. Bull. 48 (1969) 859.
- [52] J. Li, L. Porter, S. Yip, J. Nucl. Mater. 255 (1998) 139.
- [53] G.A. Slack, J. Phys. Chem. Solids 34 (1973) 321.



- [54] C.H. McMurtry, W.D.G. Boecker, S.G. Seshadri, J.S. Zanghi, J.E. Garnier, *J. Am. Ceram. Soc. Bull.* 66 (1987) 325.
- [55] T. Maruyama, M. Harayama, *J. Nucl. Mater.* 329–333 (2004) 1022.
- [56] C.W. Forrest, P. Kennedy, J.V. Shennan, in: P. Popper (Ed.), *Special Ceramics*, vol. 5, Brit. Ceram. Res. Assn., London, p. 99.
- [57] T. Darroudi, *Projects Within the Center for Advanced Materials*, 1989, p. 63.
- [58] E.H. Kraft, G.I. Dooher, *Conference on Mechanical Behavior of Materials*, 1976, p. 1.
- [59] K. Becher, *Z. Physik* 40 (1926) 37.
- [60] T.A. Taylor, R.M. Jones, in: J.R. O'Connor, J. Smiltens (Eds.), *Silicon Carbide, a High-Temperature Semiconductor*, Pergamon, Oxford, 1960, p. 147.
- [61] D. Clark, D. Knight, Royal Aircraft Establishment, Technical Report RAE-TR-65049, 1965.
- [62] H. Suzuki, T. Iseki, M. Ito, *J. Nucl. Mater.* 48 (1973) 247.
- [63] P. Popper, I. Mohyuddin, in: P. Popper (Ed.), *Special Ceramics 1964*, Academic Press, London, 1965, p. 45.
- [64] E.L. Kern, D.W. Hamill, H.W. Deem, H.D. Sheets, *Mater. Res. Bull.* 4 (1969) S25.
- [65] A.F. Pojur, B. Yates, B.T. Kelly, *J. Phys. D* 5 (1972) 1321.
- [66] T.R. Watkins, D.J. Green, *J. Am. Ceram. Soc.* 76 (1993) 3066.
- [67] M. Bonnke, E. Fitzer, *Ber. Deut. Keram. Ges.* 43 (1966) 180.
- [68] G.L. Harris, *Properties of Silicon Carbide*, EMIS Datareviews Series No. 13, INSPEC, London, 1995.
- [69] M.-J. Pan, P.A. Hoffman, D.J. Green, J.R. Hellmann, *J. Am. Ceram. Soc.* 80 (1997) 692.
- [70] D.J. Green, J.R. Hellmann, M.F. Modest, *Projects Within the Center for Advanced Materials*, 1990, p. 71.
- [71] D.E. McCullum, N.L. Hecht, L. Chuck, S.M. Goodrich, *Ceram. Eng. Sci. Proc.* 12 (1991) 1886.
- [72] G.A. Graves, N.L. Hecht, UDR-TR-94-136, 1995, 1.
- [73] J.B. Wachtman Jr., D.G. Lam Jr., *J. Am. Ceram. Soc.* 42 (1959) 254.
- [74] W.S. Coblenz, *J. Am. Ceram. Soc.* 58 (1975) 530.
- [75] C. Tracy, M. Slavin, D. Viechnicki, *Adv. Ceram.* 22 (1988) 295.
- [76] M.J. Slavin, G.D. Quinn, *Int. J. High Technol.* 2 (1986) 47.
- [77] C.A. Tracy, G.D. Quinn, *Ceram. Eng. Sci. Proc.* 15 (1994) 837.
- [78] N.L. Hecht, D.E. McCullum, G.A. Graves, *Ceramic Materials and Components for Engines* (1988) 806.
- [79] R. Ruh, A. Zagvil, J. Barlowe, *Am. Ceram. Soc. Bull.* 64 (1985) 1368.
- [80] Y. Zhou, K. Hirao, M. Toriyama, Y. Yamauchi, S. Kanzaki, *J. Am. Ceram. Soc.* 84 (2001) 1642.
- [81] N.G. Einspruch, L.T. Claiborne, *J. Acoust. Soc. Am.* 35 (1963) 925.
- [82] B.L.P. Keyes, ORNL/M-2775, 1992, p. 1.
- [83] S.G. Seshadri, K.-Y. Chia, *J. Am. Ceram. Soc.* 70 (1987) C242.
- [84] N.L. Hecht, S.M. Goodrich, L. Chuck, D.E. McCullum, V.J. Tennery, *Am. Ceram. Soc. Bull.* 71 (1992) 653.
- [85] B.V. Cockeram, *J. Am. Ceram. Soc.* 85 (2002) 603.
- [86] T.D. Gulden, *J. Am. Ceram. Soc.* 52 (1969) 585.
- [87] J. Kubler, *Mechanische Charakterisierung von Hochleistungskeramik Festigkeitsunte* (1992) 1.
- [88] B.O. Yavuz, R.E. Tressler, *Ceram. Int.* 18 (1992) 19.
- [89] J.M. Grow, R.A. Levy, *J. Mater. Res.* 9 (1994) 2072.
- [90] M.C. Osborne, J.C. Hay, L.L. Snead, D. Steiner, *J. Am. Ceram. Soc.* 82 (1999) 2490.
- [91] S. Nogami, A. Hasegawa, L.L. Snead, *J. Nucl. Mater.* 307–311 (2002) 1163.
- [92] K.H. Park, S. Kondo, Y. Katoh, A. Kohyama, *Fus. Sci. Technol.* 44 (2003) 455.
- [93] Y. Katoh, L.L. Snead, *J. ASTM Int.* 2 (2005) 12377.
- [94] Yu.V. Milman, S.I. Chugunova, I.V. Goncharova, T. Chudoba, W. Lojkowski, W. Gooch, *Int. J. Refract. Met. Hard Mater.* 17 (1999) 361.
- [95] K. Bongartz, E. Gyarmati, H. Schuster, K. Tauber, *J. Nucl. Mater.* 62 (1976) 123.
- [96] K. Minato, K. Fukuda, K. Ikawa, *J. Nucl. Sci. Technol.* 19 (1982) 69.
- [97] K. Bongartz, E. Gyarmati, H. Nickel, H. Schuster, W. Winter, *J. Nucl. Mater.* 45 (1972/73) 261.
- [98] T.D. Gulden, H. Nickel, *Nucl. Technol.* 35 (1977) 206.
- [99] O.L. Anderson, *Phys. Rev.* 144 (1966) 553.
- [100] K.B. Tolpygo, *Sov. Phys. Solid State* 2 (1961) 2367.
- [101] K. Kamitani, M. Grimsditch, J.C. Nipko, C.-K. Loong, *J. Appl. Phys.* 82 (1997) 3152.
- [102] V.M. Lyubimskii, *Sov. Phys. Solid State* 18 (1976) 1814.
- [103] G. Arlt, G.R. Schodder, *J. Acoust. Soc. Am.* 37 (1965) 384.
- [104] Z. Li, R.C. Bradt, *Int. J. High Technol. Ceram.* 4 (1988) 1.
- [105] R.J. Gettings, G.D. Quinn, *Ceram. Eng. Sci. Proc.* 16 (1995) 539.
- [106] A.G. Evans, E.A. Charles, *J. Am. Ceram. Soc.* 59 (1976) 371.
- [107] J. Denape, J. Lamon, *J. Mater. Sci.* 25 (1990) 3592.
- [108] J.R. Hellmann, P. Strzepa, *Projects Within the Center for Advanced Materials*, 1987, p. 51.
- [109] H. Kodama, T. Miyoshi, *J. Am. Ceram. Soc.* 73 (1990) 3081.
- [110] H. Wang, R.N. Singh, J.S. Goela, *J. Am. Ceram. Soc.* 78 (1995) 2437.
- [111] J.B. Quinn, G.D. Quinn, *J. Mater. Sci.* 32 (1997) 4331.
- [112] N.L. Hecht, G.A. Graves, D.E. McCullum, A.P. Berens, S. Goodrich, J.D. Wolf, J.R. Hoenigman, P. Yaney, D. Grant, S. Hilton, ORNL/Sub/84-00221/2, 1990, p. 1.
- [113] D. Chakraborty, A.K. Mukhopadhyay, J. Mukerji, *Revue Internationale des Hautes Temperatures et des Refractaires* 22 (1985) 105.
- [114] S. Fujita, K. Maeda, S. Hyodo, *J. Mater. Sci. Lett.* 5 (1986) 450.
- [115] K. Niihara, *J. Less Common Met.* 65 (1979) 155.
- [116] E. Ryshkewitch, *J. Am. Ceram. Soc.* 36 (1953) 65.
- [117] K. Niihara, *J. Am. Ceram. Soc. Bull.* 63 (1984) 1160.
- [118] W.A. Zdaniewski, H.P. Kirchner, *J. Am. Ceram. Soc.* 70 (1987) 548.
- [119] G.H. Campbell, B.J. Dalgleish, A.G. Evans, *J. Am. Ceram. Soc.* 72 (1989) 1402.
- [120] E.H. Kraft, R.H. Smoak, Report – Fall Meeting, American Ceramic Society, 1977, p. 3.
- [121] A. Ghosh, M.G. Jenkins, K.W. White, A.S. Kobayashi, R.C. Bradt, *J. Am. Ceram. Soc.* 72 (1989) 242.
- [122] G.D. Quinn, J.J. Swab, M.D. Hill, *Ceram. Eng. Sci. Proc.* 18 (1997) 163.
- [123] G.D. Quinn, J.A. Salem, *J. Am. Ceram. Soc.* 85 (2002) 873.
- [124] A.G. Evans, F.F. Lange, *J. Mater. Sci.* 10 (1975) 1659.

- [125] T. Ohji, Y. Yamauchi, W. Kanematsu, S. Ito, J. Am. Ceram. Soc. 72 (1989) 688.
- [126] B.O. Yavuz, R.E. Tressler, J. Am. Ceram. Soc. 76 (1993) 1017.
- [127] M.A. Mulla, V.D. Krstic, Acta Metall. Mater. 42 (1994) 303.
- [128] R.E. Tressler, Projects Within the Center for Advanced Materials, 1987, p. 124.
- [129] S.A. Mariano, D. Friel, I. Bar-On, Ceram. Eng. Sci. Proc. 14 (1993) 1077.
- [130] D.C. Larsen, J.W. Adams, AFWAL Contract Report TR-83-4141, 1984.
- [131] J. Kubler, Ceram. Eng. Sci. Proc. 18 (1997) 155.
- [132] R.N. Katz, S. Grendahl, K. Cho, I. Bar-On, W. Rafaniello, Ceram. Eng. Sci. Proc. 15 (1994) 877.
- [133] L.A. Simpson, Fracture Mechanics of Ceramics Vol. 2, Plenum, New York, 1974.
- [134] J.A. Coppola, R.C. Bradt, J. Am. Ceram. Soc. 55 (1972) 455.
- [135] J.R. Rice, S.W. Freiman, P.F. Becher, J. Am. Ceram. Soc. 64 (1981) 345.
- [136] R.B. Matthews, W.G. Hutchings, F. Havelock, J. Can. Ceram. Soc. 42 (1973) 1.
- [137] R.W. Rice, S.W. Freiman, J. Am. Ceram. Soc. 64 (1981) 350.
- [138] J. Schlichting, Powd. Metall. Int. 12 (1980) 141.
- [139] R. Stevens, J. Mater. Sci. 6 (1971) 324.
- [140] J.L. Henshall, D.J. Rowcliffe, J.W. Deington, J. Am. Ceram. Soc. 60 (1977) 373.
- [141] T.S. Byun, S.G. Hong, L.L. Snead, Y. Katoh, in: 30th Annual International Conference on Advanced Ceramics and Composites, Cocoa Beach, FL, USA, 2005.
- [142] A.G. Evans, C. Padgett, R.W. Davidge, J. Am. Ceram. Soc. 56 (1973) 36.
- [143] A. Briggs, R.W. Davidge, C. Padgett, S. Quickenden, J. Nucl. Mater. 61 (1976) 233.
- [144] J.W. Ketterer, General Atomics Document 910105 N/C, 1990.
- [145] N.N. Nemeth, J.M. Manderscheid, J.P. Gyekenyesi, Ceram. Bull. 68 (1989) 2064.
- [146] T.S. Byun, E. Lara-Curzio, L.L. Snead, Y. Katoh, J. Nucl. Mater., doi:10.1016/j.jnucmat.2007.03.014.
- [147] M.L. Torti, M.L. Paille, J.J. Litwinowich, Adv. Ceram. 14 (1985) 291.
- [148] S.-G. Hong, T.-S. Byun, R.A. Lowden, L.L. Snead, Y. Katoh, J. Am. Ceram. Soc. 90 (2007) 184.
- [149] T.D. Gulden, C.F. Driscoll, Report GA-10366, 1971.
- [150] C.H. Carter Jr., R.F. Davis, J. Bentley, J. Am. Ceram. Soc. 67 (1984) 732.
- [151] J.A. DiCarlo, J. Mater. Sci. 21 (1986) 217.
- [152] G.N. Morscher, C.A. Lewinsohn, C.E. Bakis, R.E. Tressler, T. Wagner, J. Am. Ceram. Soc. 78 (1995) 3244.
- [153] G.N. Morscher, J.A. DiCarlo, J. Am. Ceram. Soc. 75 (1992) 136.
- [154] R.F. Davis, C.H. Carter Jr., A Review of Creep in Silicon Carbide and Silicon Nitride, Oxford University Press and Ohmsha, Ltd., 1988.
- [155] J.N. Wang, J. Mater. Sci. 29 (1994) 6139.
- [156] M.H. Hon, R.F. Davis, J. Mater. Sci. 14 (1979) 2411.
- [157] T. Ohji, Y. Yamauchi, J. Am. Ceram. Soc. 75 (1992) 2304.
- [158] G.S. Corwan, J. Am. Ceram. Soc. 75 (1992) 3421.
- [159] T. Narushima, T. Goto, T. Hirai, J. Am. Ceram. Soc. 72 (1989) 1386.
- [160] M.J.H. Balat, J. Eur. Ceram. Soc. 16 (1996) 55.
- [161] B. Schneider, A. Guette, R. Naslain, M. Cataldi, A. Costecalde, J. Mater. Sci. 33 (1998) 535.
- [162] E.J. Opila, J. Am. Ceram. Soc. 82 (1999) 625.
- [163] C. Eric Ramberg, W.L. Worrell, J. Am. Ceram. Soc. 84 (2001) 2607.
- [164] T. Goto, H. Homma, J. Eur. Ceram. Soc. 22 (2002) 2749.
- [165] Y. Song, F.W. Smith, J. Am. Ceram. Soc. 88 (2005) 1864.
- [166] J.A. Costello, R.E. Tressler, J. Am. Ceram. Soc. 69 (1986) 674.
- [167] K.L. Luthra, J. Am. Ceram. Soc. 74 (1991) 1095.
- [168] T. Narushima, T. Goto, Y. Iguchi, T. Hirai, J. Am. Ceram. Soc. 74 (1991) 2583.
- [169] C. Eric Ramberg, G. Cruciani, K.E. Spear, R.E. Tressler, C.F. Ramberg Jr., J. Am. Ceram. Soc. 79 (1996) 2897.
- [170] J.D. Kalen, R.S. Boyce, J.D. Cawley, J. Am. Ceram. Soc. 74 (1991) 203.
- [171] M.A. Lamkin, F.L. Riley, R.J. Fordham, J. Eur. Ceram. Soc. 10 (1992) 347.
- [172] T. Narushima, T. Goto, Y. Yokoyama, M. Takeuchi, Y. Iguchi, T. Hirai, J. Am. Ceram. Soc. 77 (1994) 1079.
- [173] T. Narushima, T. Goto, Y. Iguchi, T. Hirai, J. Am. Ceram. Soc. 73 (1990) 3580.
- [174] T. Iseki, in: JSPS (Ed.), Advanced Silicon Carbide Ceramics, Uchida Rokakuho Publishing Co., Ltd., Tokyo, 2001 (in Japanese).
- [175] N.S. Jacobson, J. Am. Ceram. Soc. 76 (1993) 3.
- [176] T. Narushima, T. Goto, T. Hirai, Y. Iguchi, Mater. Trans. 38 (1997) 821.
- [177] S.C. Singhal, F.F. Lange, J. Am. Ceram. Soc. 58 (1975) 433.
- [178] G. Ervin Jr., J. Am. Ceram. Soc. 41 (1958) 347.
- [179] R.E. Tressler, M.D. Meiser, T. Yonushonis, J. Am. Ceram. Soc. 59 (1976) 278.
- [180] D.W. McKee, D. Chatterji, J. Am. Ceram. Soc. 59 (1976) 441.
- [181] K. Yamada, M. Mori, in: S. Somiya, Y. Inomata (Eds.), SiC Ceramics, Uchida Rokakuho Publishing Co., Ltd., Tokyo, 1988 (in Japanese).
- [182] R. Blackstone, E.H. Voice, J. Nucl. Mater. 39 (1971) 319.
- [183] R.J. Price, J. Nucl. Mater. 33 (1969) 17.
- [184] R.J. Price, J. Nucl. Mater. 48 (1973) 47.
- [185] W. Primak, L.H. Fuchs, P.P. Day, Phys. Rev. 103 (1956) 1184.
- [186] M. Balarin, Phys. Stat. Sol. 11 (1965) K67.
- [187] N.F. Pravdyuk, et al., Properties of Reactor Materials and the Effects of Radiation Damage Proceedings, 1962.
- [188] R.P. Thorne, V.C. Howard, B. Hope, Proc. Brit. Ceramic Soc. 7 (1967).
- [189] R. Stevens, Philos. Mag. 25 (1972) 523.
- [190] J.C. Corelli, J. Hoole, J. Lazzaro, C.W. Lee, J. Am. Ceram. Soc. 66 (1983) 529.
- [191] H. Miyazaki et al., J. Nucl. Sci. Technol. 29 (1992) 656.
- [192] R.B. Matthews, J. Nucl. Mater. 51 (1974) 203.
- [193] L.L. Snead, J. Nucl. Mater. 329–333 (2004) 524.
- [194] L.L. Snead, J. Nucl. Mater. 326 (2004) 114.
- [195] G.W. Hollenberg, C.H. Henager Jr., G.E. Youngblood, D.J. Trimble, S.A. Simonson, G.A. Newsome, E. Lewis, J. Nucl. Mater. 219 (1995) 70.
- [196] G.E. Youngblood, D.J. Senor, R.H. Jones, Fus. Mater. DOE/ER-0313/33, 2002, p. 27.

- [197] D.J. Senor, G.E. Youngblood, L.R. Greenwood, D.V. Archer, D.L. Alexander, M.C. Chen, G.A. Newsome, *J. Nucl. Mater.* 317 (2003) 145.
- [198] W. Dienst, T. Fett, R. Heidinger, H.D. Rohrig, B. Schulz, *J. Nucl. Mater.* 174 (1990) 102.
- [199] T. Iseki, T. Maruyama, T. Yano, T. Suzuki, T. Mori, *J. Nucl. Mater.* 170 (1990) 95.
- [200] C.W. Lee, F.J. Pineau, J.C. Corelli, *J. Nucl. Mater.* 108&109 (1982) 678.
- [201] G.E. Youngblood, D.J. Senor, R.H. Jones, *J. Nucl. Mater.* 329–333 (2004) 507.
- [202] L.L. Snead, T. Hinoki, Y. Katoh, *Fus. Mater. DOE/ER-0313/33*, 2003, p. 49.
- [203] G. Newsome, L.L. Snead, T. Hinoki, Y. Katoh, D. Peters, *J. Nucl. Mater.*, in press.
- [204] Y. Katoh, N. Hashimoto, S. Kondo, L.L. Snead, A. Kohyama, *J. Nucl. Mater.* 351 (2006) 228.
- [205] L.L. Snead, S.J. Zinkle, in: I.M. Robertson, G.S. Was, L.W. Hobbs, T.D. de la Rubia (Eds.), *Microstructure Evolution during Irradiation*, vol. 439, Materials Research Society, Pittsburgh, 1997, p. 595.
- [206] Y. Katoh, H. Kishimoto, A. Kohyama, *J. Nucl. Mater.* 307–311 (2002) 1221.
- [207] L.L. Snead, S.J. Zinkle, J.C. Hay, M.C. Osborne, *Nucl. Instrum. and Meth. B* 141 (1998) 123.
- [208] L.L. Snead, S.J. Zinkle, *Nucl. Instrum. and Meth. B* 191 (2002) 497.
- [209] S.I. Golubov, *Phys. Met. Metall.* 60 (1985) 7.
- [210] Y. Katoh, S.I. Golubov, L.L. Snead, *Ceram. Eng. Sci. Proc.*, accepted for publication.
- [211] T. Yano, H. Miyazaki, M. Akiyoshi, T. Iseki, *J. Nucl. Mater.* 253 (1998) 78.
- [212] S. Kondo, K.H. Park, Y. Katoh, A. Kohyama, *Fus. Sci. Technol.* 44 (2003) 181.
- [213] Y. Katoh, L.L. Snead, C.H. Henager, Jr., A. Hasegawa, A. Kohyama, B. Riccardi, H. Hegeman, in: 12th International Conference on Fusion Reactor Materials, 2005, Santa Barbara, CA, USA, *J. Nucl. Mater.*, in press.
- [214] S. Kondo, A. Kohyama, T. Hinoki, in: 12th International Conference on Fusion Reactor Materials, 2005, Santa Barbara, CA, USA, *J. Nucl. Mater.*, in press.
- [215] R.J. Price, *J. Nucl. Mater.* 46 (1973) 268.
- [216] H. Itoh, N. Hayakawa, I. Nashiyama, E. Sakuma, *J. Appl. Phys.* 66 (1989) 4529.
- [217] A. Kawasuso, H. Itoh, N. Morishita, M. Yoshikawa, T. Ohshima, I. Nashiyama, S. Okada, H. Okumura, S. Yoshida, *Appl. Phys. A* 67 (1998) 209.
- [218] S. Kondo, Y. Katoh, L.L. Snead, in: 2007 Annual TMS Meeting, 2007, Orlando, FL, USA.
- [219] L.L. Snead, Y. Katoh, S. Kondo, in: 12th International Conference on Fusion Reactor Materials, 2005, Santa Barbara, CA, USA, *J. Nucl. Mater.*, in press.
- [220] L.L. Snead, R. Scholz, A. Hasegawa, A. Frias Rebelo, *J. Nucl. Mater.* 307–311 (2002) 1141.
- [221] H.C. Huang, N.M. Goniem, J.K. Wong, M.I. Baskes, *Modelling Simul. Mater. Sci. Eng.* 3 (1995) 615.
- [222] M. Bockstedte, A. Mattausch, O. Pankratov, *Phys. Rev. B* 68 (2003) 205201.
- [223] C.H. Lam et al., *Mat. Res. Soc. Symp. Proc.* 792 (2004) R3.19.1.
- [224] L.A. de S. Balona, J.H.N. Lousber, *J. Phys. C* 3 (1970) 2344.
- [225] L.L. Snead, S.J. Zinkle, S.J. White, *J. Nucl. Mater.* 340 (2005) 187.
- [226] R.P. Thorne, V.C. Howard, B. Hope, *Proc. Brit. Ceramic Soc.* 7 (1967) 449.
- [227] R.J. Price, *Nucl. Technol.* 16 (1972) 536.
- [228] L.L. Snead, A. Marie Williams, A.L. Qualls, *ASTM STP* 1447 (2003) 623.
- [229] J. Tersoff, *Phys. Rev. B* 39 (1989) 5566.
- [230] S.D. Harrison, J.C. Corelli, *J. Nucl. Mater.* 122&123 (1984) 833.
- [231] W. Dienst, *Fus. Eng. Des.* 16 (1990) 311.
- [232] R.J. Price, G.R. Hopkins, *J. Nucl. Mater.* 108&109 (1982) 732.
- [233] R.A. Matheny, J.C. Corelli, *J. Nucl. Mater.* 83 (1979) 313.
- [234] B.E. Sheldon, UKAEA Report AERE-R8025, 1975.
- [235] R. Scholz, *J. Nucl. Mater.* 254 (1998) 74.
- [236] R. Scholz, *J. Nucl. Mater.* 258–263 (1998) 1533.
- [237] R. Scholz, R. Mueller, D. Lesueur, *J. Nucl. Mater.* 307–311 (2002) 1183.
- [238] R. Scholz, G.E. Youngblood, *J. Nucl. Mater.* 283–287 (2000) 372.
- [239] Y. Katoh, L.L. Snead, T. Hinoki, S. Kondo, A. Kohyama, *J. Nucl. Mater.*, in press.
- [240] K. Ehrlich, *J. Nucl. Mater.* 100 (1981) 149.
- [241] J.R. Matthews, M.W. Finnis, *J. Nucl. Mater.* 159 (1988) 257.
- [242] T. Nozawa, L.L. Snead, Y. Katoh, J.H. Miller, E. Lara-Curzio, *J. Nucl. Mater.* 350 (2006) 182.
- [243] T. Nozawa, L.L. Snead, Y. Katoh, J.H. Miller, *J. Nucl. Mater.*, in press.
- [244] Z. Hashin, *J. Appl. Mech.* 46 (1979) 543.
- [245] T. Nozawa, Y. Katoh, L.L. Snead, in: 12th International Conference on Fusion Reactor Materials, 2005, Santa Barbara, CA, USA, *J. Nucl. Mater.*, in press.
- [246] T. Nozawa, Y. Katoh, L.L. Snead, in: 7th IEA International Workshop on SiC/SiC for Fusion and 1st International Workshop on C and SiC Composites for Advanced Fission, Petten, The Netherlands, 2006.